Estimation of Geoacoustic parameters of the Ocean Bottom by Inversion of Reflection Loss data

by

David Edward Hannay
B Sc , University of Victoria, 1988

A thesis submitted in Partial Fulfillment of the
Requirements for the Degree of

MASTER OF SCIENCE

in the Department of Physics and Astronomy

We accept this thesis as conforming to the required standard

[redacted]

Dr N R Chapman, Supervisor (Defence Research Establishment Pacific)

[redacted]

Dr H Dosso, Co-Supervisor (Dept of Physics and Astronomy)

[redacted]

Dr G Spence, Outside Member (School of Earth and Ocean Sciences)

[redacted]

Dr K Rohr, External Examiner
(Pacific Geoscience Centre, Geological Survey of Canada)

Supervisor Dr N R Chapman

Abstract

An inversion method has been developed for estimating the geoacoustic parameters of the ocean bottom at thin sediment sites, such as those in the Abyssal Hills region of the North Pacific The ocean bottom is modeled by two elastic layers representing pelagic sediment overlying basalt The method fits bottom reflection loss versus grazing angle, calculated for many possible bottom models, to measured data Simulated annealing optimization is used to perform an efficient search to find the model which produces the best match between the calculated losses and the data Parameter values associated with this optimum model are taken as the geoacoustic parameter estimates at the experiment site This method was tested with simulated data to demonstrate its effectiveness for estimating several elastic parameters The method was found to provide reliable estimates for basalt p and s wave speeds, and the sediment s wave speed The inversion method was applied to data obtained along a track in the North Pacific, over which the basalt age increased from ~42 m y to ~63 m y The estimates indicated trends of increasing basalt wave speed with age, from 2 6 km/s to 3 2 km/s for p waves, and from 1 0 km/s to 1 5 km/s for s waves

Examiners

[redacted]

Dr N R Chapman, Supervisor (Defence Research Establishment Pacific)

[redacted]

Dr H Dosso Co-Supervisor (Dept of Physics and Astronomy)

[redacted]

Dr G Spence, Outside Member (School of Earth and Ocean Sciences)

[redacted]

Dr K Rohr, External Examiner,
(Pacific Geoscience Centre, Geological Survey of Canada)

Contents

List of Figures

List of Tables

Acknowledgments

I would like to express my gratitude to my graduate supervisor Ross Chapman for his support and guidance during the research which is presented in this thesis I would also like to thank Joe and Stella Scrimger at Jasco Research Ltd for employing me throughout my graduate program I have benefited from working amongst a very talented group of scientists at the Defence Research Establishment Pacific In particular, I would like to acknowledge help from Gary Heard and Ian Schumacher I thank Brian Burger for developing the data storage formats and data tape transcription routines which were used extensively, and for keeping the computers running smoothly Lastly I am grateful to my wife Jacqueline and my children Michelle and Rachael for their support

Chapter 1
Introduction:

The predominant geologic profile of the ocean bottom over the Abyssal Hills region in the North Pacific ocean consists of basalt overlain by a thin sediment layer The extent of this region, where sediment thickness is less than 100 m, is shown in figure 1 1

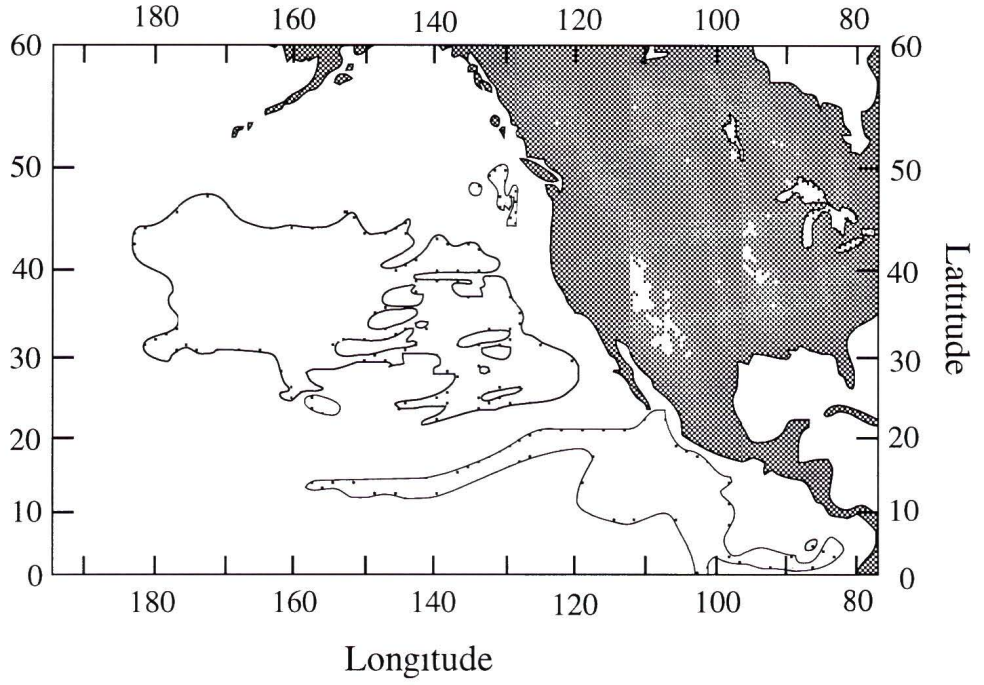

Figure 1 1 Area in the Abyssal Hills region where sediment thickness is less than 100m From (Atwater and Severinghaus, 1989)

A large amount of research effort has been expended to measure the elastic properties of both the sediment and basalt layers in this region Published values for the elastic parameters of the sediment have been obtained mainly from laboratory measurements made on sediment core samples A comprehensive compilation of measurements for this region (Hamilton, 1980) classifies the sediments as pelagic clays, silty-clays, and clayey-silts The sediments are characterized by compressional wave speeds between 1500 m/s and 1530 m/s, and densities between 1 3 g/cm^3 and 1 5 g/cm^3 The experimental measurements, from which these values were determined, were highly consistent from site to site and consequently the limits are well established Less consistent measurements have been obtained for compressional wave attenuation in the

sediment This value is assumed to be in the order of 0 1 dB/λ for frequencies less than 100 Hz, (Hamilton, 1980) Accurate estimation of compressional attenuation from laboratory measurements is very difficult because of its low value Measurements of the sediment shear wave speed and attenuation coefficient have been highly inconsistent, and these properties are also poorly known A compilation of *in situ* shear wave speed versus depth for thicker pelagic sediments (Hamilton, 1976) has indicated a shear wave speed of approximately 100 m/s at the water-sediment interface with a gradient of 4 s^{-1} to 5 s^{-1} in the top 50 m of sediment

Measurements of the geoacoustic properties of the basalt have been made almost exclusively by remote acoustic and seismic sensing rather than by direct sampling This is due mainly to the physical barrier formed by the sediment layer The notable exception is the deep sea drilling project which has provided core samples of the upper crust basalt at many sites in the North Pacific, e g (Christensen and Salisbury, 1975) Cores have indicated densities between 2 0 g/cm^3 and 3 0 g/cm^3, and compressional wave speeds between 3 5 km/s and 6 5 km/s Increasing compressional speed in these cores has been correlated with increasing density

An analysis of sonobuoy refraction surveys at a large number of sites in the Pacific (Houtz and Ewing, 1976) indicated that the upper crust basalt (layer 2) could be divided into three main sub-layers, each with distinctive properties The survey results for compressional wave speed in the uppermost of these sub-layers, (layer 2A), contained a high degree of scatter These data, however, suggested a trend of increasing compressional speed with basalt age from approximately 2 5 km/s in very young crust to 4 5 km/s for crust >40 m y Seismic experiments performed on the East Pacific Rise (Christeson, Purdy, and Fryer, 1992), (Vera *et al* , 1990), (Harding *et al* , 1989) have established very low speeds between 2 2 km/s and 2 3 km/s in layer 2A for young crust near the ridge axis An interesting observation is that compressional wave speeds measured during these experiments have been significantly lower than those measured from core samples at the same locations (Purdy, 1987) The widely accepted explanation for the discrepancies is that large-scale porosity in the basalt, due primarily to cracks and faults, reduces the measured seismic speeds Small changes in large-scale porosity of a few percent have been shown to have significant influence on the compressional wave speed (Wilkins *et al*, 1991) The core samples are generally smaller than the scale of the faults, so measurements on the samples are representative of the speeds in consolidated material An explanation for the increase in compressional wave speed with basalt age, indicated by Houtz and Ewing's data, attributes the increase to decreasing basalt porosity

as cracks and faults in the basalt are gradually filled by minerals precipitated from hydrothermally circulated sea-water (Jacobson, 1992) A study performed at the Juan de Fuca ridge, over a well defined transect of young crust in which basalt age increased from 0 to 4 5 m y , found increasing compressional wave speed with basalt age (Rohr, 1994) Rapid increases in speed were correlated with changes in the regime of hydrothermal circulation from open communication with sea-water, to closed where circulation is limited to the upper basalt and overlying sediment

In this thesis, we present measurements of basalt compressional and shear wave speeds at thin-sediment sites along a track in the North Pacific, for which the geologic age of the basalt increased from 40 my to 63 my These data provide the first test of Houtz and Ewing's results, and Jacobson's theory, along a well defined transect of moderate basalt age The track is significant also because sediment is uniformly thin (<33m) so that open hydrothermal circulation may have continued since the crust was formed The measurements were obtained using a new inversion method which is developed and evaluated in this thesis The method matches reflection loss versus grazing angle values, calculated for many bottom models, to measured data The bottom models are based on a system of two solid layers representing sediment overlying basalt Individual bottom models are described by particular values for the geoacoustic parameters in each of the layers These parameters are varied until the best possible match with measured data is found The parameter set for this optimum model is taken as the estimates for the geoacoustic parameters at the experimental site The method is found to be sensitive to the sediment shear wave speed, the basalt compressional wave speed and the basalt shear wave speed near the sediment-basalt interface The obtained estimates should be more reliable than estimates from existing geophysical techniques which are better suited to measuring the geoacoustic properties in deeper layers

In chapter 2 we describe the inversion method, and we discuss the physics of the important acoustic interactions which influence bottom reflection loss In this discussion we consider acoustic scattering from the ocean bottom, and we propose methods for reducing the scattering effects In chapter 3 we outline a study in which the inversion method was evaluated with simulated data to determine its effectiveness for estimating geoacoustic model parameters This study estimated the sensitivity of the inversion to several model parameters, and investigated the inversion performance in the presence of experimental noise In chapter 4 the method is applied to experimental reflection loss versus grazing angle data obtained at 9 sites along a track in the North Pacific ocean Estimates of the sediment shear wave speed, the basalt compressional wave speed and the

basalt shear wave speed are obtained for each site Finally, in chapter 5, we examine the experimental parameter estimates from chapter 4 and we discuss their implications for crustal aging Chapter 5 also contains some suggestions for related future research

Chapter 2
Inversion of Reflection Loss data

I. Overview

When plane acoustic pressure waves are incident from the water onto the ocean bottom, some of the wave energy is transmitted into the bottom, and some is returned back into the water The returned energy forms an acoustic field which is the sum of signals from reflected and refracted acoustic paths, some of which may have interacted with sub-bottom layers When this is the case, the acoustic field contains information about the geoacoustic properties of the layers The goal of acoustic and seismic inversion methods is to determine the geoacoustic properties of the bottom from the characteristics of the returned acoustic field

Most seismic inversion methods for determining bottom properties in the deep ocean are based on experiments designed to measure variations in bottom reflected and refracted signal properties as a function of the range between a source and receiver, or as a function of the angle of incidence of the seismic energy onto the bottom Commonly employed experiments include the expanding spread profile (ESP), common midpoint (CMP), shot point, and sonobuoy refraction experiments The ESP experiment, *e g* (Harding *et al* , 1989) and (Vera *et al* , 1990), is performed using two ships One of the ships tows a receiver in the opposite direction to the other ship, which tows an impulsive-type source or deploys explosive charge sources Both ships start from a common location and sail at the same speed so that the midpoint between the ships remains fairly constant As the ships move apart, the source is repeatedly fired so that bottom reflected signals, measured at the receiver, are recorded for a range of incidence angles The CMP experiment, *e g* (Rohr, 1994), is performed using only one ship for towing the receiver and deploying the sources The receiver for this experiment contains multiple in-line elements, and is towed far enough behind the ship so that sources can be fired or detonated between the ship and the frontmost element Because the receiver has spatial extent, the angle of incidence for the bottom reflected signals measured on different elements is not constant and the range of angles increases with the length of the receiver The signals from multiple shots are combined, and the forward movement of the sources and receiver elements are accounted for to obtain a range of incidence angle measurements for signals reflected from common positions on the bottom Shot point experiments, *e g* (Christesen, Purdy and Fryer, 1992) and (Purdy, 1987), are performed

using one or more receivers mounted on or close to the ocean bottom Sources are fired or detonated at varying range from the receivers so that a range of reflection or refraction angles from sub-bottom layers is obtained A benefit of this method is that it avoids contamination of the data by ocean surface multiples, which can arrive at the receiver simultaneously with the bottom refracted signals of interest Additionally, ocean bottom seismometers (OBS's) can be used in place of hydrophones The OBS receiver resolves the direction of particle displacement in the solid bottom so that wave polarizations can be resolved The sonobuoy refraction experiment, *e g* (Houtz and Ewing, 1976), is carried out by deploying a sonobuoy which suspends a hydrophone receiver The sonobuoy can contain signal recording hardware, or it can broadcast the hydrophone data to a ship The ship meanwhile deploys sources at varying range from the sonobuoy to obtain data similar to that of the ESP experiment, except that the bottom reflection point is not fixed

Inversion methods can be classified in three main categories travel time methods, amplitude methods, and full waveform methods Travel time methods exploit the time differences between refracted acoustic arrivals as the source-receiver range changes The time differences are related to the compressional and shear wave speeds in the layers between interfaces from which individual arrivals are observed The travel time method is applied by using a forward seismic propagation algorithm to calculate theoretical arrival time differences for a geoacoustic model which approximates the bottom media The wave speeds in the model are varied until the best match between modeled and observed arrival time differences is achieved In the most commonly implemented case, the bottom is modeled as a system of layers in which the wave speeds in each layer are constant, or vary linearly with depth only Inversion wave speed estimates in oceanic crust using this method have been presented in several papers, *e g* (Vera *et al* 1990) and (Harding *et al* , 1989) The method has been extended to two dimensions (Zelt, 1992) and three dimensions (Toomey, 1990) These higher dimensional methods require more sophisticated forward seismic propagation algorithms to predict theoretical arrival times

Amplitude methods are applied to data in similar manner to travel time methods but the arrival amplitudes, rather than arrival time differences, are the feature of interest The amplitudes of reflections from a specific interface are related to the reflection coefficient at the interface The reflection coefficient is, in turn, a function of the compressional and shear wave speeds and attenuation coefficients, and the densities in the layers on both sides of the interface, as well as the angle of incidence of the seismic energy The reflection coefficient and angle of incidence at each identifiable interface are determined and then inverted to obtain the geoacoustic parameters of the layers at the

respective interface This method has been applied to invert upper crustal speeds in ~140 m y crust (Rohr, 1987), and in very young crust near the Juan de Fuca ridge, (Rohr, Schmidt, and Groschel-Becker, 1993)

The full waveform method, *e g* (Singh et al, 1989) and (Sen and Stoffa, 1991) matches the full measured refraction waveform (seismogram) to theoretically modeled waveforms (synthetic seismograms) which are calculated by a forward propagation algorithm The parameters, describing the model for which the synthetic seismograms are calculated, are varied until the best match between the measured and synthetic seismograms is achieved The application of this method is generally difficult because the incident waveform must be used in the calculation of the returned synthetic seismograms Additionally, the forward model must provide a broadband transfer function for the bottom models, and the matching of the synthetic and measured seismograms is not straight-forward

The above inversion methods, except for the full waveform method, are not well suited to provide accurate estimates of geoacoustic parameters in thin bottom layers (<50 m), or in layers defined by interfaces across which the acoustic impedance mismatch is small Errors in sound speed estimates from travel time methods are proportional to errors in the arrival time difference measurements For thin layers, the arrival time differences are small, so large sound speed estimate errors occur Also, when the arrival time difference is small, the individual reflection signals can overlap The overlap of the signals introduces error in the amplitude measurements which are required by the amplitude methods Both the travel time and amplitude inversion methods rely on the ability to identify reflections from individual interfaces When the acoustic impedance mismatches across interfaces are small, the reflected signals have low amplitudes This makes identification of the reflected signals difficult, especially in the presence of scattering noise

A new inversion method, based on a modified ESP experiment, for estimating geoacoustic parameters of uppermost oceanic crust in regions of thin sediment cover (<50 m) is developed in this thesis The method was developed specifically for estimating the geoacoustic properties of the sediment and upper basalt (layer 2A) over large areas of the Abyssal Hills region in the North Pacific These areas are characterized by a thin layer of pelagic sediment (<50 m) overlying basalt Bottom roughness is generally large, and bottom reflected signals usually contain significant scattered energy, which partially obscures signals from reflecting interfaces Also, the upper basalt generally lacks strongly reflecting interfaces in the top few hundred meters Because of

the thin sediment layer and lack of reflecting interfaces in the upper basalt, the travel time and amplitude methods are not suited to provide accurate estimates for the geoacoustic parameters in this environment

The inversion method uses bottom reflection loss versus grazing angle data It is found that the reflection loss, in the Abyssal Hills environment described above, is strongly influenced by the geoacoustic properties of the sediment and basalt near the sediment-basalt interface The reflection loss is calculated from the total energy, in selected frequency bands, of the entire returned waveform so that no separation of the individual arrivals in the waveform is required Reflection loss is defined as the ratio of the reflected energy to the total incident energy Although it is closely related to the reflection coefficient, the reflection loss is a real quantity, defined for specific frequency bands, while the reflection coefficient is generally a complex function of frequency The reflection loss (h) for a frequency band defined by band edges f_1 and f_2 is also a function of the incident wave power spectrum and is given by

$$h = \frac{\int_{f_1}^{f_2} |P(f)|^2 |R(f)|^2 \, df}{\int_{f_1}^{f_2} |P(f)|^2 \, df} \qquad (2\ 1)$$

where $|P(f)|^2$ is the incident wave power spectral density function, and $R(f)$ is the complex reflection coefficient If the incident wave power spectrum is constant over the band, the reflection loss is the average square modulus of the reflection coefficient in the band The reflection loss is more commonly expressed in decibels by $H = -10 \log(h)$

The proposed inversion method belongs to a class of inversion methods known as iteration of forward models (Frisk, 1990), (Chapman, 1991) These methods work by matching certain characteristics of the data, with those predicted for a model which simulates the geoacoustic bottom environment The approach requires theoretical computation of the characteristic of interest for many possible bottom models For our inversion method, the characteristic of interest is the bottom reflection loss at several grazing angles A cost function is defined to indicate the fit between theoretical results, for individual bottom models, and the data This function is minimized to find the bottom model which best reproduces the measured reflection loss versus angle characteristics The geoacoustic parameter values describing this optimum model are taken as the estimates for the values at the experiment site

II. Reflection Loss Model

In general, the reflection coefficient is dependent on the frequency, the geoacoustic properties of both the sediment and the basalt, and the angle of incidence of the waves onto the bottom The important geoacoustic parameters are the compressional wave speeds (C_p), the shear wave speeds (C_s), the compressional attenuation coefficients (α_p), the shear attenuation coefficients (α_s), and the densities (ρ) in both the sediment and basalt Because of the great water depths over the Abyssal Hills region, (generally greater than 5 km), curvature of the wavefronts near the bottom for acoustic energy generated by point sources near the ocean surface is very small for frequencies as low as a few Hz Consequently, a plane wave treatment of the interaction of the waves with the bottom is an excellent approximation Plane wave reflection coefficients can be numerically evaluated for a system of solid homogeneous layers analogous to the sediment and basalt bottom layers, (Brekhovskikh, 1980) The numerical method of Brekhovskikh is a full wave solution of the wave equation for the system of solid layers It assumes that layer interfaces are smooth and planar, and that compressional and shear waves are coupled only at the interfaces Brekhovskikh's outline contains several errors which have been corrected in the outline of the method given in Appendix B of this thesis Furthermore, the method has been extended to include both compressional and shear wave attenuation in each layer This method has been implemented for the water-sediment-basalt model in a FORTRAN routine which is included at the end of Appendix B This routine was used to calculate modeled reflection coefficients at several frequencies within the frequency band of interest Reflection losses were calculated from these reflection coefficients using equation 2 1

The ocean bottom for the Abyssal Hills environment is represented by the 2-layer elastic solid model shown in figure 2 1 We describe the set of possible geoacoustic models by a vector **m** whose components are the geoacoustic parameters in the layers $\mathbf{m} = \{\rho^S, C_p^S, C_s^S, \alpha_p^S, \alpha_s^S, \rho^B, C_p^B, C_s^B, \alpha_p^B, \alpha_s^B\}$, where the superscripts S and B indicate respectively whether the parameter represents the value in the sediment layer or in the basalt layer Note that **m** spans a region of 10 dimensional space which is defined by the allowed ranges for each of the parameters

Water	C_p, ρ
Sediment	C_p^S, α_p^S C_s^S, α_s^S ρ^S
Basalt	C_p^B, α_p^B C_s^B, α_s^B ρ^B
no lower boundary	

Figure 2 1 Geoacoustic model for thin sediment bottom

The proposed inversion method searches for the model which optimizes the fit between the measured reflection loss versus angle data $H_D(\theta)$, and the modeled data $H_M(\mathbf{m},\theta)$ The parameter values for this model are the estimates for the actual parameters at the experiment site It is noted that some of the parameters comprising **m** may have little influence on the loss curve and thus could be removed from the search space thereby reducing its dimension

III. Reflection Loss Versus Angle Characteristics

Reflection loss versus grazing angle data for the two layer profile, representing a typical Abyssal Hills geoacoustic environment, have distinguishing features which can be attributed to the behavior of individual acoustic paths, (Chapman and Chapman, 1993) It is useful to approach the physical problem by considering the interaction of the incident acoustic energy with the bottom, using "rays" to illustrate the important acoustic paths The diagram in figure 2 2 shows the important rays which are responsible for the majority of the structure in the reflection loss curves Rays for compressional waves are depicted by solid lines while rays for shear waves are depicted by dashed lines, and the important rays are numbered for later reference

The incident ray arrives from the water on the left in figure 2 2 This ray interacts with the water-sediment interface, where it is partially reflected (ray 1) and partially transmitted (ray 2) Because the reflection coefficient at this interface is low, most of the energy is transmitted The compressional wave speed in the sediment in this example is slightly lower than in the water Consequently, by Snell's law, ray 2 propagates at a slightly steeper angle than the rays in the water When ray 2 reaches the sediment-basalt interface, a fairly complex interaction occurs Here it is partially reflected into the sediment (ray 4), and partially transmitted into the basalt (ray 7) Additionally the interaction initiates a transmitted shear wave in the basalt (ray 6), and a reflected shear wave in the sediment (ray 3)

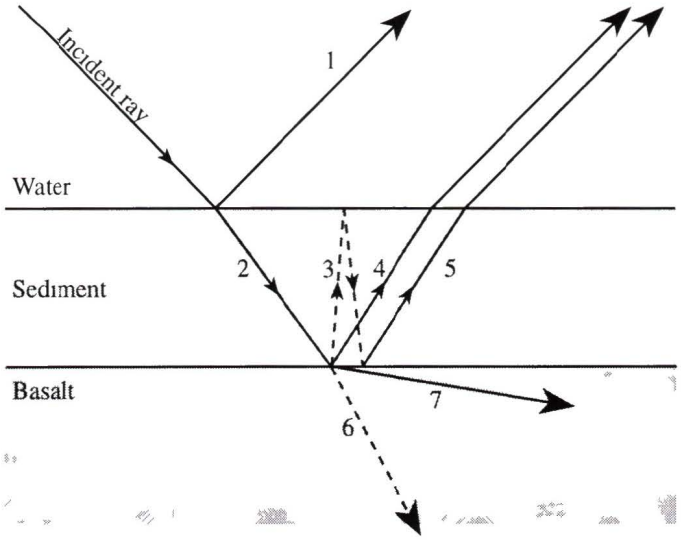

Figure 2 2 Important rays for the two layer geoacoustic interaction for a typical thin sediment Abyssal Hills environment

The relative slopes for rays 6 and 7 represent the case where the basalt shear wave speed is less than the sediment compressional speed which, in turn, is less than the basalt compressional wave speed Because the shear wave speed of the sediment is very low (typically 100 m/s - 200 m/s), ray 3 propagates in a nearly vertical direction for all incident ray angles The wave depicted by this ray is almost totally reflected back into the sediment at the sediment-water interface, with a phase change of 180° The reflected shear wave then propagates back down to the sediment-basalt interface, where it is partially re-converted to a compressional wave in the sediment (ray 5) Rays 4 and 5 propagate back up to the sediment-water interface where they are mostly transmitted back into the water The interference between these rays produces much of the structure in the reflection coefficient, and ultimately in the reflection loss versus angle data

We first consider the form of the reflection loss versus grazing angle for a geoacoustic environment consisting of a thin sediment layer overlying a higher speed basalt layer The plot in figure 2 3 shows reflection loss, in decibels, versus grazing angle and frequency for the geoacoustic profile which was used to generate test data for the simulation study in chapter 3 The parameter values describing this profile are given in table 3 1 Figure 2 3 was generated using the reflection loss routine given in Appendix B The frequency bandwidth for the reflection loss in figure 2 3 was set to zero, so the values are actually the modulus squared of the reflection coefficient, expressed in dB

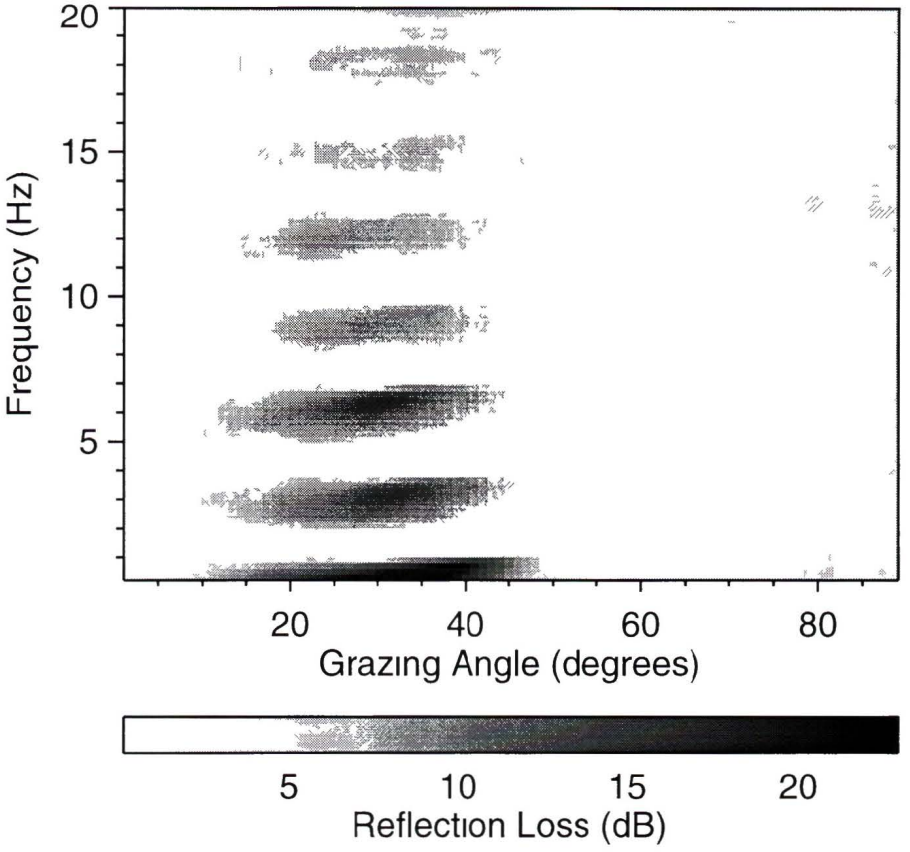

Figure 2 3 Reflection loss versus grazing angle and frequency

The most striking feature in figure 2 3 is the modulation of reflection loss with frequency which is evident from ≈3-55° grazing angle Over this spread of angles, strong conversion of the compressional energy in ray 2, (of figure 2 2), to shear energy in ray 3 occurs This leads to the doubly converted ray 5 having significant amplitude The observed modulation is due to the strong interference between rays 4 and 5 By noting that the total phase difference (ϕ) between rays 4 and 5 occurs in the two-way sediment path of shear wave ray 3, we can predict the period of modulation in frequency based on

the sediment thickness and the shear wave speed The total phase difference is $\phi = 4\pi d / \lambda + \pi$, where d is the sediment thickness and λ is the shear wave wavelength in the sediment The modulation pattern repeats every time the phase difference changes by 2π We obtain the relationship

$$\begin{aligned} \Delta\phi &= \phi(f_2) - \Delta\phi(f_1) \\ &= 4\pi d f_2 / b - 4\pi d f_1 / b \\ &= 2\pi, \end{aligned} \qquad (2\ 2)$$

where b is the sediment shear wave speed Solving, we get $f_2 - f_1 = b / 2 d$ The values used for b and d for calculating the loss in figure 2 3 were 180 m/s and 30 m respectively This gives $f_2 - f_1 = 3$ Hz We note that the modulation pattern in figure 2 3 repeats every 3 Hz An additional observation pertaining to the modulation is that the modulation amplitude decreases with increasing frequency This effect is due to the shear wave attenuation in the sediment, which increases with frequency The increasing attenuation rapidly decreases the amplitude of ray 3 before it converts to ray 5 Consequently, the amplitude of interfering ray 5 also decreases with frequency The modulation of reflection loss was found to be negligible for frequencies greater than 50 Hz when shear wave attenuation was specified at 1 5 dB/λ

The second notable feature of the loss versus angle and frequency is the very low reflection loss occurring near 56° grazing angle for all frequencies This angle is the incident ray grazing angle for which the basalt compressional wave (ray 7) becomes horizontal, and is referred to as the basalt compressional wave critical angle If no shear wave was supported in the basalt, then total internal reflection of the acoustic energy, incident from the sediment, would occur for angles less than the critical angle The critical angle can be calculated from Snell's law by setting the grazing angle (θ_B) for ray 7, to zero If θ_C represents the critical angle for incident ray, then by Snell's law,

$$\frac{\cos\theta_C}{C_W} = \frac{\cos\theta_B}{C_B}, \qquad \theta_B = 0 \qquad (2\ 3)$$

where C_W is the water sound speed, and C_B is the basalt compressional speed The profile used for figure 2 3 had $C_W = 1540$ m/s and $C_B = 2800$ m/s This gives $\theta_c = 56\ 6°$, which agrees well with the peak in figure 2 3

IV. Rough Bottom Scattering Effects

One disadvantage in modeling the bottom as a smooth planar interface is that the effects of bottom roughness are ignored In practice, bottom roughness is always present, and causes some degree of non-specular scattering of the incident waves The diagram in figure 2 4 shows how energy, incident at the specular angle onto a rough bottom, can be scattered over a range of angles

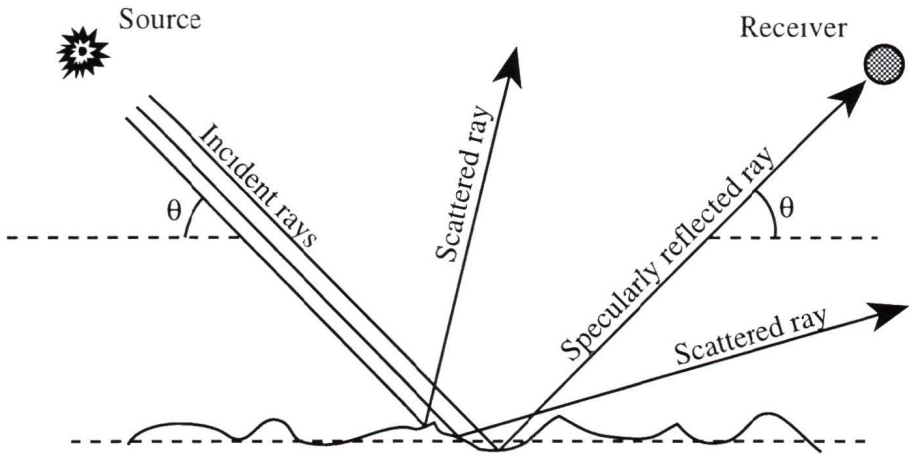

Figure 2 4 Scattering away from the specular direction

The energy lost to the scattered rays leads to a reduction of the amplitude of the specularly reflected signal If the magnitude of bottom roughness (s) is sufficiently small, and can be described by a Gaussian distribution of elevations, the loss (H_E) due to scattering can be calculated according to the Eckart scattering law, (Diachok *et al*, 1994)

$$H_E = \exp(-2g^2) \tag{2 4}$$

where k is the wave number, $g = 2ks \sin(\theta)$, and θ is the grazing angle We note from equation 2 4, that the scattering effects increase with grazing angle and frequency Analysis of the reflection data for the experiment described in chapter 4 indicated that scattering effects were significant at the sites studied Because the amplitude of bottom roughness may vary significantly over small distances, and the roughness may be of non-Gaussian form, it is difficult in practice to accurately estimate the magnitude of scattering loss in real reflection data For these reasons, the analysis of the reflection loss data was restricted to low frequencies so that scattering effects were minimized For the simulation study in chapter 3, and analysis of real data in chapter 4 analysis was performed for a 1/3 octave band centred at 8 Hz with band edges at 7 08 Hz and 8 91 Hz

V. Reflection Loss Experiment

Bottom reflection loss versus grazing angle measurements are generally made using impulsive type waveforms so that signals from a specific reflection path can be isolated from waterborne and other multiply reflected paths The reflected signal is measured by a receiver located at varying distance from the source, to provide a range of grazing angles The energy level in dB measured at the receiver (L) is assumed to be equal to the source level (SL) less the spreading loss (H_S) and the bottom reflection loss (H_B) If a calibrated source is used, and spreading loss can be predicted, the bottom loss is obtained by

$$H_B = SL - H_S - L + 6\ 02 \qquad (2\ 5)$$

The 6 02 dB accounts for the combined additive energy of the four separate acoustic paths present in the bottom-reflected waveform, i e $10 \log(4) = 6\ 02$ The paths are the source-bottom-receiver, source-surface-bottom-receiver, source-bottom-surface-receiver, and the source-surface-bottom-surface-receiver Since the source and receiver are close to the ocean surface, the arrivals from these paths are difficult to isolate from each other because their time separation is usually comparable with the impulsive source waveform duration

Values obtained for bottom loss using this approach, however, may not be representative of the reflection loss as defined previously The reason for this is that the total energy measured at the receiver may result from scattered in addition to specularly reflected acoustic paths When bottom roughness is present, a component of the full sound field at the receiver is due to scattering from within a region around the specular reflection point Figure 2 5 shows a representation of the scattering region for the general source-receiver geometry This region is a result of facet-like scattering, and is not related to the Fresnel zone The size of the significant scattering area, and the magnitude of the scattered energy increase with increasing bottom roughness and frequency

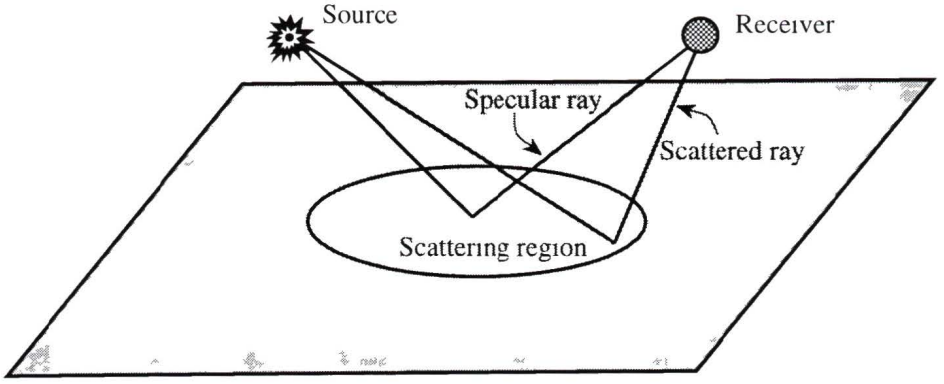

Figure 2 5 Rough bottom scattering region

The scattered component of the sound field at the receiver is unwanted for our modeling purposes Unfortunately, this component cannot be isolated from the specular component when non-directional receivers are employed Therefore, it is necessary to use an array of hydrophones to spatially filter the scattered component We have used a towed horizontal line array for this purpose Plane wave beamforming of the towed array outputs is well suited for the signal processing due to the small wavefront curvatures mentioned previously The plane wave beam pattern for line arrays is conical with the axis of the cone along the array If the bottom and array are both horizontal, the intersections of the conic beams with the planar bottom are hyperbolas Figure 2 6 shows the bottom intersection of one of these beams passing through the scattering region of figure 2 5 Beam intersection with the bottom is indicated by the area inside the dashed lines The region where the intersection passes through the scattering region is indicated by the darkly shaded area

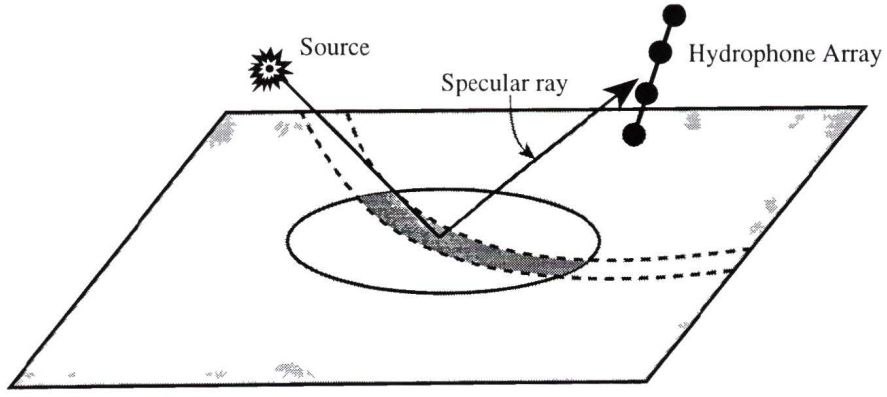

Figure 2 6 Line array beam intersection with the bottom and scattering region

Because the beamformer rejects energy incident from angles other than the beam direction, much of the energy from the scattering region can be filtered out The beam however admits energy from the area where it intersects the scattering region as indicated in Figure 2 6 This smaller region of intersection will still contain the specular reflection, resulting in a much smaller ratio of scattered energy to reflected energy

VI. Cost Function Minimization

To use the method, a set of data, consisting of measurements of low frequency reflection loss at N different grazing angles, is required This set of measured reflection loss data is denoted $M(\theta_i)$, $i = 1 \quad N$, where the loss values are in linear units An energy or cost function $E(\mathbf{m})$ is defined which indicates the degree of mismatch between the measured reflection losses and the reflection losses predicted for model **m** The proposed function is the rms point to point difference between the square roots of the measured and modeled loss data

$$E(\mathbf{m}) = \left[\frac{1}{N} \sum_{i=1}^{N} \left[\sqrt{M(\theta_i)} - \sqrt{R(\mathbf{m}, \theta_i)} \right]^2 \right]^{\frac{1}{2}} \tag{2 6}$$

A perfect match between the measured and modeled data is indicated by $E(\mathbf{m}) = 0$ The inversion is then formulated as a multi-dimensional optimization problem in which we wish to minimize $E(\mathbf{m})$ This minimization is non-trivial because $E(\mathbf{m})$ is generally a non-linear function which can have several sub-optimal or local minima This feature precludes the use of calculus based minimization techniques Additionally, the search space is very large so that exhaustive searching of a discretized space of adequate resolution is not possible in a reasonable amount of time with currently available computer capabilities For these reasons, the efficient optimization technique Simulated Annealing (Press *et al*, 1986) is employed to search for the optimum model This method has also been used recently for full waveform matching of measured and synthetic seismograms, (Sen and Stoffa, 1991) When the optimum model is found, the parameters describing it are used as the estimates for the actual parameter values at the experiment site

Simulated Annealing (SA) is based on an analogy with the annealing process of metallurgy, whereby molten metal is cooled slowly so that it crystallizes in a very low energy state The SA algorithm is an iterative technique which repeatedly perturbs the parameter values comprising a model, and accepts or rejects the perturbed model based

on the change of the cost function value The process is controlled by a parameter T, analogous to temperature, which is slowly reduced (cooling) During the inversion, the algorithm keeps track of an accepted model $\mathbf{m}_a$, and the associated value of the cost function $E(\mathbf{m}_a)$ A new model $\mathbf{m}_n$ is determined by perturbing one or more of the parameters in $\mathbf{m}_a$, and the change in the cost function, $\Delta E = E(\mathbf{m}_n) - E(\mathbf{m}_a)$, is calculated Perturbations which decrease E are always accepted Perturbations which increase E are accepted with a probability that is proportional to the Boltzman distribution

$$P(\Delta E) = \exp(-\Delta E / T) \tag{2 7}$$

Because the algorithm allows probabilistic acceptance of increases in cost, it has the ability to escape from sub-optimal or local minima in the cost function As T decreases, the probability that an increase in cost is accepted becomes smaller If T is reduced slowly, the algorithm will move out of small local minima, and will avoid regions in the parameter search space where the cost is high If, however, T is reduced too quickly, the algorithm can become trapped in sub-optimal minima and the inversion will fail The initial value of T, and the rate at which it is reduced is referred to as the annealing schedule The annealing schedule is problem specific, and is usually determined by trial and error after running the algorithm several times on a similar problems

VII. Summary

Water depths in the Abyssal Hills region of the North Pacific are often greater than 5 km The direct measurement of properties of the ocean bottom in these areas is usually precluded by the great depth[1] As a result, most of the data collected have been by remote acoustic sensing using geophysical techniques, whereby acoustic signals are directed toward the ocean bottom and the reflected and refracted acoustic signals are measured Properties of the bottom and sub-bottom layers are then inferred from the characteristics of these returned signals Unfortunately, the currently available geoacoustic methods are not well suited for measuring the properties of the sediment and upper basalt layers at thinly sedimented sites (<50 m)

The inversion method developed in this thesis was designed specifically for regions where sediment thickness is relatively thin The method is superior to the existing methods for these regions mainly because it does not require that signals from closely spaced reflecting interfaces be resolved, (most importantly, the water-sediment and

[1]A notable exception is the deep sea drilling project, e g (Christensen and Salisbury, 1975)

sediment-basalt interfaces) It, in fact, exploits the interference between these signals This interference is especially dependent on the shear wave properties of the sediment as described in section III Additionally, the use of a beamformed towed line array is necessary for reducing the unwanted scattered component in the reflected signal An additional benefit of beamforming is that it can reject low frequency energy which is reflected or refracted from deeper layers of basalt where sound speeds are known to be higher than the surface speeds This type of refracted energy is not resolvable by non-directional receivers, and is a possible source of error for measurements of the properties of the upper ocean bottom layers using the current methods

Chapter 3
Simulation Study

Simulated reflection loss data are used to demonstrate the inversion method and to determine its effectiveness for estimating the elastic properties of the basalt and pelagic sediment in a typical abyssal hills thin-sediment environment The simulation study investigates the effects of individual parameters on the reflection loss, and examines the sensitivity of the cost function to each of the parameters The study indicates that three of the parameters sediment shear wave speed, and basalt compressional and shear wave speeds are significantly more sensitive than the remainder of the parameters Effects of experimental error on the inversion estimates are investigated by introducing random errors in the simulated data Whereas all parameter estimates are good in the absence of noise, the errors for the insensitive parameters are found to be large when noise is present Estimates for the three most sensitive parameters, however, are only slightly degraded in the presence of noise The study concludes that the method can provide useful estimates for the three sensitive parameters from experimental data

I. Test Data

For testing the inversion method, a set of reflection loss versus grazing angle data in a 1/3 octave band centred at 8 Hz were generated for a specific thin-sediment geoacoustic profile under the assumption that the incident wave power spectrum is constant over the band The specific profile used for the test data will be referred to as the true environment, which is described by the parameter values in table 3 1 The sediment thickness was fixed at a value of 30 m Data for this environment were calculated at 40 separate grazing angles between 7° and 85° in 2° increments

Table 3 1 Parameter values for "True" environment

Layer	C_p (m/s)	C_s (m/s)	α_p (dB/λ)	α_s (dB/λ)	ρ(g/cm^3)
Water	1540	-	-	-	1 0
Sediment	1535	180	0 1	1 5	1 3
Basalt	2800	1100	0 3	0 5	2 3

To simulate the circumstances of a real experiment, a range of possible values for each of the parameters was specified These ranges would normally be representative of

the apriori knowledge about the respective parameters Here we use the approximate ranges of values for the parameters of the abyssal hills environment (Hamilton, 1980), which are listed in table 3 2

Table 3 2 Geoacoustic model parameter ranges

Layer	C_p (m/s)	C_S (m/s)	α_p (dB/λ)	α_S (dB/λ)	ρ (g/cm^3)
Sediment	1520-1540	100-200	0 0-0 2	1 0-3 0	1 2-1 4
Basalt	2600-3000	900-1400	0 0-0 5	0 0-1 0	2 0-2 5

II. Parameter Sensitivity

The degree to which the cost function changes, due to a change in a particular geoacoustic model parameter, is not the same for all parameters Because the cost function is a measure of mismatch between the measured and predicted reflection loss, its sensitivity to individual parameters is related to how the respective parameter influences the reflection loss Because the parameters are restricted to finite ranges, we are interested only in the influences within the ranges We investigate the sensitivity for each parameter by first considering how the parameter influences the reflection loss versus angle curve Then we consider the effects on the cost function itself by examining its dependence on the individual parameters Finally, we obtain a general sensitivity estimate by calculating the average variance of the cost function due to varying the individual parameters at many random positions in the parameter search space

A. Reflection Loss Curves

In order to gain an understanding of the sensitivity of the cost function, it is useful to investigate how the shape of the reflection loss curve changes when the individual geoacoustic model parameters are varied Because the cost function is a direct measure of the rms difference between the square root of the measured data and the modeled reflection loss, we will plot the square root of reflection loss versus grazing angle rather than the reflection loss itself This is desirable also because the square root of the reflection loss has similar characteristics to the familiar reflection coefficient For a single frequency, the square root of reflection loss is, in fact, the magnitude of the reflection coefficient We will refer to the square roots of the 1/3-octave reflection losses as "equivalent reflection coefficients" for the frequency band Figure 3 1 contains equivalent reflection coefficient curves, in which one parameter has been purposely

displaced from its true value to the lower and upper values in its allowed range The dotted lines are the curves for the respective parameters at the lower range values, the dashed curves represent the parameters at the upper values, and the solid lines are for the true values Note that all parameters, other than the perturbed ones, are fixed at their true values

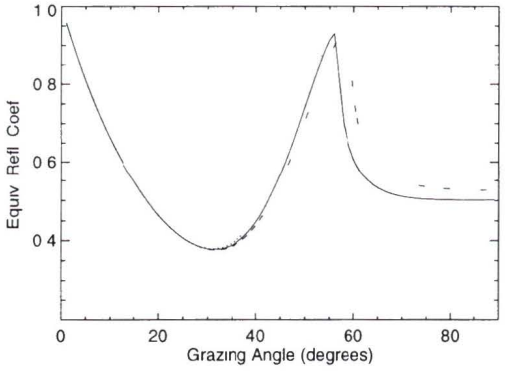

a) Basalt compr wave speed C_p=2600 m/s ( ), C_p=2800 m/s (—), and C_p=3000 m/s (---)

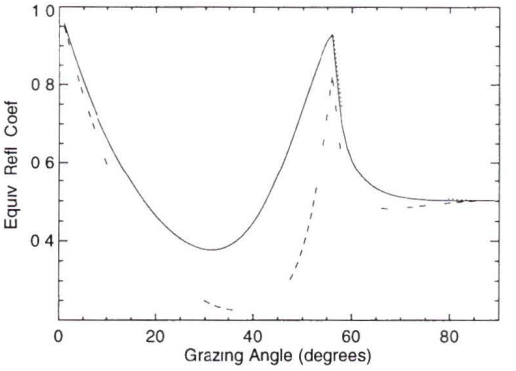

b) Basalt shear wave speed C_S=900 m/s ( ), C_S=1100 m/s (—), and C_S=1400 m/s (---)

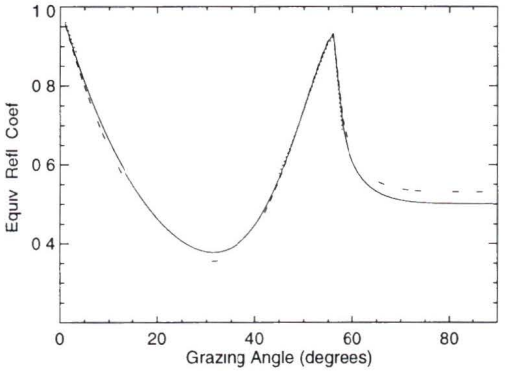

c) Basalt density ρ=2 0 g/cm^3 ( ), ρ=2 3 g/cm^3 (—), and ρ=2 5 g/cm^3 (---)

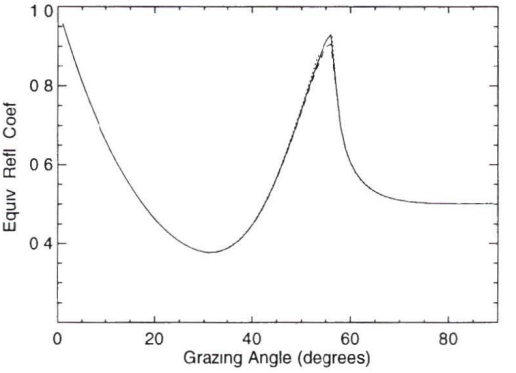

d) Basalt compr atten α_p=0 0 dB/λ ( ), α_p=0 3 dB/λ (—), and α_p=0 5 dB/λ (---)

Figure 3 1 Equivalent reflection coefficient versus grazing angle curves at lower, true, and upper parameter range values

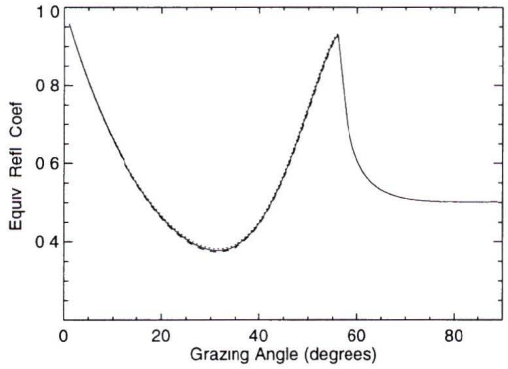

e) Basalt shear atten α_S=0 0 dB/λ ( ), α_S=0 5 dB/λ (—),and α_S=1 0 dB/λ m/s (---)

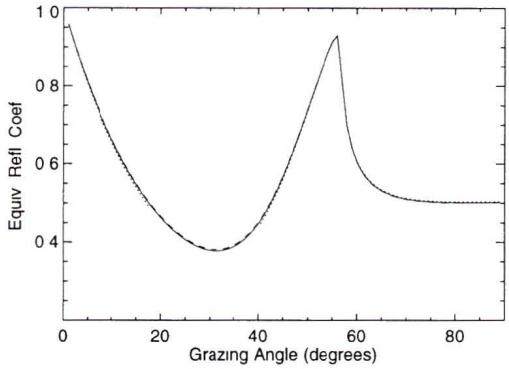

f) Sediment compr speed C_p=1520 m/s ( ), C_p=1525 m/s (—), and C_p=1540 m/s (---)

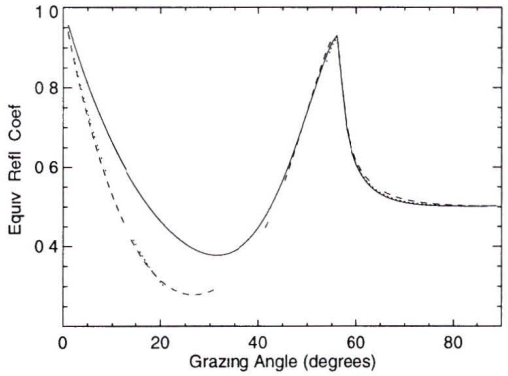

g) Sediment shear speed C_S=100 m/s ( ), C_S=180 m/s (—), and C_S=250 m/s (---)

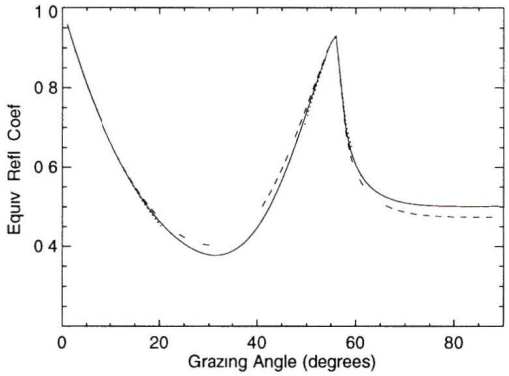

h) Sediment density ρ=1 2 g/cm^3 ( ), ρ=1 3 g/cm^3 (—), and ρ=1 4 g/cm^3 (---)

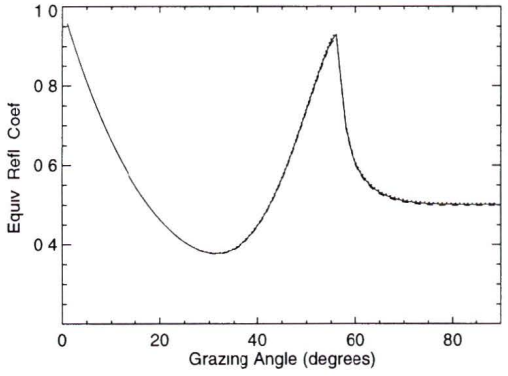

ı) Sediment compress atten α_p=0 0 dB/λ ( ), α_p=0 1 dB/λ (—), and α_p=0 2 dB/λ (---)

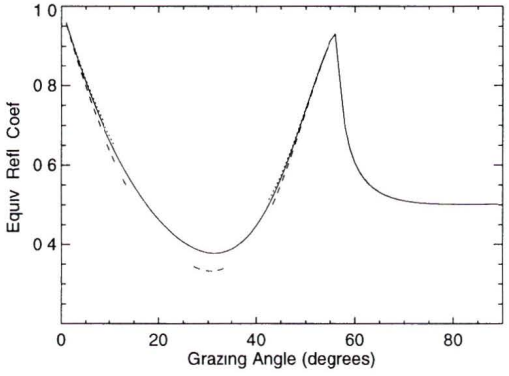

ȷ) Sediment shear attenuation α_S=1 0 dB/λ ( ), α_S=1 5 dB/λ (—), and α_S=3 0 dB/λ (---)

Figure 3 1 Continued

We note from figures 3 1 (a to j), that several of the parameters have very little influence on the reflection loss In particular the equivalent reflection coefficient versus angle curves at differing values for basalt compressional attenuation (figure 3 1 d), basalt shear attenuation (figure 3 1 e), sediment compressional speed (figure 3 1 f), and sediment compressional attenuation (figure 3 1 i), are nearly indistinguishable from each other This observation suggests that the inversion method will not produce useful estimates for these four parameters Additionally, three of the remaining parameters show only moderate influence on reflection loss These are basalt density (figure 3 1 c), sediment density (figure 3 1 h), and sediment shear wave attenuation (figure 3 1 j) Lastly, the three parameters basalt compressional speed, basalt shear speed, and sediment shear speed, (figures 3 1 a,b,g respectively) cause considerable change of shape of the equivalent reflection coefficient curves when they are varied through their respective ranges

It is important to consider the form of the equivalent reflection coefficient curve change in addition to the magnitude of the change Errors in the inversion estimates can arise if different parameters effect the reflection loss in similar ways The manner in which this occurs is illustrated by referring to figures 3 1 c and 3 1 h which show equivalent reflection coefficient versus angle curves for basalt density and sediment density We note that a decrease in the basalt density creates a change in reflection loss very similar to that obtained by increasing the sediment density This effect is explained by the fact that the reflection coefficient, for rays incident onto the sediment-basalt interface, is related to the acoustic impedance contrast across the interface Since the impedance in each layer is proportional to the density, decreasing the basalt density and increasing sediment density both reduce the impedance contrast Consequently, an ambiguity in the cost function minimum arises, where many combinations of the densities provide nearly identical reflection loss versus angle characteristics The minimization of the cost function during inversion for example, may locate the minimum where both the basalt density and sediment density are less than the correct values Although the density estimates would be invalid, the impedance mismatch would be correct This is a case where re-parameterization of the cost function search space could be useful Here we might replace the sediment density and basalt density parameters by a single parameter representing their ratio, however this was not investigated

The effects due to basalt shear attenuation, sediment compressional speed and sediment compressional attenuation are very small and similar Additionally, the form of the changes is similar to that of the more important sediment shear wave attenuation Consequently the problem of ambiguity, described above, will occur here also

Varying the basalt compressional attenuation causes a small change to the amplitude of the equivalent reflection coefficient in a small grazing angle range close to the basalt compressional critical angle peak This peak occurs near 55° grazing angle in all curves The variation is small, but it is distinct from the effects of varying the other parameters

Varying the basalt compressional wave speed produces a change in the compressional critical angle that coincides with the sharp peak in the curves This distinct feature in the reflection loss versus angle curve allows direct estimation of the basalt compressional speed by simply locating the angle of the peak and using equation 2 3, (Diachok, 1994) The speed estimate obtained by this direct method can be used to position the search interval used by the iterative inversion method The inversion method should provide a more accurate estimate by exploiting the full shape of the loss versus angle data around the peak

Varying the sediment shear wave speed directly influences the phase change incurred by the shear wave which propagates on a two-way path through the sediment layer This phase change is proportional to the ratio of sediment thickness to the shear wave wavelength, and therefore is proportional to frequency and inversely proportional to shear wave speed as was shown in Chapter 1 section III The total phase change, incurred by the sediment shear wave, controls the interference which is manifested by the low equivalent reflection coefficients over the grazing angles between approximately 3° and 55°

Varying the basalt shear wave speed changes the grazing angle of the minimum between approximately 20° and 40° in figures 3 1 The low equivalent reflection coefficients around the minimum result from sediment shear wave interference The minimum occurs at the angle of maximum compressional to shear wave conversion at the sediment basalt interface This angle increases with increasing basalt shear speed Secondly, the change in the parameter modifies the phase change incurred upon compressional to compressional wave reflection at the sediment-basalt interface The

reflected compressional wave is one of the two main acoustic paths whose interference causes the low reflection coefficients The relative phase of the interfering paths is thus changed, resulting in a change in the amplitude of the minimum

Analysis of the changes in reflection loss versus grazing angle, due to varying the geoacoustic parameters, indicates that the three parameters basalt compressional wave speed, basalt shear wave speed, and sediment shear wave speed are the only parameters which influence the reflection loss strongly and uniquely The conclusion of this analysis is that reliable estimates can be obtained only for these parameters using the proposed inversion method

B Cost Function Sensitivity

A different approach, for investigating the ability of the method to estimate individual parameters, is to consider how the parameters affect the cost function near the global minimum The global minimum occurs when all the model parameters are set exactly to the true values For our simulated experimental data, with no noise, the cost function is exactly zero at the global minimum We can obtain projections of the cost function near this minimum by plotting the function versus one parameter at a time, with the remaining parameters fixed at their true values Projections of this kind are shown in figures 3 2 (a to j)

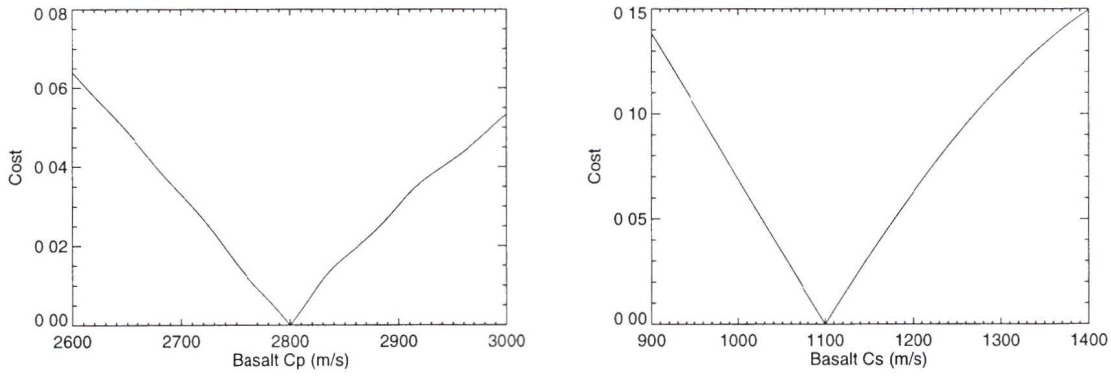

a) Basalt Compression Speed

b) Basalt Shear Speed

Figure 3 2 Cost function versus individual parameters, with remaining parameters fixed at true values

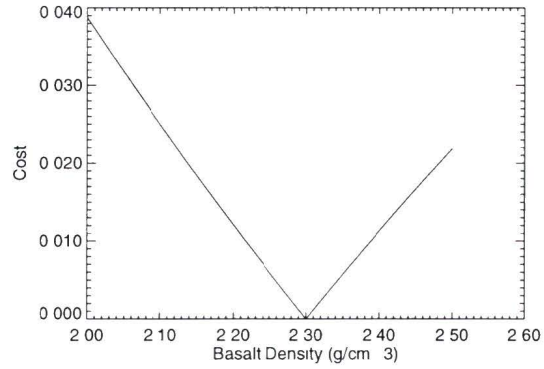

c) Basalt Density

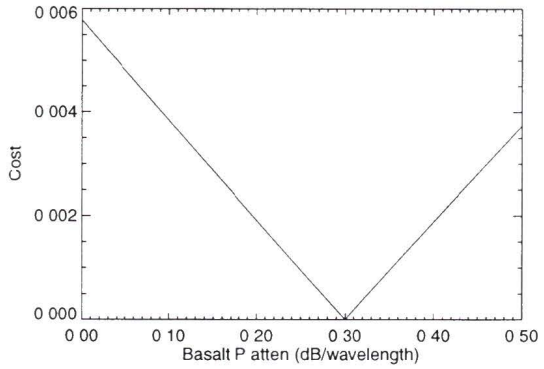

d) Basalt Compressional Attenuation

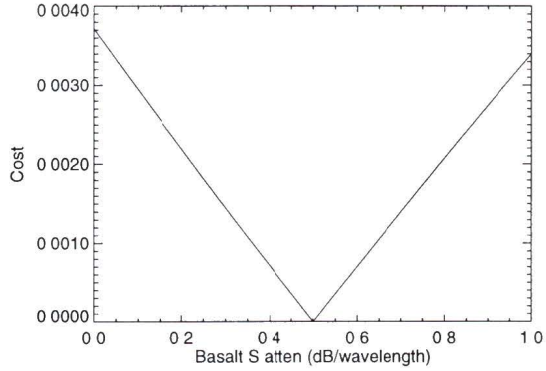

e) Basalt Shear Attenuation

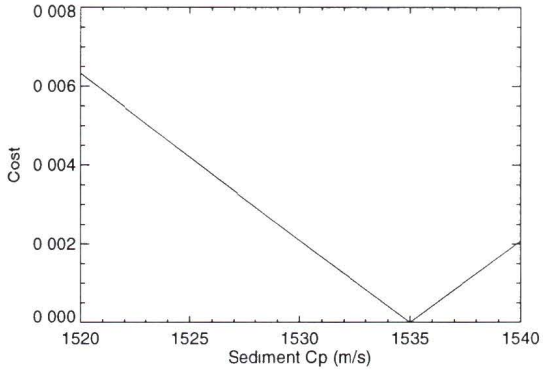

f) Sediment Compressional Speed

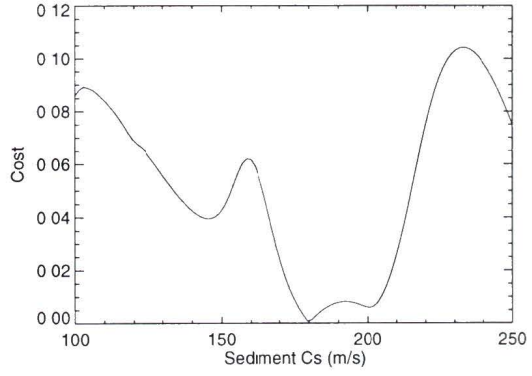

g) Sediment Shear Speed

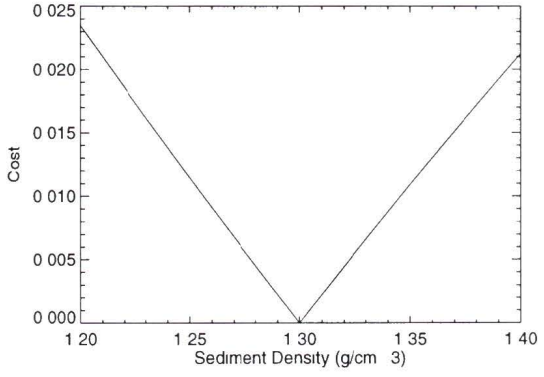

h) Sediment Density

Figure 3 2 Continued

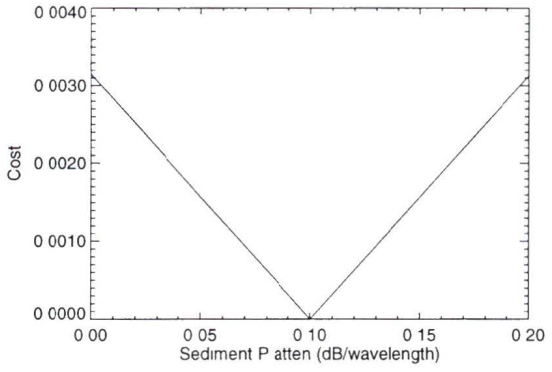

i) Sediment Compressional Attenuation

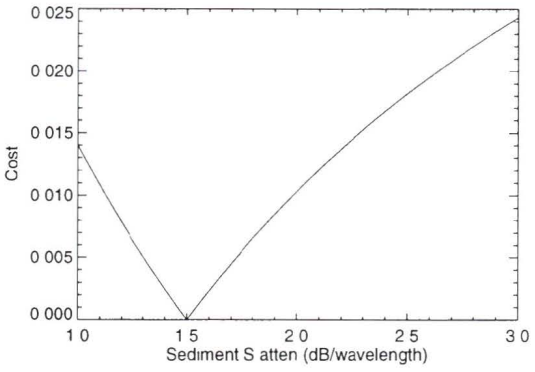

j) Sediment Shear Attenuation

Figure 3 2 Continued

The projections in figure 3 2, for all parameters except sediment shear wave speed (figure 3 2 g), are "V" shaped with only a single minimum corresponding to the global minimum Note the cost function scale is different in each plot The sediment shear speed projection has multiple minima over the allowed sediment shear wave speed range The existence of these local minima emphasizes the requirement that gradient methods be avoided for searching for the global minimum The projections in figures 3 2 only represent the cost function characteristics function close to the global minimum It is likely that additional local minima exist in regions of the cost function defined by all parameters displaced significantly from their true values If a calculus based search method was employed, it could converge to one of the local minima present in figure 3 2 g at sediment shear speeds of 100 m/s, 140 m/s, 200 m/s or 250 m/s For this reason the non-linear minimization algorithm Simulated Annealing, which has the ability to escape local minima, is used in the inversion method

C. Cost Function Variance

An estimate of the relative sensitivity of the cost function to the individual parameters near the global minimum is obtained from the variances of the cost function projections over the respective parameter ranges If the variance is small, then the parameter which was varied caused little change in the cost function value This sensitivity estimate may not, however, be representative of the sensitivity in regions of the search space far from the global minimum We require a sensitivity estimate which is representative of the nominal sensitivity over the entire search space A better estimate of

the sensitivity is obtained by calculating the variance of the cost function projections due to varying each parameter, at many fixed configurations of the other parameters These variances are then averaged to give a measurement more representative of the general sensitivity over the search space Table 3 3 lists sensitivity estimates for the individual parameters obtained this way, where the variances from 200 separate random configurations of the other parameters were averaged

Layer	C_p	C_s	α_p	α_s	ρ
Sediment	1 4	770	2 1	48	26
Basalt	660	1400	5 9	2 5	35

Table 3 3 Average variance of cost function ($\times 10^6$) when parameter is advanced through its range

It is apparent from table 3 3, that the averaged variance estimates for parameter sensitivity are in agreement with the conclusions for the relative importance of each of the parameters obtained from analyses of the equivalent reflection coefficient curves We see that the sensitivities of the three most important parameters basalt compressional and shear wave speeds and sediment shear wave speed, are more than an order of magnitude greater than all other parameters In fact, they are more than 2 orders of magnitude more sensitive than the four least sensitive parameters Because of the very low sensitivity of sediment compressional speed, sediment compressional attenuation, basalt compressional attenuation and basalt shear attenuation, it is unlikely that the inversion method can provide reliable estimates for these parameters from real loss data containing even very low level of scatter On the other hand, the removal of these less sensitive parameters from the inversion should not introduce significant error into the estimates for the more sensitive parameters

IV. Inversion trials

A. Noise-free Inversion

The inversion method was run using the simulated reflection loss data generated for the geoacoustic profile in table 3 1 Sediment compressional wave speed and compressional attenuation as well as basalt compressional and shear wave attenuations were omitted from the inversion due to their extremely low sensitivities The omitted

parameters were fixed at the lower limits of their respective ranges to determine the maximum error introduced into the other parameter estimates by the omissions The parameter ranges from table 3 2 were used as the search ranges for the parameters included in the inversion During the inversion, 21,000 separate models were tested, using the simulated annealing minimization algorithm, to find the optimum parameter set The method converged to an estimated profile which is described by the estimated values shown in table 3 4

Table 3 4 True parameters and noise-free inversion estimates

Layer	Parameter	TrueValue	Search Range	Estimate
Sediment	C_s	180 0 m/s	100 200 m/s	180 3 m/s
	α_s	1 50 dB/λ	1 0 - 3 0 dB/λ	1 51 dB/λ
	ρ	1 30 g/cm^3	1 2 - 1 4 g/cm^3	1 32 g/cm^3
Basalt	C_p	2800 m/s	2600 - 3000 m/s	2799 5 m/s
	C_s	1100 m/s	900 - 1400 m/s	1101 1 m/s
	ρ	2 30 g/cm^3	2 0 - 2 5 g/cm^3	2 30 g/cm^3

The inversion was remarkably successful at reproducing the geoacoustic profile for the noise free case The only parameter from table 3 4 which was in error by more than 0 5% of its search range was the sediment density This estimate was in error by 10% of its range It is observed that the sensitivity of the cost function to sediment density is the lowest of all other parameters included in the inversion It is it noted that an exhaustive search, where the search space for 5 parameters was discretized, would require the testing of approximately 10^{10} models to obtain an accuracy of less than 0 5% for the estimate of each parameter The simulated annealing algorithm therefore was more efficient by a factor of 10^6 for this noise free inversion

B. Inversion of Noisy Data

To test the effect of experimental errors, random error (noise) was added to the simulated reflection loss data used for the inversion from part A The noise was introduced by adding a random error, generated by a random number generator, to each point on the reflection loss versus grazing angle curve Three separate inversions were performed at maximum error magnitudes of 0 1, 0 15, and 0 2 respectively The noise free curve, and noise added curve for the 0 2 noise level are shown together in figure 3 3

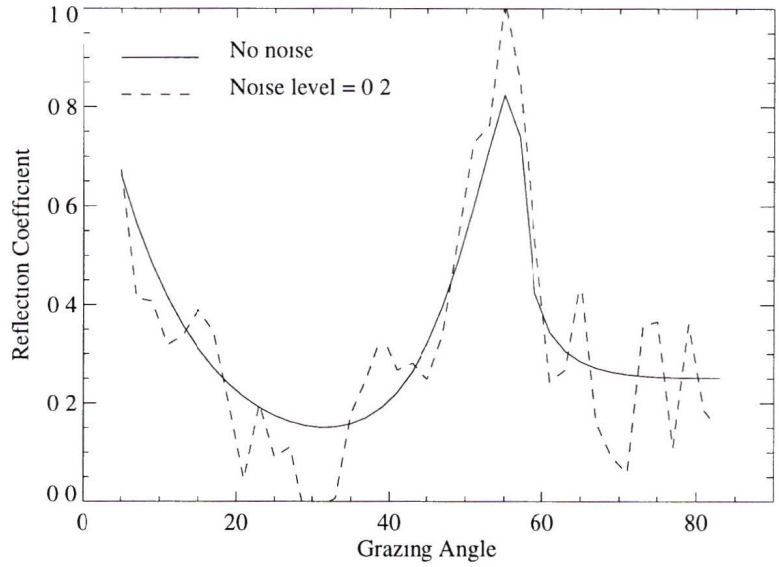

Figure 3 3 Noise free, and 0 2 noise level reflection loss curves

The search ranges for the geoacoustic parameters were the same as the ranges used for the noise free inversion The inversions for the noise-added data were performed similarly to the noise-free case Parameter estimates obtained from all three inversions are included in table 3 5

Table 3 5 True parameters and inversion estimates at maximum noise levels of 0 1, 0 15, and 0 2

			Inversion Estimates		
Layer	Parameter	Model	N=0 1	N=0 15	N=0 2
Sediment	C_S (m/s)	180 0	176 5	176 5	175 2
	α_S (dB/λ)	1 50	1 70	1 63	1 71
	ρ (g/cm^3)	1 30	1 22	1 20	1 20
Basalt	C_D (m/s)	2800	2804 6	2768 2	2787 6
	C_S (m/s)	1100	1059 5	1075 0	1056 8
	ρ (g/cm^3)	2 30	2 40	2 40	2 40

Inversion estimates for the less sensitive parameters sediment shear wave attenuation, sediment density and basement density, were corrupted by the presence of even the lowest noise level tested The accuracies of the estimates for the three most sensitive parameters, sediment shear wave speed and the basalt compressional and shear wave speeds, were reduced, but were satisfactory at all noise levels As a percentage of the search range, the estimates for the sediment shear speed at the three noise levels

differed from the experimental value by only 3 5%, 3 5% and 4 8% The estimates for the basement compressional wave speed differed from the experimental value by 1 2%, 8 0% and 3 1%, and estimates for the basement shear wave speed differed from the experimental value by 11 9 %, 5 0% and 8 6%

V. Summary

The cost function representing the rms match between simulated reflection coefficient versus grazing angle measurements and modeled reflection coefficients was found to be most sensitive to sediment shear wave speed, basalt compressional wave speed and basalt shear wave speed for the geoacoustic profile used The ability of the method to estimate the parameters in the presence of noise was found to be correlated with the sensitivities of the cost function to the respective parameters Only the estimates for the three most sensitive parameters listed above were found to be reliable in the presence of noise of amplitude similar to that which is present in actual reflection loss versus grazing angle data The sound speeds in the basalt are, however, the parameters of greatest interest to geoacoustical modelers for thin-sediment bottom environments The inversion method therefore should be a valuable tool for remote measurement of these values over large regions of the ocean bottom

Chapter 4
Experimental study

The inversion method described and tested in chapters 1 to 3, is applied here to a set of data collected at nine thin sediment sites in the North Pacific These sites are located along an East-West track at 34°N latitude between 131°W and 143°W longitude The track is shown on the map in figure 4 1

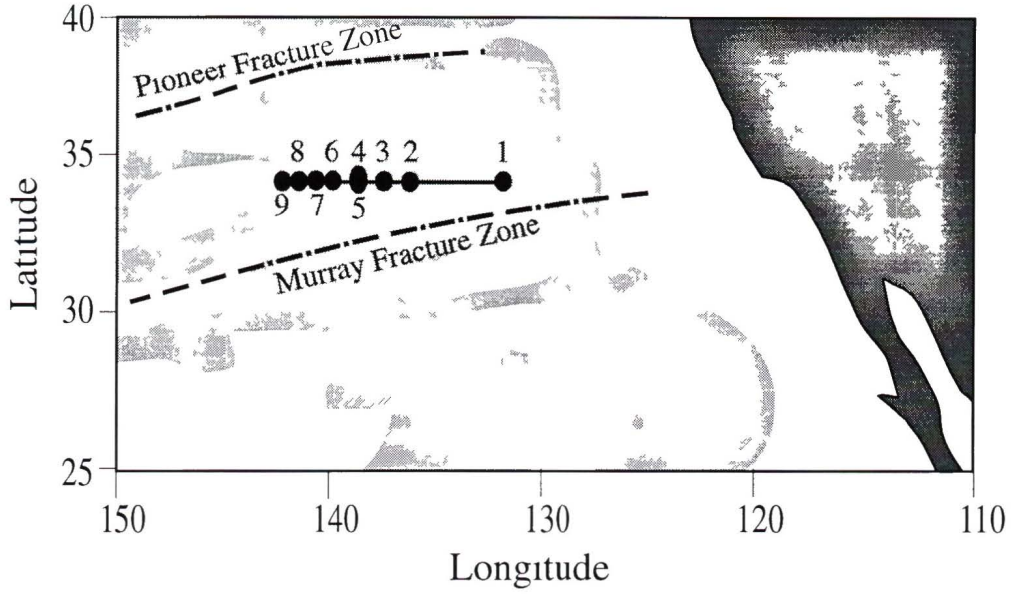

Figure 4 1 Locations of the 9 experiment sites along the experimental track in the North Pacific The shaded region shows where sediment thickness is less than 100 m

I. Geoacoustic Environment

The experimental track lies between the Murray and Pioneer fracture zones off the West coast of Southern California, and is approximately perpendicular to the axis of a spreading centre, which is no longer active The spreading rate had been approximately 4 cm/yr and the age of the basalt along the track increases from approximately 40 m y at the East end to approximately 63 m y at the West end (Atwater and Severinghaus, 1989) The entire track lies within the area categorized as the Abyssal Hills region (Hamilton, 1980), and sediment thickness is less than 33 m The location, bottom depth, sediment thickness, and crustal age for each site are included in table 4 1

Table 4 1 Environmental information at each shot run experiment site

Shot Run	Longitude Range	Bottom Depth (m)	Sediment Thickness (m)	Crustal Age (m y)
1	131°47 to 132°03'	5100	33	42
2	136°03' to 136°19'	5010	23	49
3	137°35 to 137°48'	5050	22	50
4	138°15 to 138°32'	5080	15	52
5	138°18' to 138°18'	5080	24	52
6	139°53' to 140°10'	5145	25	56
7	140°54' to 141°10	5030	25	59
8	142°20 to 142°34'	5300	28	61
9	143°12 to 143°25'	5540	15	63

The predominant geological feature of the bottom at the experimental sites is the abyssal hills These elongated hills have nominal dimensions of 1-2 km in width, by 10-20 km in length by 100-200 m high The hills are aligned approximately parallel to the axis of the spreading centre Small scale roughness was estimated by a 3 5 kHz profiler to be on the order of 10 m over the entire track Water depth was approximately 5000 m over most of the track, increasing to approximately 5500 m at the West end

II. Experiment

Experiments consisting of shot runs for measuring bottom reflection loss were performed at each site The shot runs were carried out using two ships, the C F A V Endeavour and the U S N S DeSteiguer The Endeavour towed the Canadian Oceanographic Acoustical Measurement System (COAMS) horizontal line array which collected all of the acoustic data During each of the runs, the Endeavour towed the array, at depths between 200 to 250 m, close to due West along the 34 0°N latitude at speeds of 3 to 4 knots At the start of each run, the DeSteiguer was positioned on the North side of the array at a range of 1 5 km The DeSteiguer then turned to a heading of approximately 335°T so that it departed from the array at a relative angle of 65° referred to the E/W track As the range from the array increased, a series of 40 - 0 82 kg Signal Underwater Sound (SUS) charges was deployed from the DeSteiguer The charges were set to detonate at a nominal depth of 244 m During each run, the DeSteiguer maintained a speed of approximately 6 knots so that the relative bearing from the array remained fairly constant at approximately 15° rear of broadside This ensured that the acoustic paths were approximately parallel to the axes of the abyssal hills throughout each run Additionally, one or two charges were dropped from the Endeavour at the start of each run to aid in array localization, and to provide near-vertical incidence data Each shot run

spanned a small range of about 15 km along the experimental track Figure 4 2 contains a diagram of the relative ship and array geometry

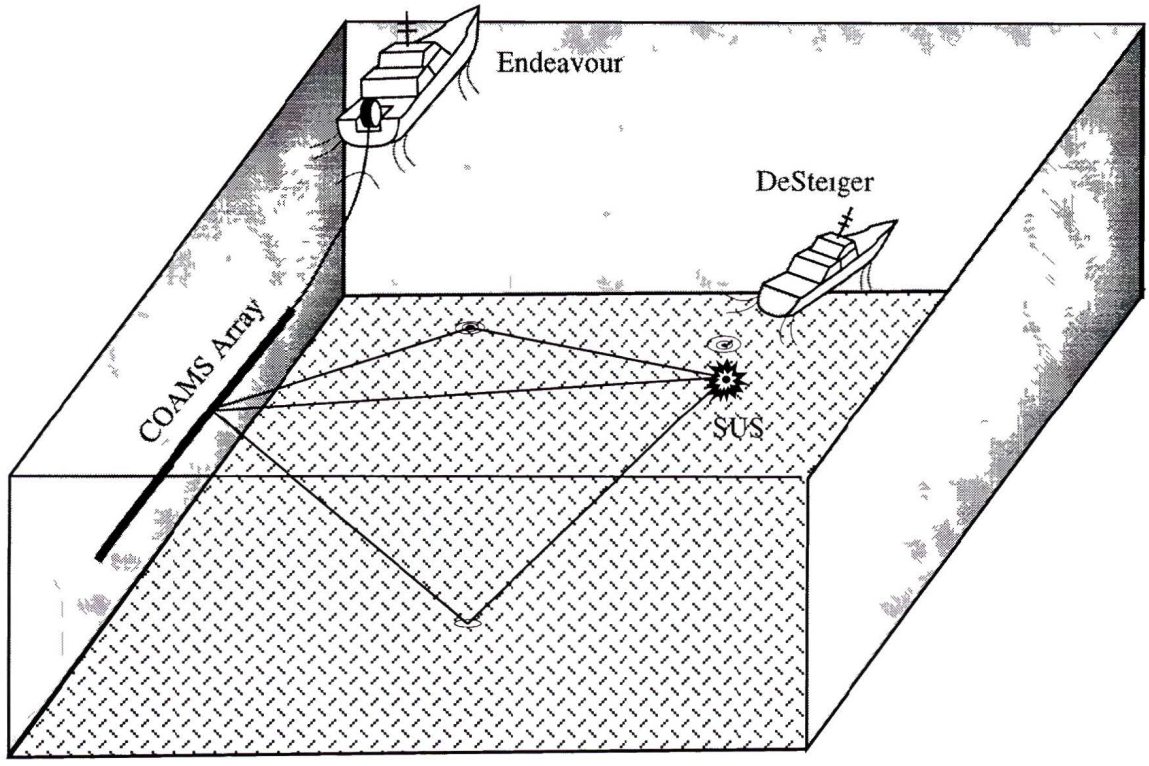

Figure 4 2 Relative experimental positions of the ships, the SUS charge and the array

The source drop schedule was designed to provide bottom grazing angles between 10° and 80° in steps of approximately 2° for single acoustic bottom reflections The source to array range for the last shot in each run was between 30 km and 40 km

The COAMS array consisted of 126 hydrophones, spaced to form 4 specific apertures In this work, only the very low frequency aperture, consisting of 38 hydrophones equi-spaced at 38 1 m, was used The higher frequency aperture data were also analyzed, however, those data will only be discussed briefly in regard to the measurement of scattering from the rough bottom Each hydrophone was actually a composite hydrophone group, consisting of 10 smaller elements wired in parallel The composite hydrophone was essentially omnidirectional for frequencies less than approximately 100 Hz, and sensitivity was -191 dB re μPa Hydrophone outputs were preamplified to drive the signal back to the ship The preamplifier had a nominal gain of 26 dB, but started to roll off below 17 Hz The average preamplifier gain was 24 4 dB in the 1/3 octave band centred at 8 Hz On-board ship, the analogue signals were again

amplified by a programmable gain amplifier which could be set between 0 and 96 dB in steps of 6 dB After the secondary amplifier, the signals were passed through a signal conditioning unit which included an antialiasing filter with a roll off starting at approximately 200 Hz The output of this secondary amplifier was digitized by a 12-bit A/D converter at a rate of 699 05 samples per second for each hydrophone A full scale analogue input of -10V to +10V resulted in digital outputs ranging from -2048 to +2047 The digital data were stored directly on magnetic tapes

Additionally, several data pertaining to the experiments were measured during the shot runs At least one XSV (Expendable Sound Velocity probe) was deployed to measure the sound speed profile at each of the shot run locations The XSV's measured the profile to a depth of 2500 m Below 2500 m, the variation in the profile is small over the experimental track, and the profile for these depths was obtained from a catalogued profile for the region Furthermore, some array status information was recorded during each of the runs This consisted of 6 depth readings and 3 heading readings from sensors located on the array The range of the DeSteiguer from the Endeavour was monitored during each of the runs using RADAR and a radio trisponder system The ship positions were also recorded at regular intervals using LORAN

III. Array Data Processing

A Signal Characteristics

The significant arrivals near each shot time were first windowed out of the continuous digital data recordings A typical shot waveform, measured on one of the array hydrophones, is shown in figure 4 3 for a shot approximately 20 km from the array The direct path signal occurs at approximately 5 5 s in figure 4 3 and has very small amplitude in comparison to the later bottom reflected paths This is due to the destructive interference with the surface reflected path which is 180° out of phase with the direct path at all frequencies, and arrives nearly simultaneously

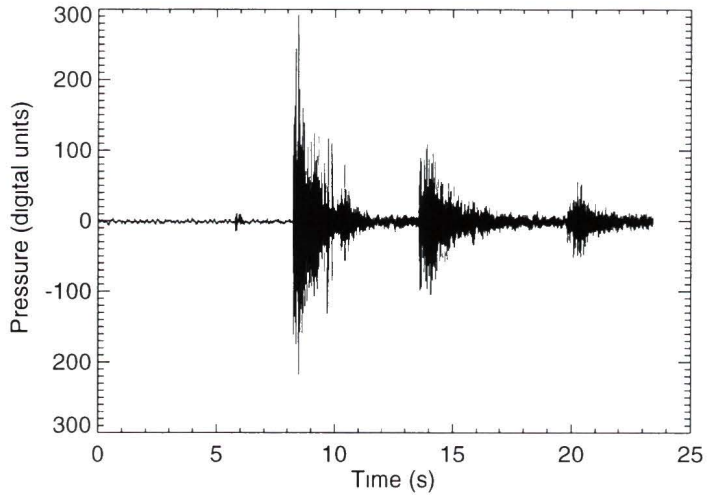

Figure 4 3 Typical shot waveform measured on a single hydrophone

Arrivals for the single, double and triple order bottom reflections can easily be seen in the waveform at approximate times 8 s, 13 5 s, and 19 5 s We note also from figure 4 3, that much of the signal in the bottom reflected paths is due to scattered rather than specularly reflected energy This is known because the specular reflected waveform duration should be less than 0 6 s (the lastest arrival will be the doubly converted shear path whose interbed multiples are highly attenuated), and the four-path impulse response for the single order specular reflection geometry is approximately 0 7 s The total length of the purely specularly reflected signal should therefore be less than 1 3 s, whereas the figure shows significant arrivals lasting for more than 3 s In order to remove this scattered energy, beamforming of the array data was performed as was suggested in Chapter 2 section V

B Beamforming

Plane wave time domain beamforming involves applying time delays to the outputs from the sensors on an array and then adding the resulting (possibly weighted) waveforms The time delay to be applied between any two sensors is related to the time it takes for a wave front of a plane wave, incident on the array, to pass from one sensor to the other The delay is applied so that the signals are added in-phase for a particular angle of incidence An expression for the time delay required between any 2 adjacent sensors is derived by referring to the diagram in figure 4 4, which shows two of the wavefronts from a plane wave signal, incident onto the array at angle θ

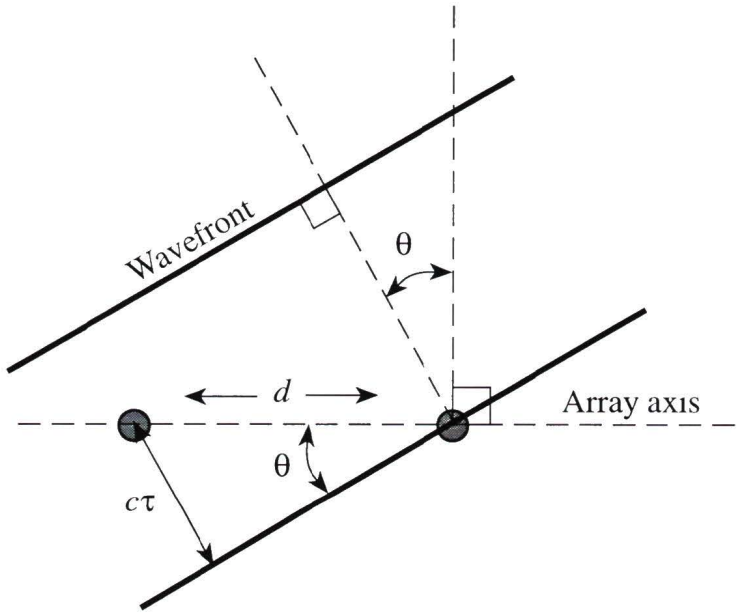

Figure 4 4 Plane waves incident on two sensors

In the time τ it takes for the wave to pass from one sensor the next, the wavefront advances a distance $c\tau$ perpendicular to itself, where c is the propagation speed of the acoustic wave It is noticed, by referring to figure 4 4, that $c\tau$ is related to d and θ by $c\tau = d \sin(\theta)$ Thus for beamforming in a direction at angle θ measured from the array broadside, the time delay to be applied to the second sensor is $\tau = d \sin(\theta)/c$ with respect to the first sensor Beamforming in a particular direction is commonly referred to as *steering* the array When beamforming with more than two sensors which are all spaced a distance d apart, the time delay between any pair of adjacent sensors is τ The beamformed signal for an array containing N hydrophones steered to angle θ is thus

$$b(t,\theta) = \sum_{i=1}^{N} a_i p_i(t-(i-1)\tau) \qquad (4\ 1)$$

where $p_i(t)$ is the pressure signal measured on the ith hydrophone, and a_i is a weighting factor applied to the ith hydrophone to improve the directivity function characteristics The directivity function for a line array describes the amplitude response for single frequency plane harmonic waves incident upon the array, versus the angle of incidence measured from the array broadside It can easily be shown that the directivity function is the Fourier transform of the array aperture function $G(u)=\Im[g(x)]$, e g (Burdic, 1991), where $u=\sin(\theta)/\lambda$ and λ is the wavelength of the incident wave The aperture function

$g(x)$ defines the spatial amplitude response of the array If the array is continuous (as opposed to having discrete sensors) and has a finite length L over which the response is uniform, the aperture function is a boxcar function extending from $-L/2$ to $+L/2$ In this case, the directivity function is a sinc function in the variable (uL)

When the array is discrete with N sensors equally spaced d apart, and the broadside beam is formed using equation 4 1 with all $a_i=1/N$, the directivity function is a repeated sinc function in the u domain The explicit form of the directivity function for this case is given by Burdic

$$G(u)=\frac{1}{N}\frac{\sin(\pi N d u)}{\sin \pi d u} \tag{4 2}$$

The square of the directivity function $G^2(u)$ is called the pattern function The pattern function describes the angular power response of the array to single frequency sinusoidal signals The main lobe in the pattern function occurs at $u = 0$ This occurs for $\theta = 0°$ (broadside) as expected The zero crossings at the edges of this lobe occur at $u = \pm 1 / L$ The points on the main lobe at which the pattern function has decreased 3 dB from its maximum occur approximately at $\theta_{3dB} = 25 \lambda / L$ deg Additional lobes called side lobes occur on the periodic maxima and minima of the sinc function in the numerator of the above expression for $G(u)$ The first side lobe occurs approximately at $u = 3 / (2 L)$ and is only 13 dB lower than the main lobe Also, since $G(u)$ contains repeated sinc functions, some of the side lobes and possibly the main lobes from the adjacent sinc functions will occur in the range $u=0$ to $\pm 1/\lambda$, ($\theta=0$ to $\pm 90°$) When the main lobes of the adjacent sinc functions fall in this range they are called grating lobes Grating lobes will occur at $u = \pm 1/\lambda$, ($\theta = \pm 90°$) when the sensor spacing $d = \lambda$ They will not occur if d is less than λ The effect of side lobes from the adjacent sinc functions is minimized when $d=\lambda/2$ In order to reduce the height of the side lobes, a technique analogous to windowing of the time series in time-frequency domain processing is applied Instead of using the same weight factors in equation 4 1 for all hydrophones (i e a discrete boxcar function), a smoother function is used The function is applied by reducing the relative weights for hydrophones near the ends of the array The term *array shading* is used to describe this process Reduction of the side lobe heights is obtained at the expense of a slightly wider main lobe For example, -35 dB side lobe levels can be achieved using Taylor shading coefficients (Taylor, 1956), with a resulting increase in the main lobe width of about 25% in the u domain

When steering the beam away from broadside using non-zero time delays, the angular widths of the lobes increase In the u domain however the widths remain constant and only a lateral shift of the function $G(u)$ results If the first beam off broadside is achieved with a delay of τ seconds between adjacent hydrophones, then $G(u)$ will be shifted by $\tau\ c\ /\ (\ N\ d\ \lambda\ )$ along the u axis Therefore, if the time delays used to form different beams are multiples of τ, then those beams will be equally spaced in the u domain Beams created this way have the desirable characteristic that their cross-over points with adjacent beams are all at the same level They however have the undesirable characteristic that they are not evenly spaced in the angular (θ) domain

A software time delay beamformer was written to beamform the acoustic array data For the VLF aperture, 37 beams were formed including 18 forward, 1 broadside, and 18 aft The full unshaded 3 dB beamwidth at broadside for a sine wave at 8 Hz for the beamformer was 6 6°, and the first side lobe occurred at 11 1° Taylor shading was applied so that side lobe levels of -35 dB were obtained to reject the significant scattering noise observed at the experimental sites which could have entered through the side lobes The Taylor aperture function used is plotted in figure 4 5 After the delay-add beamforming algorithm was applied, the beams were normalized to the equivalent amplitude of a single hydrophone by dividing the beam amplitudes by the sum of the shading coefficients Beam centre angles and upper and lower 3 dB angles for each shaded beam are given in table 4 2 The shaded beams are slightly wider than those for uniformly weighted apertures

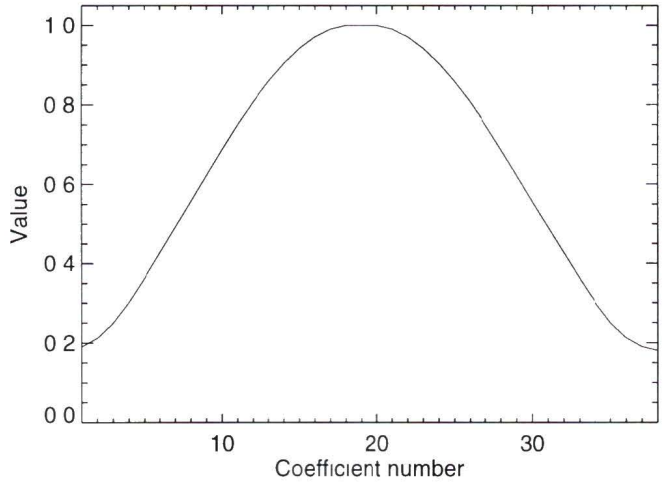

Figure 4 5 Taylor shading coefficients used for -35 dB side-lobes

Table 4 2 Beamformer angle ınformatıon

Beam	Beam Center	8 Hz Beam Low	3 dB edges High
0	0°	-4 3°	+4 3°
±1	±3 22°	-1 1°	±7 5°
±2	±6 46°	±2 2°	±10 8°
±3	±9 71°	±5 4°	±14 1°
±4	±13 00°	±8 6°	±17 4°
±5	±16 33°	±11 9°	±20 9°
±6	±19 72°	±15 2°	±24 3°
±7	±23 19°	±18 6°	±27 9°
±8	±26 74°	±22 0°	±31 7°
±9	±30 41°	±25 6°	±35 5°
±10	±34 22°	±29 2°	±39 6°
±11	±38 22°	±32 9°	±43 9°
±12	±42 44°	±36 9°	±48 6°
±13	±46 98°	±41 0°	±53 7°
±14	±51 94°	±45 4°	±59 6°
±15	±57 52°	±50 2°	±66 7°
±16	±64 15°	±55 6°	±77 1°
±17	±72 97°	±61 8°	±90 0°

The beams are conıcal around the array axıs Each beam admıts energy from a small range of angles close to the angle descrıbıng the cone The bottom reflected energy admıtted by a beam ıs therefore lımıted to that whıch has ınteracted wıth an area defıned by the ıntersectıon of the respectıve beam wıth the bottom The ıntersectıons of the conıcal beams from the horızontal array wıth a horızontal planar bottom are hyperbolas Fıgure 4 6 shows the centre lınes for the hyperbolıc ıntersectıons of the beamformer beams wıth the bottom, assumıng that the array depth ıs 200 m and the water depth ıs 5200 m Only the bottom ıntersectıons for the beams aft of broadsıde (negatıve beams), and only on one sıde of the array are shown The ıntersectıons for the beams forward of broadsıde and on the other sıde of the array are mırror ımages of those shown It ıs also apparent from fıgure 4 6 that the hıghest angular resolutıon occurs near broadsıde The experıments were desıgned so that the shot detonatıon posıtıons were approxımately 10-15° rear of broadsıde Consequently the reflected sıgnals arrıve from angles where the beam-wıdths are relatıvely narrow and beam resolutıon ıs quıte good

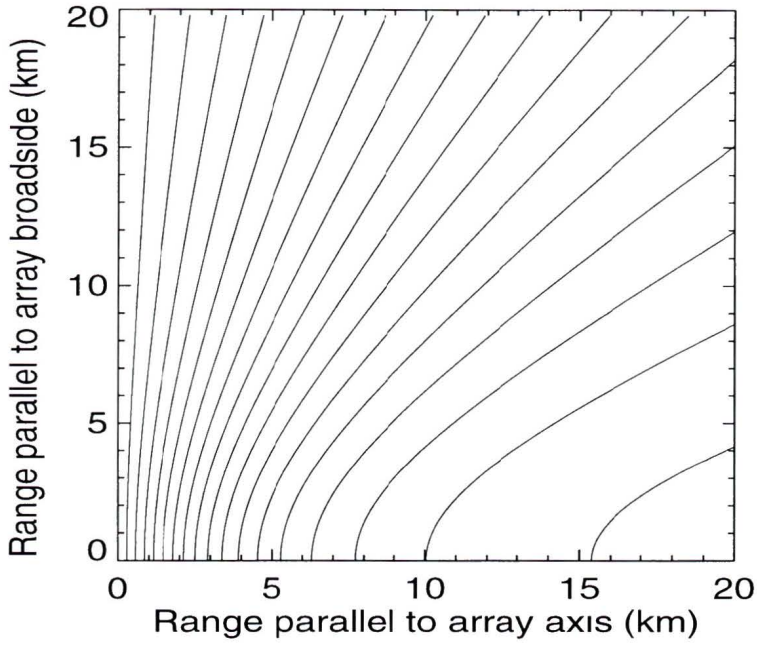

Figure 4 6 Intersection of beams on 5 2 km - deep bottom

Typical beamformer outputs for a shot at 5 km range, in 1/3 octave bands at 8 Hz and 125 Hz, are shown in figures 4 7 (a and b) Corresponding beamformer output for a shot at 30 km range is shown in figures 4 7 (c and d) The 125 Hz beamformed data were generated from the HF aperture which was comprised of 64 hydrophones, equi-spaced at 4 9 m The basic time delays used for the 125 Hz data were set so that the same beam centre angles were obtained as for the 8 Hz VLF aperture data However, the beam-widths are slightly narrower because L/λ is greater for the HF aperture than for the VLF aperture

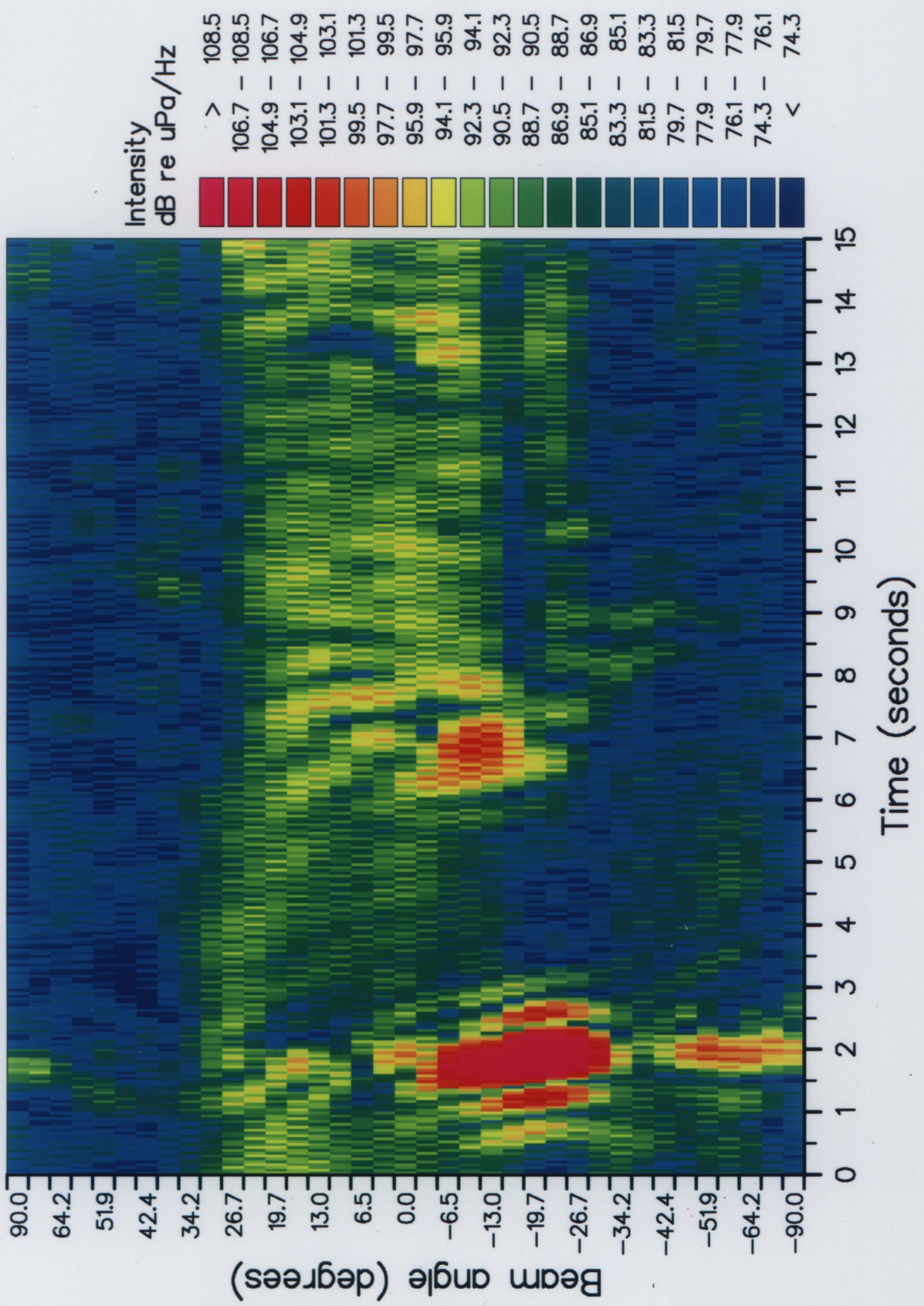

Figure 4.7 a: 8 Hz beamformer pattern for shot at 5 km range

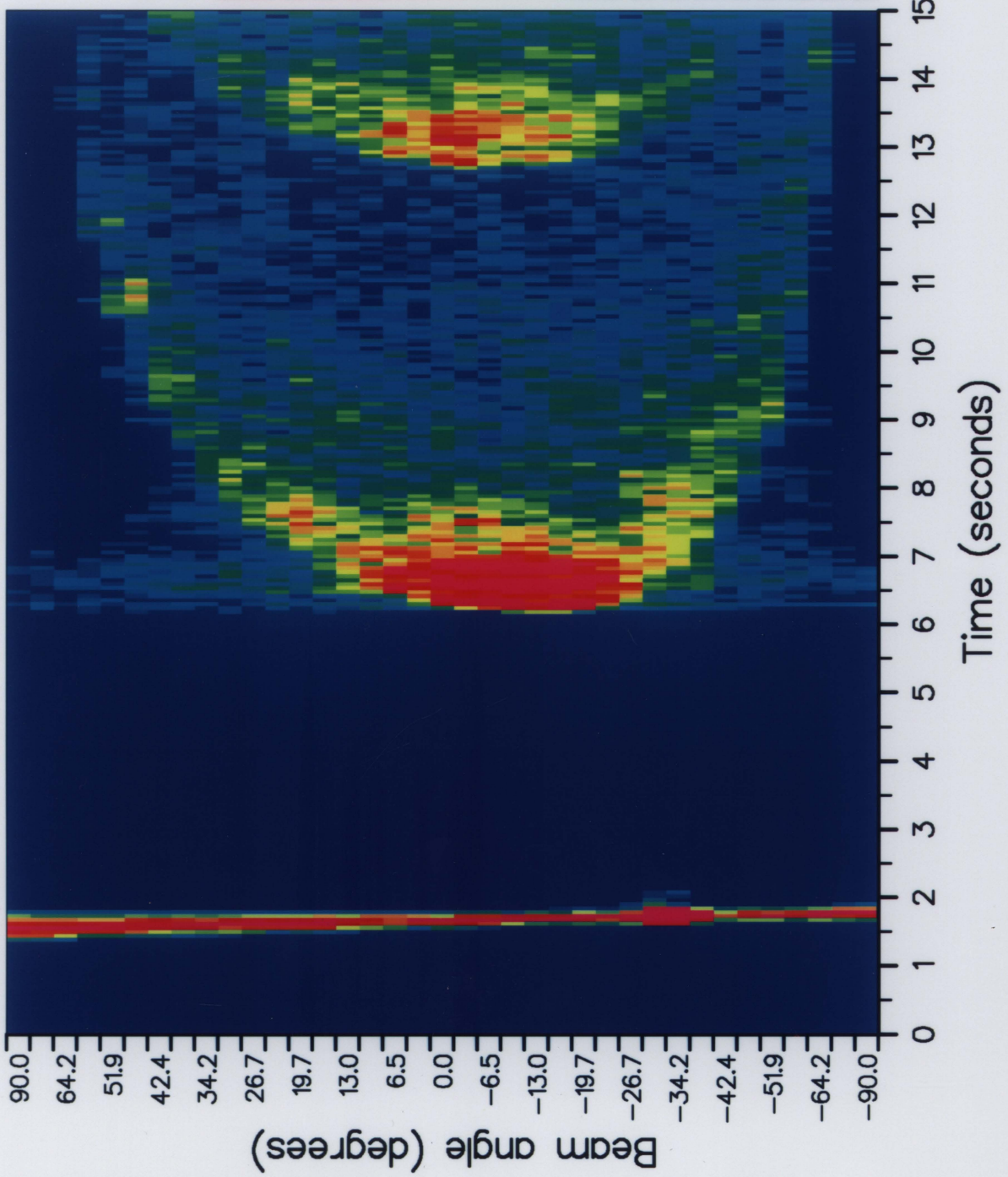

Figure 4.7 b: 125 Hz beamformer pattern for shot at 5 km range

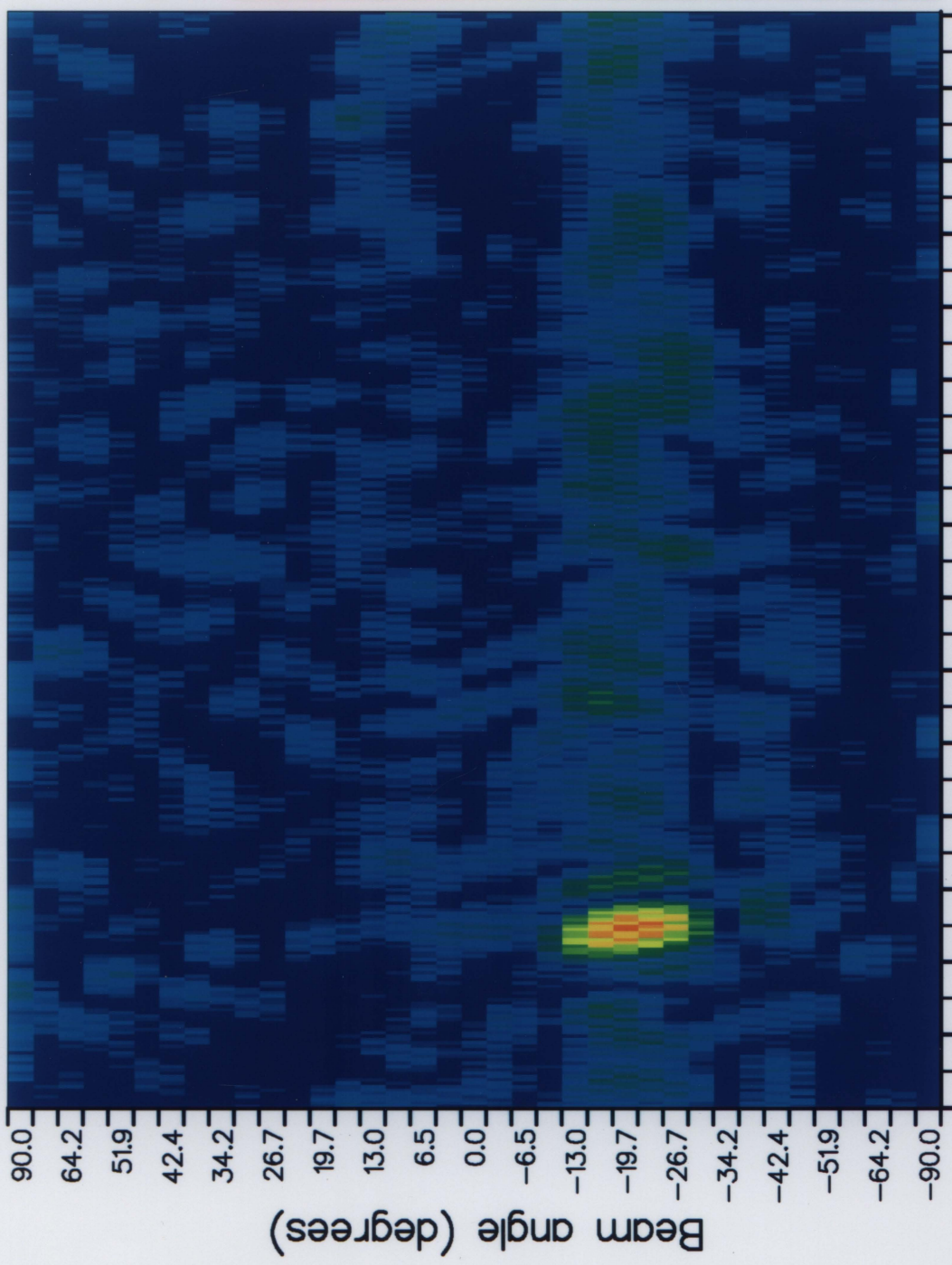

Figure 4.7 c: 8 Hz beamformer pattern for shot at 30 km range

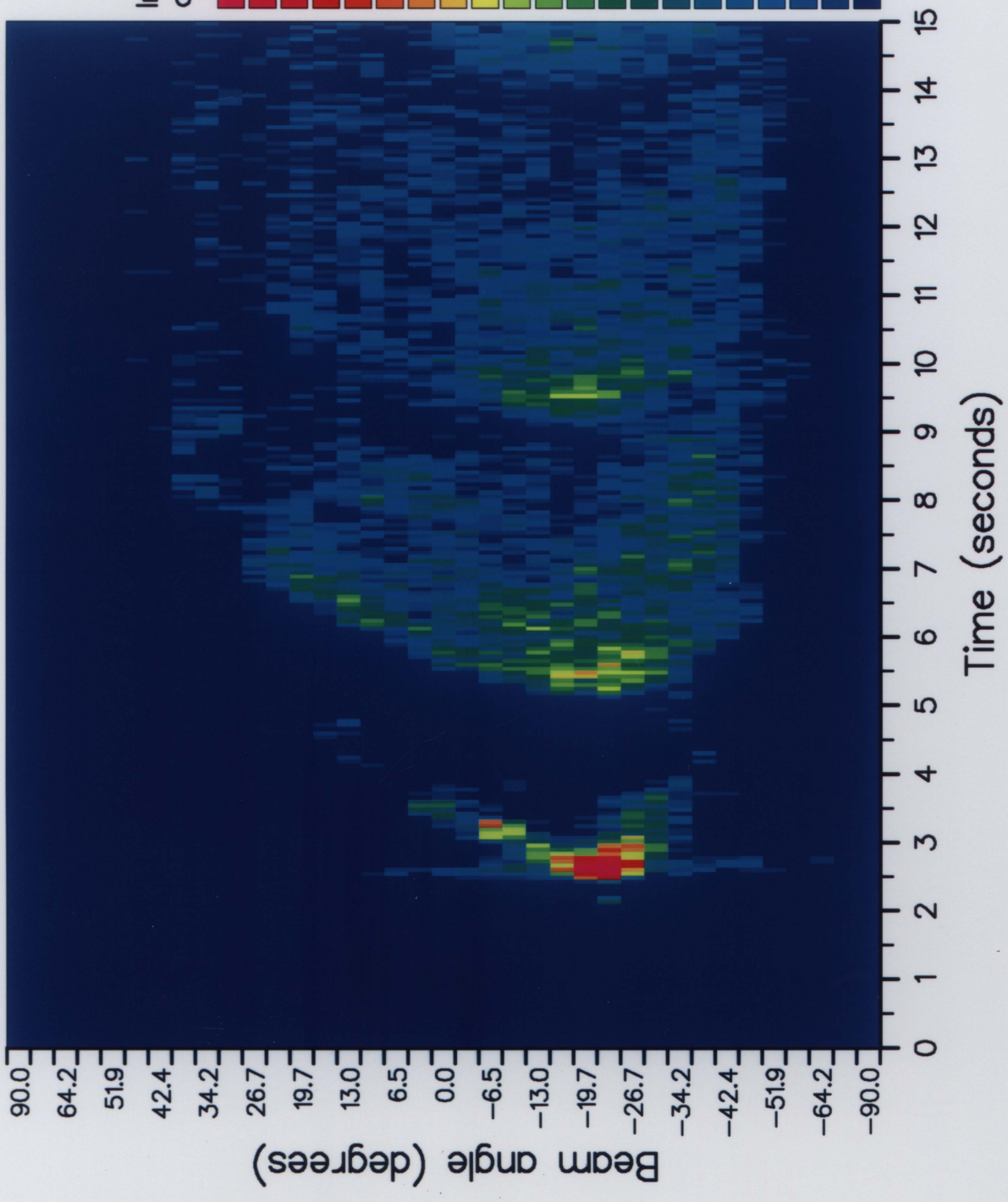

Figure 4.7 d: 125 Hz beamformer pattern for shot at 30 km range

The single order bottom reflection for the 5 km shot occurs approximately at time $t = 6.5$ s in figures 4.7 (a and b). We note the strong direct path arrival occurring at 1.5 s and the second order bottom reflection arrival at 13 s in these figures. The direct path arrives further aft of broadside in the 125 Hz beams than the 8 Hz beams, because the centre of the HF aperture was approximately 500 m forward of the centre of the VLF aperture. The specular single bottom reflection arrivals occur in the beams at -9.7° and -13.0° respectively at 8 Hz and 125 Hz. We see that there are several beams, centred approximately around the specular reflection beam, which admit significant energy. The energy arriving from angles other than the specular angle is due to non-specular scattering at the rough bottom. Because this scattered energy has to travel a greater distance in the water, it always arrives at a later time than the specularly reflected signal. This delay is very obvious for the non-specular reflected signals in the 125 Hz beams of figure 4.7 b. In fact, scattered energy is observed arriving up to 6 s after the specular arrival. It is noticed also that the angular spread of the energy at 125 Hz is much larger than at 8 Hz. Single order bottom interacting energy can be detected in the beam at +64.2° in the 125 Hz data. This is approximately 70° away from the direction of arrival of the specular reflection. The maximum angular difference from the specular direction for the 8 Hz data is only approximately 20°. The observation that greater angular spread occurs at 125 Hz than at 8 Hz indicates scattering is stronger for the high frequency signals. This is consistent with scattering theory according to the Eckart model (Diachok *et al*, 1994).

Examination of the beamformed data for the shot at 30 km range (figures 4.7 c and d), shows that the angular characteristics of the bottom reflected signals differ from those at 5 km range. At 30 km range, the direct path arrival and its surface reflection cancel each other out as was discussed for the shot waveform of figure 4.3 in part A. We can, however, see the remnant of the direct path in the 125 Hz data (figure 4.7 d), occurring at approximately 2.25 s, 0.25 s before the single bottom reflection. We can also see the two, three, and four bottom reflection paths occuring respectively at approximately 5 s, 9.5 s, and 14.5 s in figure 4.7 d. We note first, that the angular spread of the single bottom reflection, for the shot at 30 km, is much less than for the shot at 5 km. An interesting feature of the arrivals in figure 4.7 d is that the two bottom reflection path has significantly greater angular spread than the single bottom reflection path. These angular spread characteristics are consistent with scattering theory, which predicts stronger scattering for higher grazing angles. The grazing angle decreases with range,

thus explaining the narrower angular spread for the long range shot Additionally, the two bottom reflection path propagates more steeply than the one bottom reflection path and thus has a higher grazing angle associated with it This would account for the greater angular spread observed for this path in figure 4 7 d

IV. Reflection Loss Measurement

The Reflection loss (H_B) calculation was performed according to equation 2 5

$$H_B = SL - H_S - L + 6\ 02$$

where SL is the source level, H_S is the propagation loss, and L is the measured energy level for the specular reflection at the array Source levels for the depth of each shot were obtained from depth-scaled spectra of 0 82 kg SUS charges detonated in a controlled experiment Appendix A contains detailed descriptions of the depth-scaling method and the controlled experiment Measured energy was obtained using the procedure described in section IV part A, and propagation losses (H_S) were calculated as described in section IV part B The calculated reflection losses were tabulated together with corresponding bottom grazing angles

A. Energy Measurement

The first step for obtaining reflection loss measurements involved measuring the energy level of the specularly reflected arrival at the array Due to the consistent experimental geometry, it was known that the specularly reflected signal arrived in a beam close to -10° As a result, analysis of beam data was limited to the beams spanning the angular region from -3 2° to -19 7° Each of these beams contained a pressure time series normalized to the amplitude of a single sensor, and filtered in the 1/3 octave band at 8 Hz The time series of the beams were first previewed to determine the start point for the acoustic arrivals of the bottom reflection A time window of 1000 data points (1 431 s), beginning at the start point in the arrival, was chosen for each beam All energy measurements were made from these time windowed sections of the beamformed time series

It was required that the energy level measurements be obtained in units of dB *re* erg/cm^2 normalized to a 1 Hz band to agree with the conventional units for the SUS

charge source levels This unit represents energy per area and is referred to as energy flux density The total energy flux density is the time integral of intensity This represents the total acoustic energy propagated through a unit area parallel to the wavefronts The energy flux density, E, for plane waves is defined by

$$E = \frac{1}{\rho c} \int_{-\infty}^{\infty} p^2(t)dt \tag{4 3}$$

For sea water, $\rho c \approx 1\ 5\times10^5$ g/(cm^{2}s) $p(t)$ is the time varying pressure of the wave If pressure is expressed in the cgs units of dynes/cm^2, E is given in units of ergs/cm^2 If the plane wave signal is transient, the integration needs only to be performed through the time interval containing the significant arrivals The equivalent expression for energy flux density in the discrete time domain is

$$E = \frac{1}{f_s\ \rho c} \sum_{i=A}^{B} p^2(i) \tag{4 4}$$

where $p(i)$ is the true pressure for sample i, f_s is the sampling frequency, and A and B are the sample points which define the time window containing the arrivals of interest Before directly applying equation 4 4, the digital pressure units had to be converted to units of dynes/cm^2 The conversion relationship between digital $d(i)$, and real $p(i)$ pressure units was given by

$$d(i) = p(i)\ [\text{hpsens preamp pga scu adcon}]$$

where hpsens is the hydrophone sensitivity in V/(dyne/cm^2), preamp is the preamplifier amplification, pga is the programmable gain amplification, scu is the Signal Conditioning Unit amplification, and adcon is the analog to digital conversion factor Note that the preamplifier and scu amplifications were frequency dependent The meaning of the term amplification here refers to the increase in signal amplitude through each device $p^2(i)$ was thus expressed as

$$p^2(i) = d^2(i)\ [\text{hpsens preamp(f) pga scu(f) adcon}]^{\ 2}$$

The right hand side of this expression for $p^2(i)$ was substituted into equation 4 1 The resulting energy was converted to decibels, yielding the final expression for L

$$L = -10\log(f_s) - 10\log(\rho c) - 10\log(bw) + 10\log\left(\sum_{i=A}^{B} d^2(i)\right) \qquad (4\ 5)$$
$$- HPSENS - PREAMP - PGA - SCU - ADCON - BW$$

where the capitalized terms represent gains in decibels for the corresponding lower case amplifications e g ADCON = 10 log(adcon^2) Equation 4 5 is also convenient because the hydrophone sensitivity, preamplifier gain, programmable gain and signal conditioning unit gain were specified in decibels This equation was used to calculate the received energy levels in the beams of interest The beam containing the highest energy level for each shot was assumed to contain the specular reflection The level from this beam was therefore recorded as the measured energy flux density level for the respective shot

B. Propagation Loss Prediction

The method used for calculating bottom reflection losses requires the prediction of H_S (equation 2 3) This is the loss which occurs only in the water, and does not include any effects of the reflection interaction Because there was considerable variation of sound speed with depth in the ocean, the acoustic rays were not straight lines Consequently, a simple treatment, assuming spherical spreading loss given by -20 log(r), where r is the total acoustic path length, was not satisfactory In this work, the Generic Sonar Model (GSM) (Weinberg, 1985) was used to calculate the propagation loss GSM is a ray theory acoustic propagation model which accounts for focusing and diffusion effects resulting from refraction of acoustic paths in the water The environmental inputs provided to GSM included the ocean depth and the measured sound speed profile at each experimental site Additionally, the source depth, average array depth, and source to array range for each shot were provided GSM calculated the propagation losses for the four multipaths, associated with the single order bottom interaction, based on the environmental inputs for each shot The final propagation loss estimates were obtained by averaging these four loss values The propagation losses calculated for the shot ranges in run 1 are shown in figure 4 8

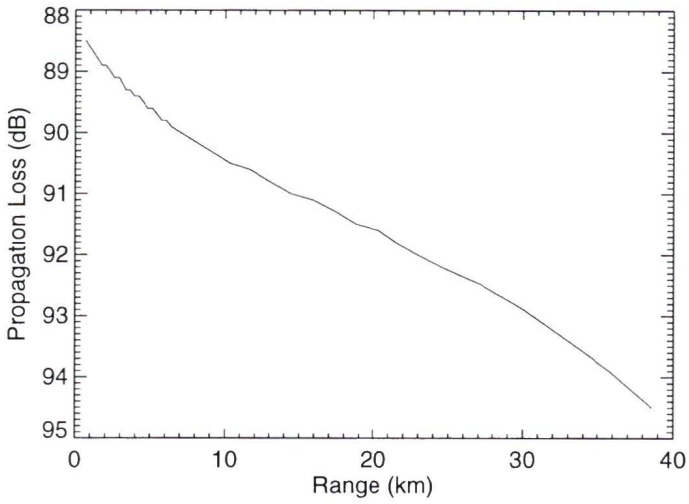

Figure 4 8 Propagation losses calculated by GSM for Run 1

An additional required output, produced by GSM, was the propagation angles for the acoustic paths at the source The bottom grazing angle (θ_G) for each shot was obtained from the angle at the source (θ_S) using Snell's law

$$\frac{C_S}{\cos\theta_S} = \frac{C_B}{\cos\theta_G} \tag{4 6}$$

where C_S and C_B are the water sound speeds at the depths of the source and bottom respectively Grazing angles determined this way were recorded for all shots

C. Reflection Loss Results

The measured reflection loss data were found to exhibit a high degree of variability or scatter There are two effects which contribute to the large amount of scatter in the reflection loss data for these experiments The first effect is acoustic scattering from the rough bottom Examination of figure 4 7a shows angular spread of the 8 Hz bottom interacting energy Most of the non-specularly scattered energy in the received signals was removed by beamforming, however, the presence of this energy indicates that the specular reflection also suffered partial scattering The energy lost from the specular reflection due to scattering was variable from shot to shot because bottom roughness was not uniform over the track of each run Referring to the Eckart scattering model (equation 2 4), we note that scattering loss is greatest at high angles Based on the measured small scale roughness at the experimental sites, s≈5-10 m, equation 2 4 predicts

additional loss due to scattering of approximately 1 to 3 dB at for 8 Hz waves Expected scattering losses near the critical angle (θ=55°) are approximately 0 5 to 2 dB, but fall off very rapidly with further decrease in grazing angle In some instances, fluctuation of the loss data by up to 5 dB was observed at high angles It is believed that these large fluctuations are a result of the existence of infrequently occurring areas of larger scale roughness

A second source of data scatter is due to variable sediment thickness In chapter 2 section III it was shown that the shear wave resonance effect is dependent on the ratio of the sediment thickness to the sediment shear wave wavelength A simple ray analysis, (Chapman and Chapman, 1993), shows that the resonance can create changes of several dB in reflection loss near the grazing angle of peak resonance when the sediment thickness varies by only 1/4 wavelength Because shear speed values in the sediment are approximately 100 - 300 m/s, shear wave wavelengths can be as small as 12 m for an 8 Hz wave Variability in the sediment thickness of even 1 m can therefore cause 1-2 dB change in the reflection loss data

Figure 4 9 shows the reflection loss versus angle data, measured from run 1 Due to fairly large amplitude of scatter in some of the calculated reflection loss data, three point smoothing was applied Figures 4 12 (a to i) show the smoothed results for all nine shot runs The smoothed reflection loss versus grazing angle data were used for inversion purposes

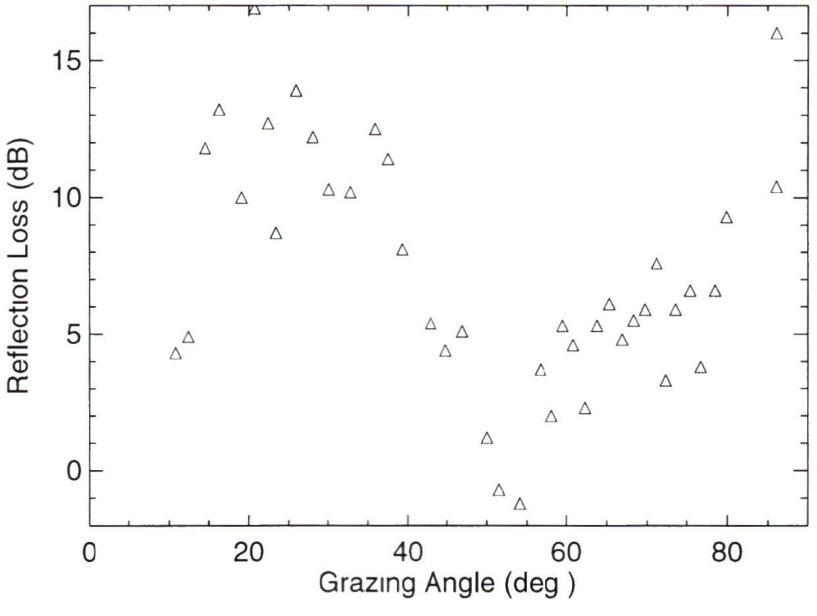

Figure 4 9 Unsmoothed Reflection Loss versus grazing angle data for Run 1

The minimum in the reflection loss data, occurring at approximately 50-55° grazing angle in figure 4 9, represents the compressional critical angle for the basalt at site 1 The high loss region between 15° and 40° is due to the shear wave losses in the sediment and basalt, including the resonance discussed in chapters 2 and 3 We note some very high loss values appearing in the loss data above 80° These high losses are probably due to scattering, and are not representative of the reflection loss mechanisms in our model

V. Inversion of Reflection Loss data

The iterative inversion method of chapter 2 was applied to each of the 9 experimental reflection loss versus grazing angle data sets The inversions were carried out by allowing 6 of the geoacoustic parameters, describing the two layer model, to vary within predefined search ranges The 6 parameters are those for which the cost function was found to be most sensitive in the simulation study of chapter 3 Simulated annealing optimization was used to find optimal values for the 6 parameters so that the best match between the measured and modeled reflection loss data was obtained These optimal values are the parameter estimates at each experiment site Because 3 of the 6 estimated parameters were shown to be highly sensitive to the noise that is exhibited by the scatter in the data, only the 3 most sensitive parameter estimates are believed to be reliable When the inversions were completed, a measure of uncertainty was calculated for each of the 3 highly sensitive parameters sediment shear wave speed, basalt compressional wave speed and basalt shear wave speed The uncertainty estimates were based on the final match between the modeled and measured loss, and the ranges of values accepted for each of the parameters during the inversion iterations

A. Parameter Ranges

The parameters included in the search were the sediment shear wave speed, shear wave attenuation, and density, and the basalt compressional wave speed, shear wave speed, and density The search limits used in the inversions for each of these parameters are given in table 4 3 The simulation study described in chapter 3 indicated that the inversion cost function was relatively insensitive to the remainder of the model parameters sediment compressional wave speed and compressional wave attenuation, and basalt compressional and shear wave attenuations Consequently, these parameters were fixed at reasonable values during the inversions The values for the fixed parameters and the parameters of the water are shown in table 4 4

Table 4 3 Search ranges for parameters included in the inversion search

Layer	Parameter	Search Range
Sediment	C_S (m/s)	100 - 250
	α_S (dB/λ)	1 0 - 3 0
	ρ (g/cm^3)	1 2 - 1 4
Basalt	C_D (m/s)	2600 - 3200
	C_S (m/s)	1000 - 1700
	ρ (g/cm^3)	2 0 - 2 5

Table 4 4 Fixed values for parameters omitted from the search

Layer	Parameter	Fixed Value
Water	ρ (g/cm^3)	1 0
	C_D (m/s)	1540
Sediment	C_D (m/s)	1535
	α_D (dB/λ)	0 1
Basalt	α_D (dB/λ)	0 3
	α_S (dB/λ)	0 5

B Simulated Annealing

The Simulated Annealing (SA) search for the optimal values of the six variable parameters was applied as follows At the start of each inversion, an arbitrary set of values for the 6 parameters was chosen (Each particular set of parameters is referred to as a model) The cost function value for this model was calculated from equation 2 6 This value was assigned to the SA energy (E) An initial value for temperature (T), and a cooling rate (h) were defined The inversion proceeded by performing 48000 model evaluation iterations, over which the temperature was slowly reduced The most computationally intensive step in the inversions was the calculation of the reflection loss values On each iteration, the reflection loss, at each grazing angle present in the measured data, was obtained by averaging the square magnitude of the reflection coefficients calculated at 8 equally spaced frequencies in the 1/3 octave band For run 1, which included reflection losses at 36 grazing angles, the 48000 iteration inversion

required 61 minutes of CPU time on a VAX 9000 The speed of this computer was approximately 15 MFLOPS

An initial temperature of T=1 0 and a cooling rate h=0 997 were found to be satisfactory for our data and 48000 iterations On each iteration, T was reduced by multiplying by h, and the current model was perturbed A model perturbation was performed by changing the value of a single parameter, and the parameters were varied in order as the iterations proceeded If we represent the current parameter value at some iteration as X, then the change, (ΔX), representing the model perturbation, was calculated according to a weighted distribution over the parameter's search interval

$$\Delta X = (2U_{0\,1}\text{-}1)^3/2*(X_U - X_L), \tag{4 4}$$

where $U_{0\,1}$ is a number produced by a random number generator between 0 0 and 1 0, and X_U and X_L are the upper and lower search range limits respectively The new parameter value was normally obtained by $X_{new} = X + \Delta X$, however when $X + \Delta X$ was outside the search interval, X_{new} was obtained by reflecting the sum back into the interval i e , if $X + \Delta X > X_U$, then $X_{new} = 2X_U - (X + \Delta X)$ The cube of $U_{0\,1}$ was taken to make small changes more probable than large ones Smaller parameter changes during model perturbation cause SA to sample the search space more densely around parameter values giving low energy than around values giving high energy

Perturbations which decreased E were always accepted Perturbations which increased E were accepted or rejected according to the size of the increase ΔE, and the current T The decision for acceptance was made according to the Boltzman distribution of equation 2 7 $P(\Delta E) = \exp(-\Delta E/T)$ When a new model was accepted, the parameter values were stored, and the new energy became the current accepted energy E At the start of each inversion, the accepted energy fluctuated largely due to the relaxed acceptance criterion at high temperatures As the temperature slowly decreased, large increases of energy became gradually less probable, so the accepted energy range narrowed and tended to move to smaller values This behavior is evident in the plot in figure 4 10 which shows accepted energy versus iteration number during run 7

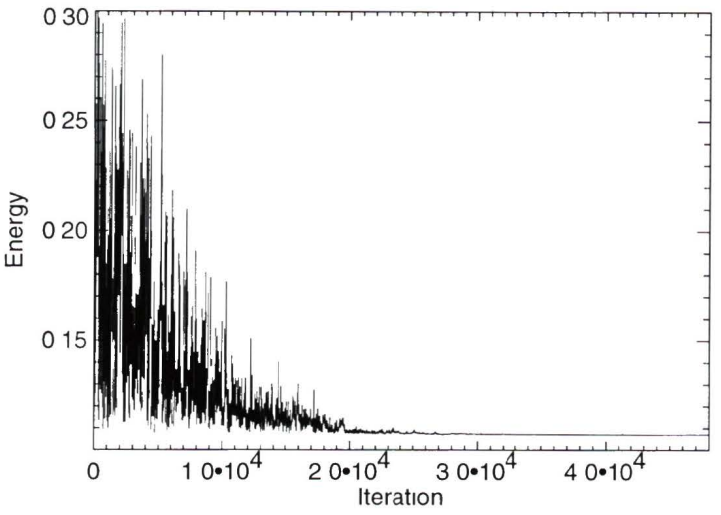

Figure 4 10 Accepted Simulated Annealing energy during run 7

As the iterations proceeded, the parameters moved through their respective search ranges Figures 4 11 (a to e) show the current model parameter values versus iteration during the iterative search for run 7

It was found that parameter estimates "froze out" during the inversion iterations at temperatures related to the respective cost function sensitivities The term "freezing out" refers to the restriction of the respective parameter values to ranges much less than their defined search ranges Freezing out occurs when the range of currently accepted energy values is lower than that which is produced by varying the parameter through its entire range It is apparent in figures 4 11 (c,e,f), that the parameters basalt density, sediment shear attenuation and sediment density have frozen out at one of their respective search limit values It is unlikely that the estimates for these three parameters are representative of the true physical parameter values at the site of shot run 7 The poor estimates for these parameters are attributed to the scatter in the measured data, as discussed previously We note that these three parameters were found to be sensitive to "noisy" data in the simulation study The three most sensitive parameters basalt compressional and shear wave speeds and sediment shear wave speed, however, were found to be much less sensitive to noise in the same study The estimates for these parameters are likely representative of the true physical values at the experimental site of run 7

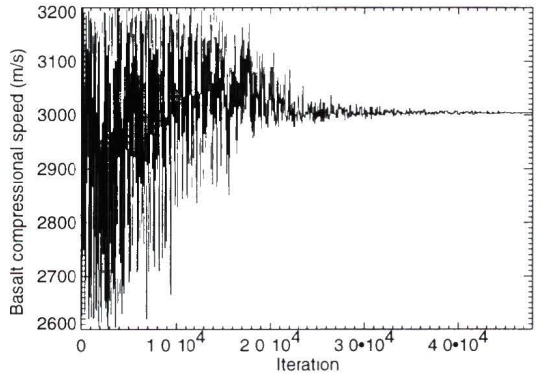

a Basalt C_p

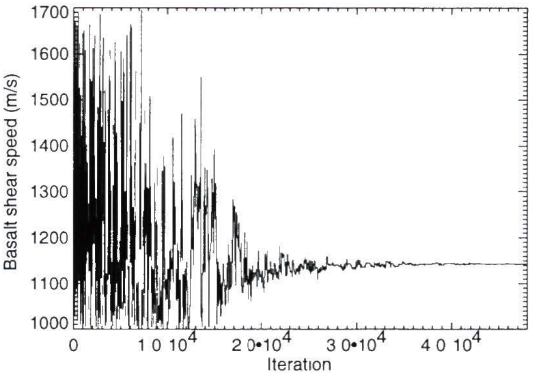

b Basalt C_s

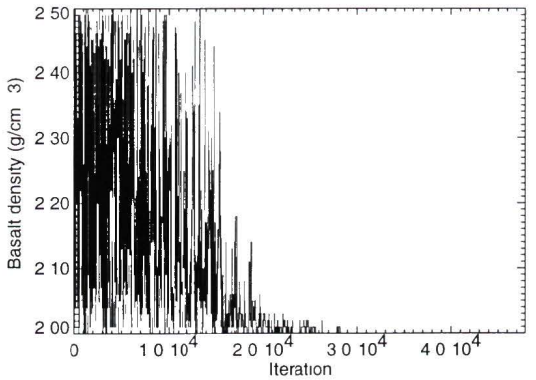

c Basalt ρ

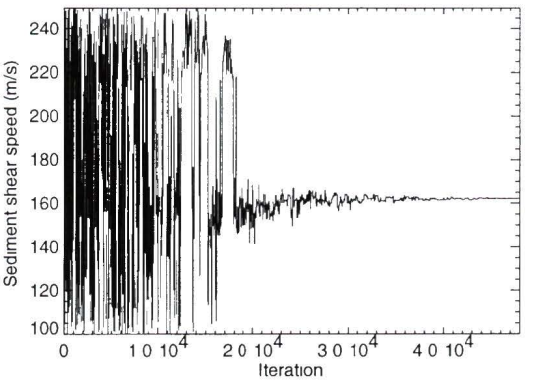

d Sediment C_s

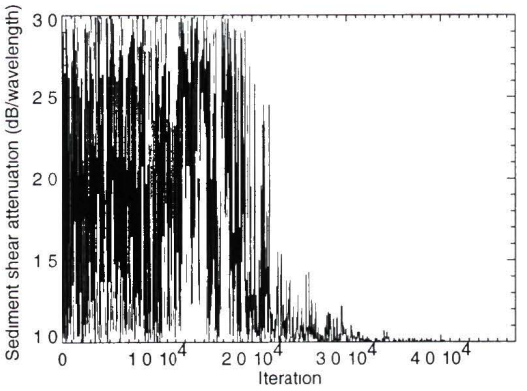

e Sediment α_s

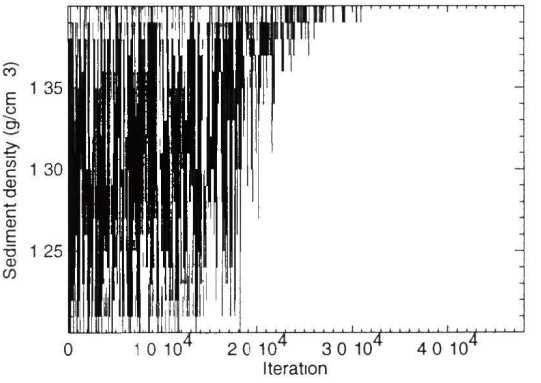

f Sediment ρ

Figure 4 11 Accepted model parameter values during run 7

C. Results

At the end of each inversion, the final accepted model was recorded Figures 4 12 (a to i) show the reflection loss versus angle calcuated for the accepted models for each run plotted with the corresponding experimental data

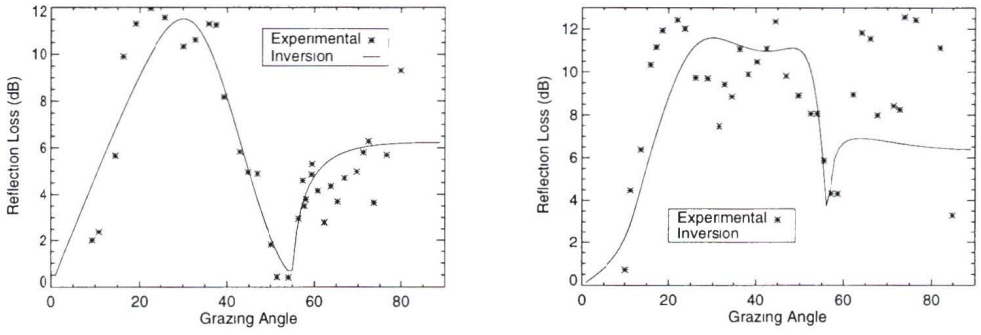

a Run 1

b Run 2

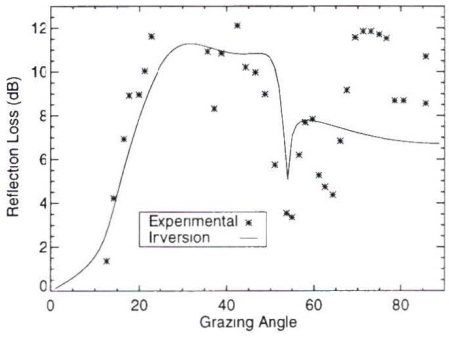

c Run 3

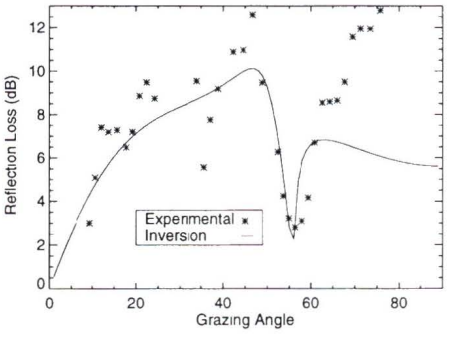

d Run 4

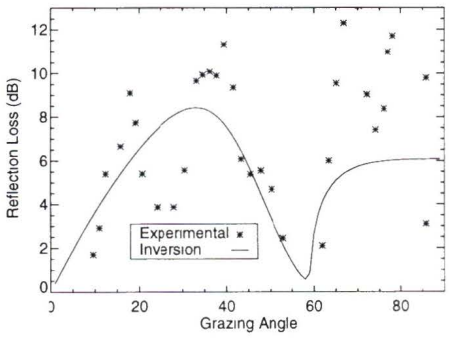

e Run 5

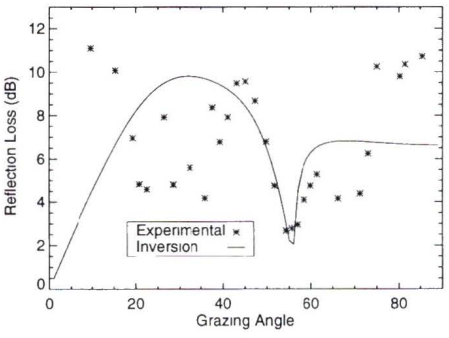

f Run 6

Figure 4 12 Measured and inversion result reflection losses

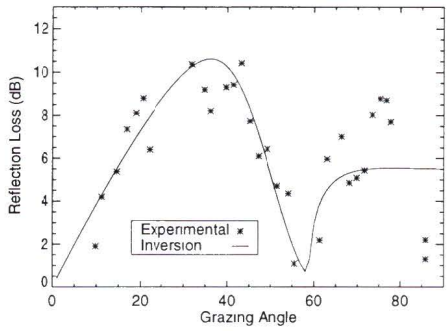

g Run 7

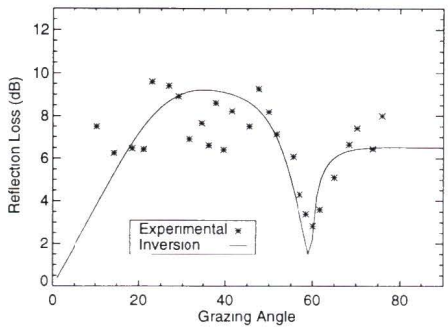

h Run 8

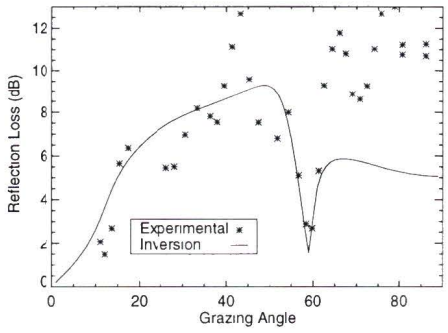

ı Run 9

Figure 4 12 continued

The parameter values describing the final models for each inversion were used as the parameter estimates at the experimental sites Because the simulation study showed that basalt density, sediment shear attenuation and sediment density estimates are sensitive to scatter in the measured data, and since the inversion results often lay on the search range limits for these parameters, the estimates are not reliable Consequently only the estimates for basalt compressional wave speed and shear wave speed and sediment shear wave speed are presented The final estimates for these three parameters are given in table 4 5

Table 4 5 Parameter estimates at experiment sites

Site	Sediment C_s	Basalt C_p	Basalt C_s
1	250 0±61 2 m/s	2713±39 m/s	1050±25 m/s
2	177 8±32 0 m/s	2804±65 m/s	1574±7 m/s
3	171 6±31 4 m/s	2622±31 m/s	1586±9 m/s
4	179 2±5 1 m/s	2763±41 m/s	1487±27 m/s
5	162 2±21 9 m/s	3004±61 m/s	1143±39 m/s
6	229 0±21 9 m/s	2812±58 m/s	1383±33 m/s
7	151 8±2 2 m/s	2990±63 m/s	1216±28 m/s
8	246 2±2 4 m/s	3075±62 m/s	1482±25 m/s
9	173 0±25 9 m/s	3050±28 m/s	1581±6 m/s

The uncertainties given for the parameter estimates in table 4 5 are based on the range of models accepted during a segment of iterations in the respective iterative searches The range of accepted parameter values decreases as the search proceeds, therefore the position of the segment is important The position of the segment was determined based on the "goodness of fit" of the final model reflection losses to the respective measured data, as measured by the final energy The iteration number, where the accepted energy vs iteration curve crossed a value 5% greater than the final energy, was first identified Because the accepted SA energy fluctuated rapidly, a 500 point moving average was applied to increase the smoothness so that the crossover iteration could be identified more easily A 1000 iteration segment of the accepted models, centred at the crossover iteration, was extracted and the standard deviation of accepted parameter variation within the segment was calculated These standard deviations were taken as the parameter uncertainties Uncertainties calculated this way cannot be given explicit confidence, however, they represent relative confidences which are based on the physics of the cost function sensitivities and the SA inversion process Uncertainties for parameters, to which the cost function is insensitive, are relatively high because greater parameter value variation is required to cause the same change in the SA energy When a poor final fit is obtained, the final energy and crossover energy are high A larger range of accepted values for all parameters occurs at higher energies, so the calculated uncertainties are greater

VI. Discussion of Experimental Inversion Estimates

A. Sediment Shear Wave Speed Estimates

The sediment shear wave speed search range was 100 m/s to 250 m/s We note, from the shear speed estimates in table 4 5, that the estimates at 5 of the 9 sites lie between 160 m/s, and 180 m/s One estimate is lower at 151 8 m/s, and the remaining 3 are 229 0 m/s, 246 2 m/s, and 250 0 m/s The only parameter estimate which froze out at a search range limit was the sediment shear wave speed at site 1 This estimate (250 m/s) also has the highest uncertainty value of all the sediment shear wave speed estimates

The simulation study from chapter 3 was performed on simulated data calculated from a geophysical model with a sediment shear speed of 180 m/s This shear wave speed coincidentally agrees approximately with the estimated speeds at 5 of the sites In the simulation study, the cost function was found to have non-global minima at sediment shear speeds of approximately 147 m/s, 202 m/s, and 250 m/s If it was assumed that the true sediment shear speed at the experiment sites was between 160 m/s and 180 m/s, then the low estimate at 151 8 m/s and the highest estimate at 250 m/s could arise if a local minima was mistakenly identified by the search In fact, the presence of physical influences on the data, such as acoustic scattering effects and sediment thickness variability, could enhance the local minima and/or diminish the correct global minimum, thus forcing the search to identify one of the local minima

It is believed that the true sediment shear speed is represented by the consistent estimates at 5 of the 9 experiment sites These estimates indicate speeds in the range 160 m/s to 180 m/s The 4 estimates outside of this range likely arise due to the effects described above

B. Basalt Compressional and Shear Wave Speed Estimates

The basalt compressional search range was 2600 m/s to 3200 m/s, and the shear wave search range was 1000 m/s to 1700 m/s Table 4 5 contains the compressional and shear speeed estimates for the basalt at each site and we note that none of these estimates froze out on the range limits In general, the uncertainties for these estimates were significantly less than those for sediment shear wave speed, as a fraction of the search range We therefore place more relative confidence in the basalt speed estimates The estimates for the basalt compressional and shear wave speeds are plotted in figure 4 13 as a function of the geologic age of the basalt at the respective experiment sites

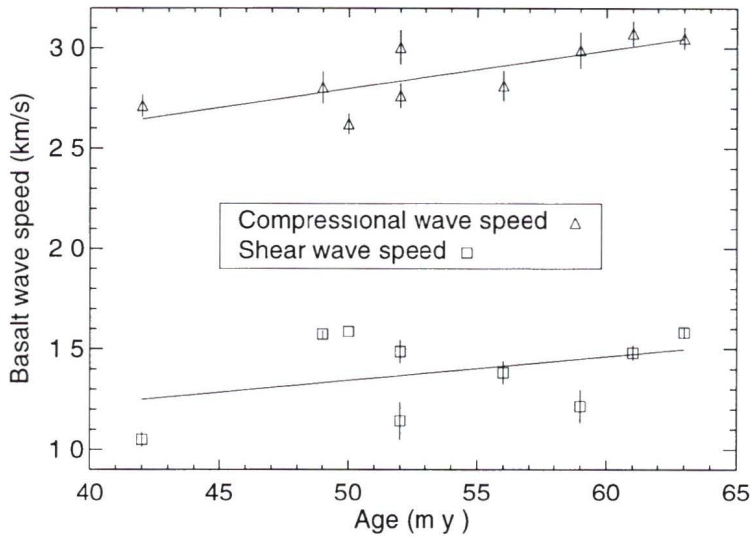

Figure 4 13 Basalt compressional and shear wave speed estimates versus basalt age

We note from figure 4 13, that trends of increasing speed with age are apparent for both the compressional and shear wave speeds Linear regression fits, represented by the solid lines in figure 4 13, indicate wave speed versus age slopes of 19 0±17 6 m/s/m y and 11 8±32 3 m/s/m y respectively for compressional waves and shear waves The zero age intercepts were 1847±946 m/s and 755±1734 m/s The large uncertainties in the intercepts occur because of the fairly large uncertainties of the slopes, and we are extrapolating back a period nearly twice the actual range of ages observed The regression results give Poisson's ratios, (Kolsky, 1963), of 0 356 for the 42 m y basalt and 0 340 for the 63 m y basalt These values are somewhat less than measured values ≥ 0 38 , (Vera et al, 1990) for 0 m y - 0 2 m y layer 2A crust, however this would be expected if porosity decreased with basalt age as hypothesized by Jacobson, (Jacobson, 1992)

5. Conclusions

I. Method Overview

An iterative search inversion method was proposed for estimating geoacoustic properties of the pelagic sediment and basalt in thinly sedimented areas in the Abyssal Hills region of the North Pacific The method uses low frequency bottom reflection loss versus grazing angle measurements, obtained from experiments which use a towed line array to resolve the bottom reflected acoustic energy of the specular path Existing geophysical inversion methods, requiring direct measurement of arrival times and amplitudes from individual acoustic paths, are not well suited for measuring the sediment properties and upper basalt properties over this very large region The reason for this is that signals from several paths arrive nearly simultaneously, thus interfering with each other so that arrival time and amplitude measurement is difficult Additionally, bottom roughness causes severe acoustic scattering which obscures the acoustic paths of interest The proposed inversion method exploits the characteristics of the interference between closely occurring acoustic paths The effects of scattering are reduced by beamforming, and data analysis is restricted to low frequencies for which scattering effects are less important

Once experimental data are obtained, implementation of the model is straight forward The ocean bottom is modeled by a general two solid layer system which represents the sediment and basalt layers The 10 geoacoustic parameters which influence the reflection loss are the compressional wave sound speeds and attenuations, the shear wave sound speeds and attenuations, and the densities of the two layers The values for the parameters (sediment compressional speed and attenuation and basalt compressional and shear attenuation) are fixed at reasonable values during each inversion Possible models are described by values for the remaining six parameters A search of all possible bottom models of this kind is performed to find the model which produces reflection loss versus angle characteristics best matching the measured data A measure of match is defined as the rms difference between the square roots of the measured and model reflection loss values Because the number of possible models is very large, an exhaustive search is precluded by the computational time required to calculate reflection losses for all models The search is made tractable by using Simulated Annealing optimization to perform an efficient search of the possible bottom models

II. Simulation Study Findings

A simulation study was performed to test the ability of the method to provide reliable estimates for each of the parameters The study was carried out using a simulated set of reflection loss data which were calculated for a test environment described by a set of realistic geoacoustic parameter values These simulated data were used in place of experimental data

An analysis of the cost function sensitivity to each of the parameters was performed by observing the Simulated Annealing cost function variance as the parameters were moved individually through their respective search ranges This analysis indicated that considerable difference in cost function sensitivity existed between parameters Inversion estimates for parameters to which the cost function is insensitive, are less reliable than those for parameters which effect the cost function strongly Parameter sensitivities could be categorized in three levels highly sensitive, moderately sensitive, and insensitive These levels were separated by an order of magnitude of sensitivity The parameters found to be highly sensitive were the sediment shear wave speed, basalt compressional wave speed, and basalt shear wave speed Parameters in the moderately sensitive category were the sediment and basalt densities, and the sediment shear wave attenuation Relatively insensitive parameters were the sediment compressional wave speed, the sediment compressional attenuation, and the basalt compressional and shear attenuations

The first test of the inversion method was performed using the unmodified simulated data Because of the extremely small influence of the four parameters in the least sensitive category above, these four parameters were excluded from the inversion The method was found to reproduce all of the remaining six test environment parameters with high accuracy Because some degree of scatter exists in all measured data, random errors were added to the generated data to simulate experimental data more realistically The inversion method was applied to the modified data at three separate noise levels typical of real reflection loss data Only the estimates for the three parameters in the highly sensitive category above remained accurate at all noise levels tested These three parameters however are the parameters which most strongly influence the reflection loss characteristics, and therefore are the parameters of greatest interest to scientists interested in acoustic interactions with the ocean bottom

III. Method Application to real data.

The iterative search inversion method was applied to reflection loss versus angle data obtained at nine sites along an East-West experimental track in the North Pacific The track was significant because the age of the underlying basalt increased from approximately 42 m y at the East end to 63 m y at the West end Estimates were obtained for the sediment shear wave speed and the basalt compressional and shear wave speeds at each site Sediment shear speed estimates indicate a value between 160 m/s and 180 m/s Trends of increasing basalt compressional and shear wave speeds were found for experiment sites increasingly Westward The basalt compressional wave speed estimates ranged from 2622 m/s to 3075 m/s Basalt shear wave speed estimates ranged from 1050 m/s to 1586 m/s Linear regression analyses of the wave speed estimates versus basalt age indicated increasing speed with age for both compressional waves and shear waves These regressions indicate rates of increase of 19 0±17 6 $^{m/s}/_{m\,y}$ for compressional waves and 11 8±32 3 $^{m/s}/_{m\,y}$ for shear waves

The upper crust basalt sound speed estimates provide the first test of the findings of the Houtz and Ewing data (Houtz and Ewing, 1976) over a well defined transect at moderate age (42-63 my) The Houtz and Ewing data indicated increasing compressional wave speed with basalt age, however their data contained a very high degree of scatter Jacobson's hypothesis attributes increasing compressional wave speed with age, to basalt alteration occurring when cracks and faults are filled by minerals precipitated from hydrothermally circulated seawater, (Jacobson, 1992) The hypothesis suggests that the increases in speed result from the higher bulk and shear moduli in the altered basalt A recent study on 0-4 5 m y basalt correlated rapid increases in basalt compressional speed with changes from open to closed hydrothermal circulation of seawater through the overlying sediment layer, (Rohr, 1994) This study indicated that alteration proceeded at a slow rate when open circulation was maintained In the present work, the sediment layer is thin (<33m) over the entire experimental track studied The possibility that open circulation is still occuring at the experiment sites is real The present estimates are very low in comparison with previous estimates for similar age basalt These results would indicate that the rate of alteration has been slow, and so they are consistent with the hypothesis that open circulation is continuing at the sites studied

IV. Suggestions for Further Research

A primary problem for applying data-matching inversion techniques, such as the iteration of forward models method described in this thesis, is the incorrect modeling of the experimental environment Two of the modeling problems encountered for the reflection loss data inversion were that bottom roughness and sediment thickness variability could not easily be accounted for The latter of these problems could have been solved by measuring sediment thickness at every reflection point This operation however would require considerable effort A preferable option is to modify the experimental method so that the reflection point remains relatively constant throughout each shot run This in fact has been done in later reflection loss versus angle measurement shot runs at different locations, e g (Hannay, 1993), and (Hannay, 1994) These expanding spread profile (ESP) endfire shot runs are performed using the same experimental equipment used in the broadside shot runs for the experiment described in chapter 4 (figure 4 2), but the source ship and tow ship move in antiparallel directions at the same speed A diagram of the endfire geometry is shown in figure 5 1

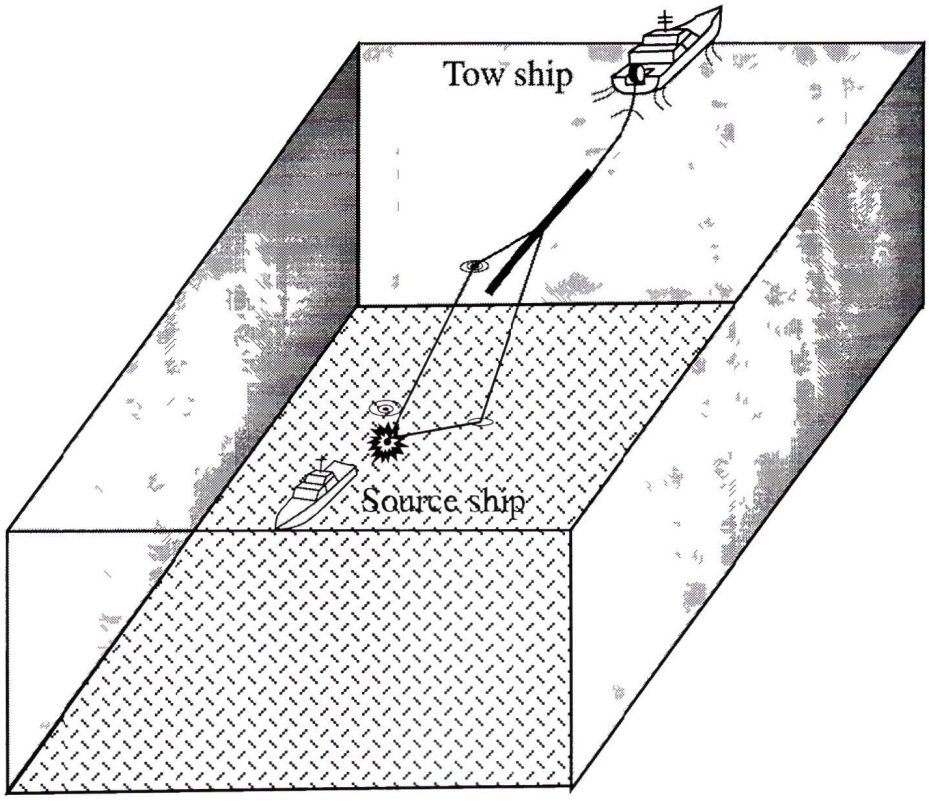

Figure 5 1 Endfire ESP shot run geometry

Significantly less scatter is observed in the endfire experimental data at all grazing angles than for broadside shot run data This type of run also allows the experimenters to choose the reflection position in advance Random scattering effects can be reduced by choosing a reflection position where bottom roughness is small

One very important aspect of the reflection loss characteristics for thin sediment sites is the shear wave resonance effect described in chapter 2 section III Figure 2 3 shows the significant structure that is apparent in reflection loss as a function of frequency Our inversion method, as defined, only considered the average magnitude of the sediment shear wave interference pattern over a frequency band smaller than the resonance frequency interval As discussed previously, the resonance frequency interval is directly related to the sediment shear speed and sediment thickness The rate at which the resonance peaks decay with frequency is related to the sediment shear wave attenuation An analysis which exploited this resonance information might reveal information regarding the sediment shear wave speed and attenuation parameters The main problem for performing such an analysis would be to obtain reflection losses in narrow frequency bands Before this could be accomplished, SUS charge levels in the narrow bands would have to be measured Currently, SUS charge levels are available only in 1/3 octave bands which are too wide for the analysis required Once SUS charge levels were available, the analysis could be performed using only a single SUS charge reflection waveform The SUS charge range would be chosen so that the grazing angle was close to the maximum angle of the resonance effect This would be approximately 30° to 40° for the environments at the experiment sites considered in chapter 4

Finally, the application of the inversion method to data collected close to spreading centre axes would be valuable for obtaining sound speed estimates in very young crust Recent experiments at the East Pacific rise (Harding *et al* , 1989), (Vera *et al* , 1990), and (Christeson, Purdy, and Fryer, 1992) have established very low compressional speeds of 2 2 km/s and 2 3 km/s near the axis Recent reflection loss versus angle data have been collected during endfire ESP experiments in very young crust, (Hannay, 1993) and (Hannay, 1994) The proposed iterative search method should be capable of confirming the low compressional speed values, and should be capable of providing new shear wave speed estimates

V. Summary

In conclusion, it has been shown that the iterative inversion method developed in this thesis can be effective for estimating the sediment shear wave speed, and the upper crust basalt compressional and shear wave speeds from reflection loss versus angle data obtained in thin sediment areas of the Abyssal Hills region of the North Pacific The method is important because accurate estimates for the uppermost basalt cannot easily be obtained using the existing geophysical techniques This is evidenced by the large scatter in a compilation of historical data for basalt sound speeds, (Houtz and Ewing, 1976) The application of the method to experimental data gave estimates for upper crust basalt compressional speeds which increased with basalt age The method also provided the first basalt shear wave speed versus age estimates These estimates also increased with age, but the scatter was too great to conclude, on the basis of the shear speed estimates alone, that a trend exists An increase of basalt compressional speed with age was suggested by the Houtz and Ewing data, and the present results are consistent with this observation

References

Atwater, T and J Severinghaus,

Tectonic maps of the northeast Pacific, in The Eastern Pacific Ocean and Hawaii, E L Winterer, D M Hussong, and R W Decker, eds , Geological Society of America, 1989

Brekhovskikh, L M

Waves in Layered Media, second edition, (Academic Press, New York) p 1 - 59, 1980

Burdic, W ,

Underwater Acoustic Systems Analysis second edition, (Prentice Hall, Englewood Cliffs, N J), p , 303 - 324, 1991

Chapman, N R ,

Source levels of shallow explosive charges, Journal of the Acoustical Society, of America, Vol 84, p 679 - 702, 1988

Estimation of geoacoustic properties by inversion of acoustic field data, in Shear Waves in Marine Sediments, edited by J Hovem, M Richardson, and R Stoll, (Kluwer, Dordrecht), p 511 -520, 1991

Chapman, N R and D M F Chapman,

A coherent ray model of plane-wave reflection from a thin sediment layer, Journal of the Acoustical Society of America, Vol 94, p 2731 - 2738, 1993

Christensen, N I and M H Salisbury,

Structure and constitution of the lower oceanic crust, Reviews of Geophysics and Space Physics, Vol 13, p 57 - 86, 1975

Christesen, G L , G M Purdy, and G J Fryer,

Structure of young upper crust at the East Pacific Rise Near 9° 30′ N, Geophysical Research Letters, Vol 19, No 10, p 1045 - 1048, 1992

Christian, E A and M Blaik,

Near surface measurements of deep explosions II Energy spectra of small charges, Journal of the Acoustical Society of America, Vol 38, p 57 - 62, 1965

Diachok, O I , R L Dicus, and S C Wales,

Elements of a geoacoustic model of the upper crust, Journal of the Acoustical Society of America, Vol 75, p 324 - 334, 1994

Frisk, G V

Inverse methods in ocean bottom acoustics, in Oceanographic and Geophysical Tomography, edited by Y Deaubies, A Tarantola, and J Zinn-Justin, North-Holland Elsevier Science Publishers B V , p 410 - 437, 1990

Gaspin, J B , and V K Shuler,

Source levels of shallow underwater explosives, Naval Ordnance Laboratory NOTLR 71 - 160, October 13, 1961

Hamilton, E L

Geoacoustic Modeling of the Sea Floor, Journal of the Acoustical Society of America, Vol 68, p 1313 - 1340, 1980

Shear Wave Velocity Versus Depth in Marine Sediments a Review, Geophysics, Vol 41, p 985 - 996, 1976

Hannay, D E

Bottom Loss Processing of the Pacific Echo IV Experiment Data, D R E P Contractor report number 94-52, May 1994

Bottom Loss Processing of the Pacific Echo III Experiment Data, D R E P Contractor report number 93-32, May 1993

Harding, A J , J A Orcutt, M E Kappus, E E Vera, G C Mutter, P Buhl, R S Detrick, and T M Brocher,

Structure of Young Oceanic Crust at 13° N on the East Pacific Rise From Expanding Spread Profiles, Journal of Geophysical Research, Vol 94, 12,163 - 12,165, September 1989

Henson N G , D E Hannay, P Scrimger, and S E Dosso,

Efficient Acoustic Field Computation for Estimating Geoacoustic Bottom Parameters using Matched Field Inversion, in Full Field Inversion Methods in Ocean and Seismic Acoustics, Ed P Gerstoft and O Diachok, NATO conference series, Presented at conference June 1994 at LaSpezia Italy, Publication Pending

Houtz, R , and J Ewing,
Upper crustal structure as a function of plate age, Journal of Geophysical Research, Vol 81, p 2490 - 2498, 1976

Hughes, S J , D M F Chapman, and N R Chapman,
Effect of shear wave attenuation on acoustic bottom loss resonance, in Shear Waves in Marine Sediments, edited by J Hovem, M Richardson, and R Stoll, (Kluwer, Dordrecht), p 436 - 439, 1991

Hughes, R ,
"Underwater explosives scaling of source spectra," in Underwater acoustics and signal processing, edited by L Bjorno, (Reidel, New York), p 87 - 91, 1981

Jacobson, R S ,
Impact of Crustal Evolution on Changes of the Seismic Properties of the Uppermost Ocean Crust, Reviews of Geophysics, Vol 30, p 24 - 28, Feb 1992

Kolsky, H ,
Stress Waves in Solids, (Dover, New York), 1963

Kormendi, F , and M Dietrich,
Nonlinear waveform inversion of plane-wave seismograms in stratified elastic media, Geophysics, Vol 56, No 5, p 664 - 674, May1991

Pilant, W L ,
Elastic Waves in the Earth, (Elsevier, New York), p 43 - 44, 1979

Press, W H , B P Flannery, S A Teukolsky, W T Vetterling,
Numerical Recipes, FORTRAN edition,
(Cambridge University Press), p 326 - 334, 1986

Purdy, G M ,
New Observations of the Shallow Seismic Structure of Young Oceanic Crust, Journal of Geophysical Research, Vol 92, No B9, p 9351 - 9362, 1987

Rohr, K ,
Increase of Seismic Velocities in Upper Oceanic Crust and Hydrothermal Circulation in the Juan de Fuca Plate, Geophysical Research Letters, Vol 21, p 2163 - 2166, Sept 1994

Rohr, K ,

Variations of the Amplitudes of Reflections from old Oceanic Basement in the North Atlantic, Journal of Geophysical Research, Vol 92, No B10, p 10,581 - 10,594, 1987

Rohr, K , U Schmidt, and H Groschel-Becker,

Regional Patterns of Hydrothermal Alteration of Sediments as Interpreted from Seafloor Reflection Coefficients, Middle Valley, Juan de Fuca Ridge, Geophysical Research Letters, Vol 20, p 1867 - 1870, Sept 1993

Sen, M K and P L Stoffa,

Nonlinear One-Dimensional Seismic Waveform Inversion using Simulated Annealing, Geophysics, Vol 56, No 10, p 1624 - 1638, 1991

Singh, S C , G F West, N D Bregman and C H Chapman,

Full Waveform Inversion of Reflection Data, Journal of Geophysical Research, Vol 94, No B2, p 1777 - 1794, 1989

Stockhausen J H ,

Energy per unit area spectrum of the shock wave from 1-lb TNT charges exploded under water, Journal of the Acoustical Society of America, Vol 36, p 1220, 1964

Taylor, T T ,

Design of Line-Source Antennas for Narrow Beamwidth and Low Side Lobes, I R E Transactions - Antennas and Propagation, Jan 1955, p 16 - 27

Toomey, D R , G M Purdy, S C Solomon, and W S D Wilcock,

The three dimensional Crustal Sructure of the East Pacific Rise near Latitude 9° 30′ N, Nature, Vol 347, p 639 - 645, 1990

Turner, R G , and J A Scrimger,

On the depth variation in the energy spectra of underwater explosive charges, Journal of the Acoustical Society of America, Vol 48, p 775 - 778, 1970

Vera, E E , J C Mutter, P Buhl, J A Orcutt, A J Harding, M E Kappus, R S Detrick, and T M Brocher,

The structure of 0- to 0 2-m y -old oceanic crust at 9° N on the East Pacific Rise from expanding spread profiles, Journal of Geophysical Research, Vol 95, p 15,529 - 15,556, 1990

Weinberg, H ,

Generic Sonar Model, Naval Underwater Systems Center Technical Document 5971D, June 6, 1985

Weston, D E ,

Underwater explosions as acoustic sources, Proceedings of the Physics Society of London, Vol 76, Sect B, p 233 - 249, 1960

Wilkins, R , G J Fryer, and J L Karsten,

Evolution of porosity and seismic structure of upper oceanic crust Importance of aspect ratios, Journal of Geophysical Research, Vol 96, p 17,981 - 17,885, 1991

Yee, W ,

Source Levels of shallow Sound Sources,
Defense Research Establishment Pacific, Contractors report 91-18, August 1991

Zelt, C A and R B Smith

Seismic Traveltime Inversion for 2-D Crustal Velocity Structure,
Geophysics Journal International, Vol 108, No 1, p 16 - 34, 1992

Appendix A
Source level measurements from depth-scaled spectra of 0.82 kg SUS charges

I. Introduction

The 0 82 kg SUS (Signal Underwater Sound) charge is commonly used in experiments designed to measure the acoustic propagation characteristics of the ocean, and to probe the upper layers of the ocean bottom Accurate knowledge of the 1/3 octave band source levels of the charges is required in the frequency range from a few Hz to a few hundred Hz, at detonation depths from approximately 20 m to 300 m These levels have been determined by experiment, e g (Stockhausen, 1964), (Christian and Blake, 1965), and (Turner and Scrimger, 1970), and by a variety of theoretical techniques, e g (Weston, 1960) and (Gaspin and Schuler, 1971) The results from these analyses, however, contain considerable differences Consequently, a highly controlled experiment and analysis was carried out by Chapman, (Chapman, 1988), to further quantify the levels His published values for the 1/3 octave source levels were obtained from an analysis of the spectra from more than 30 charges detonated at each of the depths 23 5 m, 99 6 m, 194 4 m Additionally, Chapman used a spectrum scaling method (Hughes, 1981) to scale his 194 4 m charge spectra to obtain levels at 244 m These source levels in the preferred 1/3 octave bands from 5 Hz to 630 Hz are now widely accepted and are the most frequently used

However, a complication occurs because the source levels vary significantly over the depth intervals observed for SUS charges set to detonate at specific depths We have performed an analysis of Chapman's experimental data to obtain accurate source levels over a range of depths close to each of the depths specified in Chapman's original work We have also analysed new data from 7 charges detonated near 50 m The spectral scaling method of Hughes was used to scale all charge spectra at each approximate depth to several depths within corresponding ranges representing the variability in observed detonation depth The ranges, and step sizes, are 17-27 m in 1 m steps, 40-60 m in 2 m steps, 84-104 m in 2 m steps, 170-210 m in 4 m steps and 230-280 m in 5 m steps Levels are presented for the same frequency bands analysed by Chapman The levels were obtained by averaging 1/3 octave band levels measured from the depth-scaled spectra

II. Experiment

The experiment was designed to provide high resolution recordings of the acoustic waveforms from 0 82 kg SUS charges, set to detonate at depths of 18 m, 50 m, 90 m, and 183 m A diagram of the experimental geometry is shown in figure 6 1

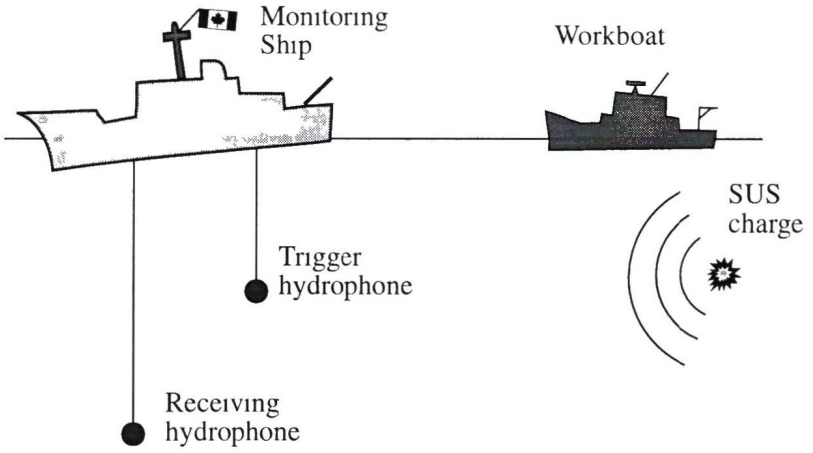

Figure 6 1 SUS charge experiment geometry

The experiment was performed in Jervis Inlet, located 90 km North of Vancouver, British Columbia The site was ideal in that it was sheltered from low frequency noise and because the water depth was deep enough (>600 m) so that bottom reflected energy would not interfere with the direct path signal of interest Charges were dropped from a work boat at ranges between 150 m and 450 m from the monitoring ship The receiving hydrophone was suspended below the recording ship at a depth of 488 m The slant range from the sources to the hydrophone was always greater than about 200 m so that finite amplitude effects from shock waves could be neglected Also, the large depth of the hydrophone maximized the delay of the surface reflected signal with respect to the direct path signal However, the surface reflected signal contaminated the waveforms of the shallow 18 3 m charges

The receiving hydrophone was an Atlantic Research Corporation barium titanate BC-32 hydrophone Its sensitivity was calibrated after the experiment to be -213 ± 1 dB re 1 V/Pa over the frequency range from 5 Hz to 5 kHz An underwater preamplifier drove the cable to the surface where the signal was amplified and filtered The frequency response of the preamplifier, cable, amplifier and filter was calibrated at +5 2 dB flat out

to 20 kHz with a low frequency roll-off at about 3 Hz The analog output of the system was digitized by a 15-bit A/D at a rate of 50000 samples per second Digital output was stored directly on magnetic tapes

III. Explosion waveforms

Figure 6 2 shows a typical waveform for one of the 193 m charges The waveform consists of a shock pulse followed by several bubble pulses The shock pulse rises nearly instantaneously, corresponding to the rapid conversion of the solid T N T to gaseous form The resulting gas globe is initially highly pressurized This globe expands quickly and overshoots its equilibrium volume due to the momentum imparted to the surrounding water The equilibrium volume occurs when the globe pressure is equal to the ambient hydrostatic water pressure, and corresponds with the first zero crossing in the pressure waveform The minimum pressure occurs when the gas globe reaches its maximum volume After the time of minimum pressure, the globe begins to contract The volume of the globe continues to decrease, and again overshoots the pressure equilibrium The point at which the volume again reaches a minimum is represented by the second positive peak in the waveform This peak is referred to as the first bubble pulse The process repeats after the first bubble pulse, causing the cyclic nature of the waveform

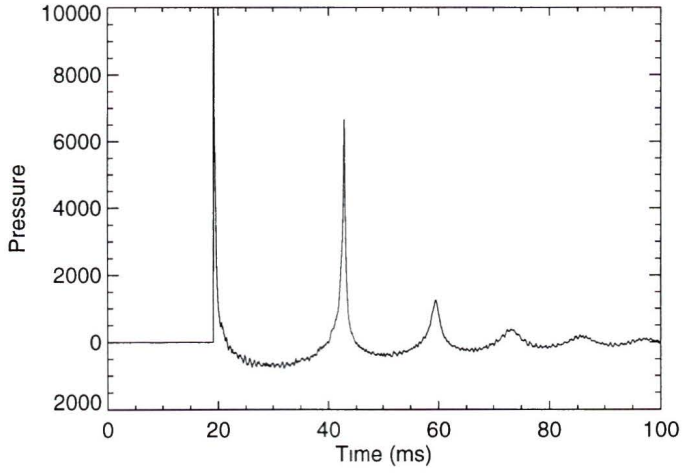

Figure 6 2 Pressure waveform for a 193 m charge

The time period from the peak of the shock pulse to the peak of the first bubble pulse is referred to as the first bubble pulse period This period, (T_{bub}), is known to vary with the depth of charge detonation as

$$T_{bub} = 2\ 11 W^{1/3} Z_0^{\ 5/6} \qquad (6\ 1)$$

where W is the charge mass in kilograms and Z_0 is the hydrostatic depth, given by $Z + 10\ 1$ m We notice that the first bubble pulse period for the 193 m charge is approximately 24 ms, while the bubble pulse period for a 23 m charge, shown in figures 6 3 and 6 4, is approximately 110 ms This difference is consistent with equation 6 1

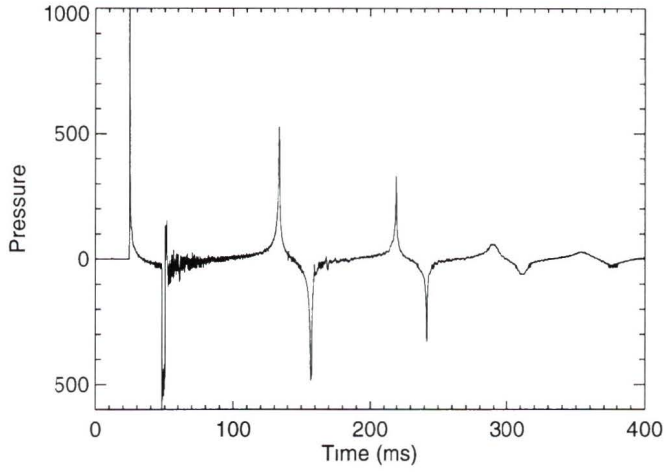

Figure 6 3 Pressure waveform for a 23 m charge showing surface reflected signals

A noticeable feature in the 23 m waveform in figure 6 3 is the appearance of negative pulses These pulses are due to surface reflected acoustic energy The surface reflected signal is an inverted replica of the direct path waveform, with the exception that the reflected shock pulse is clipped, and is followed by some high frequency noise The clipping and high frequency noise are due to cavitation occuring at the surface upon reflection of the very high pressure shock pulse

The contamination of the direct path signal by the surface reflection must be removed before further processing of the waveform The method used to remove the surface reflection was suggested by Chapman and developed by Yee, (Yee, 1991) This method was applied by repeatedly adding a time-shifted copy, of the uncontaminated part of the direct path waveform, to the surface reflection The process was iterated until a deconvolved section of the direct path waveform, out to at least the fourth bubble pulse,

was obtained This method provided very good reconstruction of the low frequency components, but did not remove the high frequency noise caused by cavitation Cavitation noise was removed by simply drawing a smooth curve through it Figure 6 4 shows the result of applying the above procedure to the waveform of figure 6 3

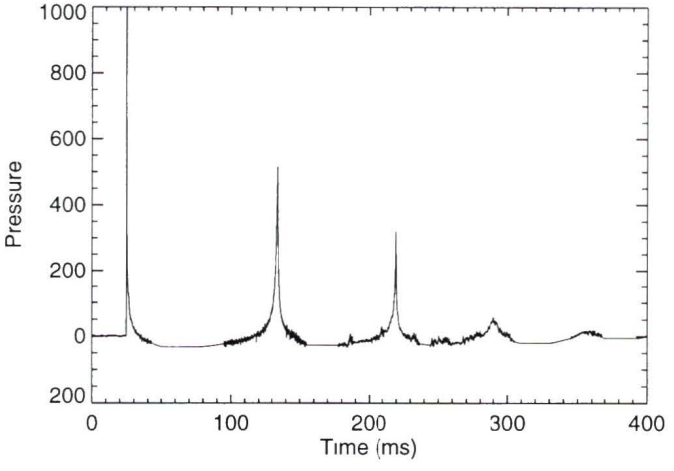

Figure 6 4 Deconvolved Pressure waveform for the 23 m charge

IV. Spectral Analysis

Source levels were calculated from the depth-scaled spectra of the charge waveforms The original spectra were obtained by the following process First, the waveforms were truncated after the fourth or fifth bubble pulse The waveform, beyond the fourth pulse, has relatively low amplitude and does not contribute significant energy, (Yee, 1991) The truncation was exponentially smoothed to zero over 1000 data points, and the resulting waveform was zero padded A 64k fft was applied to each waveform to provide spectra with 0 763 Hz binwidth The spherical spreading loss for each charge to receiver range was accounted for, and the appropriate gains were applied to scale the spectra to cgs energy density units of (dB re erg/cm^2/Hz), referred to 1 m from the source

A. Depth Scaling of Spectra

Figure 6 5 shows the spectrum of a 93 m charge The general spectral shape rises to a maximum at the first bubble pulse frequency for this depth, (≅25 Hz), and decreases with increasing frequency The most notable feature of the spectrum is its modulated shape which is caused by the spiked nature of the waveform The modulation frequency depends mainly on the time separation of the shock and first bubble pulses, but is affected slightly by the second and third bubble pulses at low frequencies The effect of the second and third pulses is seen as the multiple peaks centered around 40 Hz

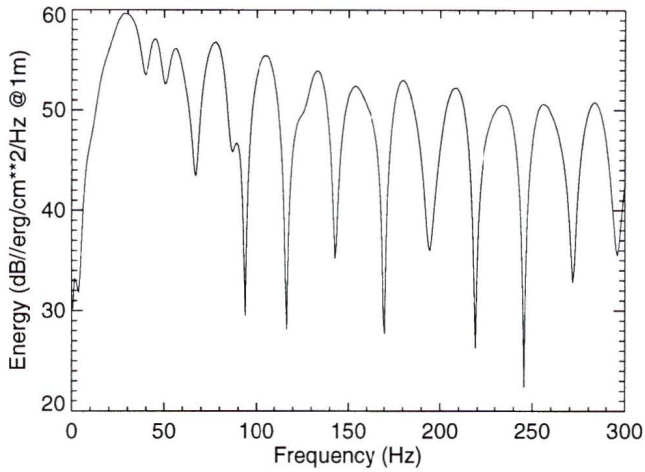

6 5 Spectrum of a 93 m charge

Figure 6 6 shows the spectrum of a 193 m charge We note that the spectral characteristics for the 193 m charge are similar to those of the 93 m charge, except the modulation frequency is greater This effect was expected since the time period between the shock and first bubble periods is smaller for deeper charges Hughes, (Hughes, 1981), noticed that if the frequency scales for the spectra of deeper charges were compressed, and the spectral levels scaled, then the spectra closely matched those for shallower charges He proposed scaling expressions for both frequency (f), and spectral level (S), based on analysis of his own shallow charge data, and deeper charge data, (Christian and Blaik, 1965) The scaling expressions are

$$f = f_o \times (Z / Z_o)^{-0\,55}$$
$$S = S_o \times (Z / Z_o)^{0\,806} \qquad (6\ 2\ a,b)$$

where S_0 is the spectral level at frequency f_0 in the spectrum to be scaled, and Z_0 is the original hydrostatic depth of the charge The scaled spectrum for depth Z is obtained by first scaling the spectral level of the original spectrum using equation 6 2 b, and then scaling the frequency using equation 6 2 a

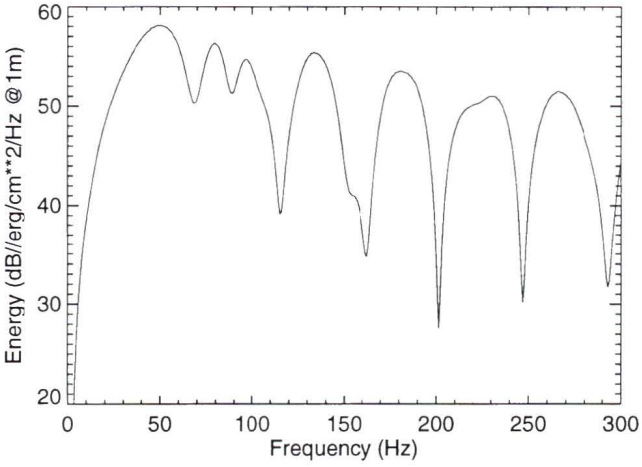

Figure 6 6 Spectrum of a 193 m charge

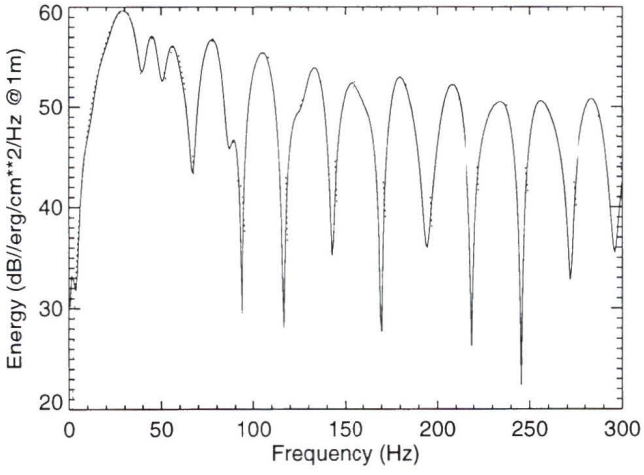

Figure 6 7 Original 93 m spectrum, and 193 m spectrum scaled to 93 m

Figure 6 7 shows the spectrum of the 193 m charge scaled to 93 m, superimposed on the original 93 m spectrum of figure 6 4 It is noted, that even for this relatively large difference in depth, there is good agreement for frequencies below 150 Hz For frequencies greater than 150 Hz, exact agreement is not critical for calculating the 1/3 -

octave band levels since the width of these bands is greater than the modulation period, and the modulation pattern is averaged out Except for the 235 m to 280 m depth range, the scaled depths differed by less than 20% of the depths of the original charges For this relatively small change in depth, the scaling method is expected to be very accurate

B. Source level measurements

Source levels were calculated from the scaled spectra The analysis was carried out on 17 charges detonated at ~20 m, 7 charges at ~50 m, 27 charges at ~100 m, and 34 charges at ~190 m Spectra from charges at each of these approximate depths were scaled to the range of depths close to the depth The depth ranges are 17 m to 27 m in 1 m steps, 40 m to 60 m in 2 m steps, 84 m to 104 m in 2 m steps, and 170 m to 210 m in 4 m steps Additionly, the 34 - 193 m charge spectra were scaled to a range of depths between 230 m and 280 m in 5 m steps Source levels were calculated from the depth-scaled spectra in the consecutive preferred 1/3 octave bands from 5 Hz to 630 Hz using boxcar filters The source levels at each depth were averaged to obtain the results presented in table 6 1 to 6 5

Table 6 1 1/3 Octave source levels for 0 82 kg SUS charges at 17 m to 27 m (dB//erg/cm^2/Hz//1m)

Centre	Charge Depth										
Freq (Hz)	17 m	18 m	19 m	20 m	21 m	22 m	23 m	24 m	25 m	26 m	27 m
5	55 0±1 2	54 9±1 3	54 4±1 5	53 9±1 5	53 6±1 6	53 3±1 7	53 2±1 5	52 9±1 6	52 5±1 8	52 3±1 7	52 2±1 7
6 3	58 8±0 6	58 6±0 6	57 8±0 8	57 0±0 8	56 7±0 7	56 5±0 8	55 8±1 0	55 1±1 2	54 6±1 3	54 3±1 2	54 2±1 3
8	61 5±0 3	61 3±0 4	60 9±0 5	60 5±0 5	60 2±0 5	59 9±0 5	59 5±0 5	59 0±0 5	58 5±0 5	58 2±0 6	57 9±0 6
10	61 9±0 4	62 0±0 4	62 0±0 4	62 0±0 4	61 8±0 4	61 7±0 4	61 5±0 4	61 3±0 4	61 0±0 4	60 8±0 4	60 6±0 4
12 5	58 3±0 6	58 6±0 6	59 0±0 6	59 2±0 5	59 6±0 5	60 0±0 4	60 4±0 5	60 8±0 5	61 1±0 4	61 2±0 4	61 3±0 4
16	57 6±0 3	57 2±0 3	56 7±0 4	56 4±0 5	56 3±0 4	56 2±0 5	56 5±0 6	56 8±0 5	57 3±0 6	57 7±0 5	57 9±0 6
20	55 7±0 2	55 8±0 4	56 3±0 3	57 0±0 4	57 5±0 3	57 8±0 2	57 8±0 4	57 6±0 3	57 3±0 3	56 9±0 3	56 6±0 3
25	56 2±0 3	56 6±0 3	56 5±0 3	56 2±0 2	56 1±0 3	56 1±0 4	56 0±0 4	55 7±0 4	55 3±0 3	55 0±0 3	55 1±0 4
31 5	54 9±0 4	55 2±0 3	55 5±0 4	55 3±0 5	54 6±0 5	53 9±0 4	53 7±0 5	54 2±0 5	55 1±0 4	55 7±0 3	55 9±0 3
40	53 6±0 3	53 7±0 4	53 9±0 4	54 0±0 4	53 8±0 4	53 6±0 3	53 8±0 3	54 0±0 3	54 2±0 3	54 3±0 3	54 5±0 3
50	52 8±0 4	52 3±0 4	52 2±0 5	52 8±0 4	53 7±0 4	53 7±0 4	53 3±0 4	53 1±0 4	53 0±0 3	53 0±0 4	53 1±0 4
63	51 8±0 2	51 9±0 2	52 2±0 3	51 9±0 3	51 7±0 4	52 0±0 4	52 7±0 3	52 8±0 4	52 4±0 4	52 0±0 4	51 6±0 4
80	51 4±0 3	51 1±0 3	51 0±0 3	51 3±0 3	50 9±0 3	51 1±0 3	51 4±0 3	51 5±0 4	51 5±0 3	51 0±0 3	51 2±0 2
100	50 1±0 3	50 1±0 3	50 2±0 3	49 8±0 3	50 3±0 3	50 6±0 3	50 2±0 2	49 8±0 3	50 4±0 2	50 8±0 3	50 4±0 3
125	48 6±0 3	49 3±0 3	48 9±0 3	49 2±0 3	49 1±0 3	49 2±0 3	49 3±0 3	49 2±0 3	49 3±0 3	49 4±0 3	49 4±0 3
160	48 0±0 2	47 8±0 2	48 1±0 2	47 9±0 2	48 2±0 3	48 1±0 2	48 2±0 3	48 4±0 3	48 2±0 3	48 1±0 3	48 6±0 3
200	46 8±0 2	47 0±0 2	46 8±0 2	46 9±0 2	47 2±0 2	47 0±0 2	47 0±0 2	47 2±0 2	47 0±0 2	47 4±0 2	47 1±0 2
250	45 6±0 2	45 7±0 2	45 9±0 2	45 9±0 2	45 8±0 2	46 0±0 2	46 2±0 2	46 1±0 2	46 2±0 2	46 1±0 2	46 3±0 2
315	44 8±0 2	44 8±0 2	44 9±0 2	44 9±0 2	44 9±0 2	44 9±0 2	44 9±0 2	45 0±0 2	45 1±0 2	45 1±0 2	45 0±0 2
400	43 9±0 2	44 0±0 2	44 0±0 2	44 0±0 2	44 0±0 2	44 1±0 2	44 1±0 2	44 0±0 2	44 0±0 2	44 1±0 2	44 1±0 2
500	43 0±0 2	43 0±0 2	43 1±0 2	43 1±0 3	43 2±0 2	43 2±0 2	43 3±0 2	43 3±0 2	43 3±0 2	43 3±0 2	43 3±0 2
630	41 6±0 2	41 7±0 2	41 8±0 2	41 9±0 2	42 0±0 2	42 1±0 2	42 1±0 2	42 2±0 2	42 3±0 2	42 3±0 2	42 4±0 2

Table 6 2 1/3 Octave source levels for 0 82 kg SUS charges at 40 to 60 m (dB//erg/cm^2/Hz//1m)

Centre	Charge Depth										
Freq (Hz)	40 m	42 m	44 m	46 m	48 m	50 m	52 m	54 m	56 m	58 m	60 m
5	48 9±1 8	48 9±1 8	48 5±1 5	48 0±2 1	47 8±2 5	47 3±2 2	47 2±2 2	46 8±2 7	46 3±2 3	46 2±2 3	45 8±1 8
6 3	51 0±0 5	50 9±0 5	50 8±0 8	49 8±1 0	49 6±0 9	49 4±0 7	49 2±1 2	48 5±1 9	48 3±1 8	48 2±1 8	47 9±1 5
8	54 6±1 1	54 5±1 1	53 7±1 2	53 0±1 1	52 7±1 0	51 9±1 0	51 8±1 1	51 3±0 8	50 3±0 5	50 3±0 5	50 1±0 8
10	58 1±0 6	57 8±0 7	57 1±1 0	56 8±0 9	56 5±0 9	55 5±1 0	55 4±1 0	54 7±1 1	53 9±1 1	53 8±1 1	53 1±1 2
12 5	60 1±0 7	59 7±0 5	59 4±0 5	59 0±0 4	58 8±0 4	58 4±0 4	58 1±0 4	57 7±0 6	57 4±0 6	57 2±0 7	56 6±0 8
16	61 6±0 5	61 5±0 6	61 4±0 7	61 1±0 8	60 9±0 8	60 5±0 8	60 1±0 7	59 9±0 8	59 5±0 7	59 2±0 4	58 9±0 5
20	57 2±0 4	57 7±0 6	58 4±0 9	59 3±0 8	59 8±0 6	60 3±0 4	60 7±0 5	60 9±0 5	60 9±0 5	61 0±0 6	60 8±0 7
25	56 7±0 7	56 8±0 9	56 9±0 9	56 9±0 9	56 8±0 9	56 6±0 7	56 5±0 6	56 6±0 6	56 6±0 3	57 0±0 8	57 8±0 9
31 5	55 3±0 9	55 8±1 0	56 1±0 7	56 2±0 7	56 2±0 5	56 1±0 4	56 0±0 5	55 9±0 5	56 0±0 8	56 1±0 9	56 2±1 0
40	56 4±0 4	56 4±0 6	56 2±0 9	55 5±1 0	54 6±0 9	53 9±0 7	54 0±0 9	54 2±1 0	54 6±0 9	55 0±1 0	55 4±0 9
50	54 1±0 9	53 1±1 1	52 0±0 8	52 1±1 1	53 6±0 9	54 8±0 5	55 3±0 3	55 6±0 3	55 7±0 4	55 8±0 6	55 6±0 7
63	52 7±0 4	52 6±0 6	53 1±0 5	53 7±0 3	53 8±0 3	53 9±0 3	54 0±0 3	53 9±0 6	53 5±0 9	52 7±0 9	51 8±0 8
80	51 1±1 3	52 3±0 6	52 8±0 4	52 6±0 5	52 3±0 4	51 9±0 4	51 8±0 5	51 9±0 4	52 0±0 4	51 9±0 4	52 1±0 6
100	51 6±0 7	51 2±0 6	50 5±0 7	50 9±0 7	51 4±0 4	51 6±0 7	51 3±0 8	50 5±0 7	50 4±1 3	51 4±0 7	52 0±0 4
125	49 6±0 6	50 0±0 6	50 5±0 4	50 2±0 6	50 2±0 6	49 7±0 5	49 8±1 0	50 6±0 4	50 9±0 6	50 7±0 7	50 1±0 5
160	49 3±0 6	48 8±0 7	49 1±0 5	49 4±0 5	48 7±1 0	49 3±0 5	49 7±0 6	49 1±0 5	48 9±0 6	49 2±0 7	49 6±0 4
200	47 8±0 5	48 4±0 5	48 0±0 6	48 2±0 4	48 3±0 6	48 3±0 5	48 2±0 6	48 3±0 6	48 6±0 6	48 2±0 7	48 3±0 6
250	47 2±0 5	46 9±0 4	47 2±0 5	47 2±0 4	47 2±0 4	47 4±0 4	47 1±0 5	47 6±0 4	47 2±0 5	47 6±0 5	47 5±0 5
315	45 8±0 5	46 0±0 6	46 2±0 5	46 1±0 5	46 3±0 5	46 0±0 6	46 5±0 4	46 1±0 5	46 5±0 5	46 2±0 4	46 6±0 4
400	45 1±0 5	45 1±0 4	45 1±0 5	45 0±0 5	45 2±0 5	45 3±0 5	45 2±0 5	45 4±0 5	45 2±0 5	45 5±0 5	45 3±0 4
500	44 0±0 4	44 1±0 5	44 1±0 5	44 2±0 5	44 3±0 4	44 3±0 4	44 3±0 4	44 3±0 5	44 4±0 5	44 4±0 4	44 4±0 5
630	42 4±0 5	42 6±0 5	42 8±0 5	42 9±0 5	43 0±0 5	43 1±0 5	43 2±0 5	43 3±0 4	43 4±0 4	43 4±0 4	43 5±0 4

Table 6 3 1/3 Octave source levels for 0 82 kg SUS charges at 84 to 104 m (dB//erg/cm^2/Hz//1m)

Centre	Charge Depth										
Freq (Hz)	84 m	86 m	88 m	90 m	92 m	94 m	96 m	98 m	100 m	102 m	104 m
5	40 7±1 0	40 5±1 0	40 2±0 9	40 0±0 9	39 5±1 1	39 1±1 0	38 9±0 9	38 7±1 0	38 4±1 1	38 3±1 2	37 9±1 0
6 3	43 9±0 6	43 8±0 6	43 4±0 7	43 0±0 7	42 5±0 7	42 3±0 8	42 2±0 8	42 1±0 8	42 0±0 8	41 6±0 8	41 3±0 8
8	46 9±0 4	46 7±0 4	46 4±0 5	46 1±0 3	45 8±0 4	45 5±0 4	45 3±0 4	45 1±0 4	44 9±0 4	44 6±0 5	44 4±0 5
10	49 8±0 3	49 6±0 3	49 3±0 3	49 1±0 2	48 8±0 2	48 5±0 4	48 2±0 4	48 0±0 4	47 8±0 3	47 7±0 2	47 4±0 5
12 5	52 8±0 4	52 6±0 4	52 3±0 4	52 1±0 4	51 8±0 4	51 5±0 4	51 2±0 3	51 1±0 3	50 7±0 4	50 5±0 3	50 3±0 3
16	55 7±0 3	55 5±0 3	55 2±0 4	54 9±0 3	54 8±0 4	54 4±0 4	54 2±0 4	54 0±0 4	53 7±0 4	53 5±0 4	53 3±0 4
20	58 3±0 3	58 1±0 3	57 9±0 3	57 6±0 3	57 4±0 3	57 2±0 3	56 9±0 3	56 7±0 3	56 4±0 3	56 3±0 3	56 0±0 3
25	59 6±0 3	59 6±0 3	59 5±0 3	59 4±0 4	59 3±0 4	59 2±0 4	59 1±0 4	59 0±0 4	58 8±0 3	58 7±0 4	58 5±0 4
31 5	56 6±0 3	56 9±0 3	57 2±0 3	57 6±0 3	57 9±0 3	58 1±0 3	58 4±0 3	58 5±0 3	58 7±0 3	58 8±0 3	58 9±0 3
40	55 7±0 3	55 7±0 3	55 8±0 4	55 7±0 4	55 7±0 4	55 6±0 4	55 4±0 4	55 3±0 4	55 2±0 4	55 1±0 4	55 1±0 4
50	54 5±0 4	54 6±0 3	54 7±0 3	54 8±0 3	54 8±0 3	54 8±0 3	54 9±0 3	54 9±0 3	55 0±0 3	55 0±0 3	55 0±0 3
63	54 3±0 3	53 9±0 3	53 4±0 3	52 8±0 3	52 1±0 4	51 7±0 4	51 4±0 4	51 4±0 3	51 6±0 3	51 9±0 3	52 4±0 3
80	50 1±0 4	50 2±0 4	50 7±0 4	51 5±0 3	52 3±0 3	52 9±0 3	53 4±0 3	53 8±0 3	54 0±0 3	54 1±0 3	54 1±0 3
100	51 7±0 3	51 9±0 3	52 1±0 3	52 2±0 3	52 1±0 3	52 1±0 3	52 2±0 3	52 2±0 3	52 2±0 3	52 0±0 3	51 8±0 4
125	51 3±0 3	51 3±0 3	51 1±0 3	50 8±0 3	50 5±0 3	50 2±0 3	49 9±0 3	49 9±0 3	50 0±0 3	50 2±0 3	50 4±0 3
160	48 7±0 3	48 8±0 3	49 3±0 3	49 8±0 3	50 3±0 3	50 4±0 3	50 3±0 3	49 8±0 3	49 2±0 3	48 7±0 3	48 7±0 3
200	48 8±0 3	48 6±0 3	48 6±0 3	48 6±0 3	48 5±0 3	48 2±0 3	48 1±0 3	48 3±0 3	48 8±0 3	49 2±0 3	49 4±0 3
250	47 5±0 3	48 0±0 3	47 7±0 3	47 2±0 3	47 1±0 3	47 6±0 3	48 0±0 3	48 1±0 3	47 8±0 3	47 5±0 3	47 3±0 3
315	46 1±0 3	46 1±0 3	46 5±0 3	46 6±0 3	46 4±0 3	46 4±0 3	46 4±0 3	46 4±0 3	46 5±0 3	46 8±0 3	47 0±0 3
400	45 4±0 3	45 3±0 3	45 3±0 3	45 3±0 3	45 5±0 3	45 5±0 3	45 2±0 3	45 2±0 3	45 7±0 3	45 8±0 3	45 4±0 3
500	44 3±0 3	44 2±0 3	44 2±0 3	44 3±0 3	44 4±0 3	44 3±0 3	44 3±0 3	44 7±0 3	44 4±0 3	44 3±0 3	44 6±0 3
630	42 6±0 3	42 8±0 3	42 7±0 3	43 0±0 3	42 9±0 3	43 0±0 3	43 1±0 3	43 1±0 3	43 1±0 3	43 4±0 3	43 2±0 3

Table 6 4 1/3 Octave source levels for 0 82 kg SUS charges at 170 to 210 m (dB//erg/cm^2/Hz//1m)

Centre	Source Depth										
Freq (Hz)	170 m	174 m	178 m	182 m	186 m	190 m	194 m	198 m	202 m	206 m	210 m
5	35 0±1 7	34 7±1 7	34 5±1 8	34 3±1 9	34 0±1 9	33 9±1 9	33 7±2 0	33 6±2 0	33 4±2 0	33 3±2 1	33 1±2 1
6 3	37 1±1 3	36 7±1 3	36 4±1 4	36 1±1 5	35 9±1 4	35 9±1 4	35 8±1 4	35 6±1 4	35 4±1 4	35 0±1 6	34 8±1 6
8	39 3±1 0	39 0±1 0	38 8±1 1	38 5±1 1	38 3 1	38 1±1 1	37 9±1 2	37 7±1 2	37 5±1 1	37 3±1 2	37 0±1 2
10	41 8±0 7	41 6±0 7	41 3±0 7	41 1±0 8	40 8±0 8	40 6±0 8	40 3±0 9	40 1±0 9	39 9±0 9	39 7±0 9	39 5±0 9
12 5	44 7±0 4	44 4±0 5	44 1±0 5	43 8±0 5	43 6±0 5	43 4±0 5	43 0±0 5	42 8±0 5	42 6±0 5	42 4±0 5	42 1±0 6
16	47 7±0 4	47 4±0 5	47 1±0 4	46 8±0 5	46 6±0 5	46 4±0 5	46 0±0 5	45 8±0 4	45 5±0 4	45 3±0 4	45 0±0 4
20	50 5±0 5	50 2±0 5	49 9±0 4	49 7±0 5	49 4±0 5	49 2±0 5	48 9±0 5	48 7±0 5	48 5±0 4	48 2±0 5	48 0±0 5
25	53 3±0 5	53 0±0 5	52 7±0 5	52 5±0 5	52 2±0 5	52 0±0 5	51 7±0 5	51 5±0 5	51 2±0 5	51 0±0 5	50 7±0 5
31 5	55 9±0 5	55 7±0 5	55 5±0 5	55 2±0 4	55 0±0 4	54 8±0 5	54 5±0 5	54 3±0 5	54 1±0 4	53 8±0 5	53 6±0 5
40	57 7±0 5	57 6±0 5	57 5±0 4	57 3±0 4	57 2±0 4	57 0±0 5	56 8±0 5	56 6±0 5	56 5±0 4	56 3±0 5	56 1±0 5
50	56 3±0 5	56 6±0 5	56 9±0 5	57 1±0 5	57 2±0 5	57 3±0 5	57 4±0 5	57 4±0 5	57 4±0 5	57 4±0 5	57 4±0 5
63	54 0±0 5	53 6±0 5	53 3±0 5	53 0±0 5	52 8±0 5	52 8±0 5	52 9±0 6	53 2±0 6	53 5±0 6	53 9±0 6	54 3±0 6
80	53 5±0 5	53 8±0 5	53 9±0 5	54 0±0 5	54 1±0 5	54 1±0 5	54 1±0 5	54 1±0 5	54 1±0 5	54 1±0 5	54 1±0 5
100	49 7±0 5	49 3±0 5	49 3±0 5	49 6±0 5	50 2±0 6	50 8±0 5	51 2±0 5	51 6±0 5	51 9±0 5	52 0±0 5	52 2±0 5
125	51 4±0 6	52 0±0 5	52 3±0 5	52 5±0 5	52 6±0 5	52 6±0 5	52 6±0 5	52 4±0 5	52 2±0 5	51 8±0 5	51 3±0 5
160	50 2±0 5	50 2±0 4	50 2±0 4	50 1±0 4	49 8±0 4	49 3±0 4	48 7±0 4	48 2±0 4	47 9±0 4	47 8±0 5	48 1±0 6
200	48 3±0 4	48 0±0 5	48 0±0 5	48 2±0 5	48 5±0 5	48 7±0 5	48 9±0 5	49 1±0 5	49 4±0 5	49 6±0 5	49 7±0 5
250	48 6±0 5	48 4±0 4	47 9±0 4	47 2±0 4	47 0±0 5	47 2±0 6	47 8±0 5	48 2±0 5	48 5±0 5	48 7±0 5	48 7±0 5
315	46 3±0 4	46 3±0 5	46 6±0 5	46 9±0 5	47 2±0 5	47 3±0 4	47 1±0 4	46 7±0 4	46 3±0 4	46 1±0 4	46 2±0 5
400	45 3±0 5	45 8±0 5	46 0±0 5	45 8±0 4	45 5±0 4	45 4±0 5	45 6±0 5	46 0±0 5	46 1±0 5	46 0±0 4	45 8±0 4
500	44 5±0 5	44 5±0 5	44 5±0 5	44 6±0 5	44 9±0 5	45 0±0 5	44 7±0 5	44 4±0 5	44 5±0 6	45 0±0 5	45 3±0 5
630	43 2±0 4	43 0±0 4	43 1±0 5	43 5±0 5	43 5±0 4	43 1±0 5	43 3±0 5	43 7±0 5	43 8±0 5	43 5±0 5	43 5±0 5

Table 6 5 1/3 Octave source levels for 0 82 kg SUS charges at 230 to 280 m (dB//erg/cm^2/Hz//1m)

Centre	Charge Depth										
Freq (Hz)	230 m	235 m	240 m	245 m	250 m	255 m	260 m	265 m	270 m	275 m	280 m
5	32 9±2 2	32 7±2 3	32 5±2 3	32 2±2 4	32 0±2 5	31 8±2 6	31 7±2 6	31 6±2 6	31 6±2 6	31 5±2 6	31 4±2 6
6 3	34 6±1 8	34 4±1 8	34 1±1 9	33 9±1 9	33 6±1 9	33 5±1 9	33 4±2 0	33 3±2 0	33 1±2 0	33 0±2 1	32 7±2 1
8	36 7±1 6	36 4±1 7	36 0±1 7	35 8±1 8	35 7±1 7	35 6±1 7	35 5±1 7	35 3±1 6	35 1±1 6	34 8±1 7	34 5±1 7
10	39 0±1 5	38 7±1 5	38 5±1 5	38 2±1 5	38 0±1 5	37 8±1 6	37 7±1 6	37 5±1 5	37 3±1 5	37 1±1 6	36 8±1 6
12 5	41 5±1 4	41 2±1 4	41 0±1 4	40 7±1 3	40 6±1 4	40 3±1 4	40 1±1 5	39 9±1 4	39 7±1 4	39 5±1 4	39 3±1 4
16	44 4±1 4	44 2±1 4	43 9±1 3	43 6±1 4	43 4±1 3	43 2±1 3	42 9±1 4	42 6±1 3	42 4±1 3	42 2±1 3	41 9±1 3
20	47 4±1 3	47 1±1 3	46 8±1 3	46 5±1 3	46 4±1 3	46 1±1 3	45 8±1 4	45 6±1 3	45 4±1 3	45 1±1 3	44 9±1 3
25	50 2±1 3	49 9±1 3	49 7±1 3	49 4±1 3	49 2±1 3	48 9±1 3	48 7±1 3	48 5±1 3	48 3±1 2	48 0±1 3	47 8±1 2
31 5	53 0±1 2	52 7±1 3	52 4±1 3	52 2±1 3	51 9±1 3	51 7±1 3	51 5±1 3	51 3±1 3	51 0±1 3	50 8±1 3	50 6±1 3
40	55 5±1 0	55 3±1 0	55 0±1 0	54 8±1 1	54 6±1 1	54 4±1 1	54 2±1 1	54 0±1 2	53 8±1 2	53 6±1 2	53 4±1 2
50	57 0±0 5	56 9±0 5	56 8±0 5	56 6±0 5	56 5±0 5	56 4±0 5	56 2±0 6	56 1±0 6	56 0±0 7	55 8±0 7	55 6±0 8
63	55 7±0 7	55 9±0 7	56 1±0 8	56 2±0 8	56 3±0 8	56 4±0 9	56 5±0 9	56 5±0 8	56 5±0 8	56 5±0 8	56 5±0 7
80	53 2±0 5	52 9±0 5	52 6±0 6	52 4±0 7	52 3±0 7	52 4±0 8	52 5±0 7	52 7±0 7	53 0±0 6	53 3±0 6	53 7±0 6
100	52 8±0 8	52 9±0 8	53 1±0 9	53 2±0 8	53 2±0 8	53 3±0 8	53 3±0 7	53 3±0 7	53 3±0 6	53 3±0 6	53 3±0 6
125	49 0±0 8	49 0±1 1	49 1±1 2	49 6±1 1	50 0±1 0	50 5±0 9	50 9±0 8	51 1±0 7	51 3±0 6	51 5±0 5	51 5±0 5
160	51 0±0 6	51 4±0 6	51 6±0 6	51 8±0 6	51 8±0 7	51 8±0 7	51 7±0 7	51 5±0 8	51 3±0 8	50 9±0 8	50 5±0 8
200	49 5±0 5	49 5±0 6	49 4±0 6	49 3±0 5	49 0±0 5	48 5±0 4	48 1±0 5	47 6±0 6	47 4±0 7	47 4±0 8	47 7±0 8
250	47 6±0 5	47 5±0 6	47 5±0 5	47 7±0 5	47 8±0 6	48 0±0 6	48 2±0 6	48 5±0 6	48 7±0 5	48 9±0 5	49 0±0 5
315	47 8±0 6	47 5±0 5	46 9±0 4	46 4±0 4	46 4±0 5	46 7±0 6	47 2±0 5	47 6±0 5	47 8±0 6	47 9±0 6	47 9±0 6
400	45 6±0 5	45 7±0 5	46 0±0 5	46 4±0 5	46 6±0 5	46 6±0 5	46 3±0 5	46 0±0 4	45 6±0 4	45 5±0 5	45 6±0 5
500	44 9±0 5	45 2±0 5	45 2±0 5	45 0±0 5	44 8±0 5	44 8±0 5	45 0±0 5	45 3±0 5	45 3±0 5	45 2±0 5	45 2±0 4
630	43 8±0 5	43 8±0 5	43 8±0 6	44 0±0 6	44 2±0 5	44 2±0 5	43 9±0 5	43 7±0 5	43 8±0 6	44 3±0 6	44 5±0 6

The uncertainties given in tables 6 1 to 6 5 are the standard deviations of the levels used for each average We note that averaging was performed on source levels in linear units The standard deviations, also in linear units, were added to the averages and the sums were converted to decibels The uncertainties listed are the differences between the sums and the averages in decibels

C. Ceptsrum technique for depth measurement

The modulation of the source spectra can be exploited to provide a convenient method for measuring source depths As mentioned previously, the frequency period of modulation is the first bubble pulse frequency, which is a function of depth according to equation 6 1 The modulation period is easily determined by taking the spectrum of the energy spectrum The secondary spectrum is referred to as the CEPSTRUM A fairly reliable peak in the CEPSTRUM occurs at the time delay representing the bubble pulse period

V. Comparison with accepted levels

Because the previously published 1/3 octave band source levels are for specific depths, we will restrict comparison of our results to the accepted levels of Chapman, (Chapman, 1988), at the specific depths 23 5 m, 99 6 m, 194 4 m, and 244 m The present results at these depths are consistent with Chapman's levels within the uncertainties except for the 5, 6 3, and 8 Hz bands These mismatches are probably due to a small difference between our 1/3 octave band edges and those used by Chapman Band edges for the present work were determined according to $10^{n/10\pm0\ 05}$ where, for example, n = 9 for the 8 Hz band Additionally, the low frequency levels do not match well at the shallow 23 5 m depth This mismatch is very likely due to the different methods used for deconvolving the surface reflection in the shallow charge waveforms The method used for the present work is superior for reconstructing the low frequency components

Appendix B

Calculation of the Reflection Coefficient for Plane Acoustic Waves Incident from a Fluid onto a Solid Layered Substrate

I. Introduction

The reflection coefficient for plane acoustic waves, incident from a semi-infinite fluid layer onto a layered solid substrate, is dependent upon the frequency of the incident wave and the angle of incidence at the fluid-solid interface The reflection coefficient is also dependent upon the elastic properties of the fluid and all layers in the solid substrate, as well as the layer thicknesses The derivation of a closed form expression for the reflection coefficient at an interface separating two semi-infinite layers is relatively straight-forward *e g* (Brekhovskikh, 1980) It is significantly more complicated, however, to obtain a closed form expression for the reflection coefficient when there is more than one layer in the solid substrate In this appendix, a method for calculating the multi-layer reflection coefficient is described This method, which was outlined by Brekhovskikh, takes advantage of the relationships between the amplitudes of waves in adjacent layers Brekhovskikh's outline, however, contains several errors and therefore requires time-consuming derivations before it can be implemented These errors are corrected in the following description, which also shows how to include both compressional and shear wave attenuation for all solid layers into the method Additionally, the FORTRAN source code for a subroutine which implements the method for the case of a fluid layer overlying two homogeneous solid layers is included

II. Mathematical Formulation

The wave equation describes how disturbances propagate in linear media The disturbance of interest when considering elastic waves is the particle displacement It is assumed that the media are linear in the sense that the restoring force acting on displaced particles is directly proportional to, and in the opposite direction of the displacement

Also, in order to simplify the development of solutions, the time dependence of the particle displacement will be assumed to be harmonic with angular frequency ω Arbitrary time dependencies can be considered using Fourier superposition of the solutions for harmonic cases The particle displacement, $\mathbf{U}(x,y,z,t)$ will thus be written, $\mathbf{U} = \mathbf{u}(x,y,z)*\exp(i\omega t)$ The wave equation for particle displacement not in the vicinity of sources is,

$$\nabla^2\mathbf{U} - \frac{1}{c^2}\frac{\partial^2\mathbf{U}}{\partial t^2} = 0 \qquad (7\ 1a)$$

or equivalently

$$\nabla^2\mathbf{u} + k^2\mathbf{u} = 0 \qquad (7\ 1b)$$

where c is the speed of propagation of the disturbance in the medium and $k=\omega/c$ is the wave number Equation 7 1b is often referred to as the time reduced wave equation or the Helmholtz equation It is useful to define **u** in terms of a scalar potential ϕ, and a vector potential **Ψ,**

$$\mathbf{u} = \nabla\phi + \nabla\times\Psi \qquad (7\ 2)$$

This representation is chosen to account for the observation that, in solid media, there are two distinct types of propagating elastic waves These waves are characterized by the direction of particle motion relative to the direction of propagation In the literature concerning propagation in solid elastic media, waves with particle displacement parallel to the direction of propagation are referred to as longitudinal or compressional waves Waves with particle displacement perpendicular to the direction of propagation are referred to as transverse or shear waves The gradient of potential ϕ represents particle displacement due to compressional waves The curl of vector potential **Ψ** introduces particle displacement resulting from shear waves

If only plane waves originating in a fluid half-space are considered, a coordinate system can be oriented so that the direction of propagation lies in the (x,z) plane as shown in figure 7 1

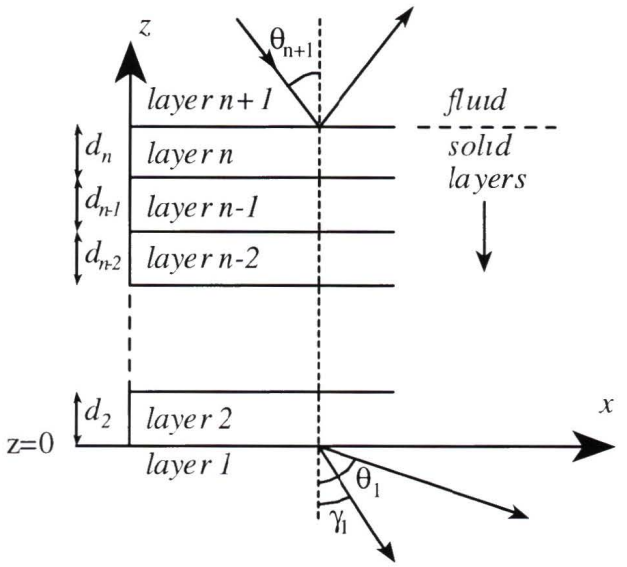

Figure 7 1 Geometry of fluid and n solid layers

For this case, all particle motion in the fluid also occurs in the (x,z) plane because only compressional waves can exist in the fluid It follows that particle displacements in the y direction are zero for all layers if the interfaces are perfectly flat and horizontal Because of the restriction of displacement to the (x,z) plane, all shear waves are vertically polarized It is apparent from equation 7 2, that to have vertically polarized shear waves requires the r and z components of the vector potential $\boldsymbol{\Psi}$ to be 0 The vector potential can thus be written, $\boldsymbol{\Psi}=\psi\hat{\mathbf{y}}$, where ψ is a scalar function In the following,ψ will be treated as the scalar potential for shear waves Within each layer, the scalar potentials ϕ and ψ satisfy the independent Helmholtz equations

$$\nabla^2\phi + k^2\phi = 0, \qquad k = \omega / c \tag{7 3a}$$

$$\nabla^2\psi + \kappa^2\psi = 0, \qquad \kappa = \omega / b \tag{7 3b}$$

Where c and b are the speeds of propagation for compressional and shear waves respectively These equations are connected through the boundary conditions at the layer interfaces Now using equation 7 2 and the fact that $\boldsymbol{\Psi}=\psi\hat{\mathbf{y}}$, particle displacements are,

$$u_x = \frac{\partial\phi}{\partial x} - \frac{\partial\psi}{\partial z}, \qquad u_y = 0, \qquad u_z = \frac{\partial\phi}{\partial z} + \frac{\partial\psi}{\partial x} \tag{7 4}$$

A rigorous treatment of the elastic properties of solids, (Pilant, 1979), shows that, when homogeneity in all layers is present, the z and x components of the stress tensor on a horizontal plane can be written,

$$T_{zz} = \lambda\left(\frac{\partial u_x}{\partial x} + \frac{\partial u_z}{\partial z}\right) + 2\mu\frac{\partial u_z}{\partial z}, \qquad T_{zx} = \mu\left(\frac{\partial u_x}{\partial z} + \frac{\partial u_z}{\partial x}\right) \tag{7 5}$$

where λ and μ are the Lamé constants for the layer The Lamé constants can be written in terms of the density ρ, and the compressional and shear wave speeds c and b as $\lambda = \rho(c^2 - 2b^2)$ and $\mu = \rho b^2$ The horizontal component of all wave vectors (compressional and shear), in all layers is $\xi = k \sin\theta = \kappa \sin\gamma$ This value is constant for a wave of specific frequency and angle of incidence from the fluid This is a consequence of Snell's law In fact, the x dependence of all compressional and shear waves can be written $e^{i\xi x}$ Because this dependence is common to all potentials, it will be omitted in the following expressions The dependence however allows us to replace all derivatives of the potentials with respect to x by $i\xi$ Using this and the expressions for the Lamé constants, the stress components in 7 5 can be rewritten with the z subscript omitted,

$$T_z = \rho\kappa^{-2}\left(\frac{\partial\psi}{\partial z} - ip\phi\right), \qquad T_x = \rho\kappa^{-2}\left(\frac{\partial\phi}{\partial z} + ip\psi\right), \tag{7 6}$$

where $p = [\,\xi^2 - (\kappa^2/2)]\xi^{1}$

Boundary conditions to be satisfied on the interfaces between the elastic layers are,

1 The x and z stress components must be continuous across the interface

2 Particle displacement must be continuous across the interface

These conditions may be written using the notation of Brekhovskikh,

$$[T_z] = 0, \quad [T_x] = 0, \quad [u_x] = 0, \quad [u_z] = 0 \tag{7 7}$$

where the square brackets represent the change of the value across an interface The four conditions in 7 7 are rewritten in 7 8 using the expressions for the stress components in 7 6 and the particle displacements in 7 4,

$$\left[\rho\kappa^{-2}\left(\frac{\partial\psi}{\partial z}-\imath p\phi\right)\right]=0, \qquad \left[\rho\kappa^{-2}\left(\frac{\partial\phi}{\partial z}+\imath p\psi\right)\right]=0 \tag{7 8 a,b}$$

$$\left[\frac{\partial\psi}{\partial z}-\imath\xi\phi\right]=0, \qquad \left[\frac{\partial\phi}{\partial z}+\imath\xi\psi\right]=0 \tag{7 8 c,d}$$

At the fluid-solid interface, condition 7 8c which represents continuity of u_x does not hold because the fluid particles are free to slide along the surface of the solid

We now have general equations for the shear and compressional waves in each layer, and boundary conditions at the layer interfaces These equations are required for calculating reflection and transmission coefficients for a system of 2 or more layers

III. Direct calculation of the reflection coefficient

We proceed by considering the geometry and coordinate system shown in figure 7 1, which consists of a fluid half-space layer overlying n solid layers The bottom solid layer is numbered 1 and is a half-space The z axis points upward with z=0 at the interface between layers 1 and 2 Quantities associated with a particular layer are distinguished by their subscripts Using this notation, $k_{n+1}=\omega/c_{n+1}$ is the wave number in the fluid Also $k_n=\omega/c_n$ and $\kappa_n=\omega/b_n$ are the compressional and shear wave numbers in the top solid layer The layers have thicknesses d_j, j=2 n

The potentials ϕ and ψ in each layer are split into upward and downward traveling plane waves Note the x dependence has been omitted

$$\phi_j=\phi'_j e^{\imath\alpha_j z}+\phi''_j e^{-\imath\alpha_j z}, \qquad \alpha_j=\left(k_j{}^2-\xi^2\right)^{1/2} \tag{7 9}$$

$$\psi_j=\psi'_j e^{\imath\beta_j z}+\psi''_j e^{-\imath\beta_j z}, \qquad \beta_j=\left(\kappa_j{}^2-\xi^2\right)^{1/2}$$

$$j=1 \quad n+1$$

Here α_j, and β_j are the vertical components of the wave vectors for compressional and shear waves in layer j These values are easily calculated, using Snell's law to obtain the directions of the wave vectors, and using the wave speeds to obtain their magnitudes Because we do not have upward traveling waves incident from layer 1, $\phi'_1 = \psi'_1 = 0$ Also, because shear waves are not supported in the fluid layer, $\psi'_{n+1} = 0$ and $\psi''_{n+1} = 0$

The reflection coefficient at the fluid-solid interface is simply the ratio of the reflected wave to the incident wave, $\phi'_{n+1} / \phi''_{n+1}$ The direct method for calculating the reflection coefficient is to make ϕ''_{n+1} a unit amplitude wave and then to solve the system of equations 7 9 to obtain ϕ'_{n+1} The equations 7 9 can be solved directly using the boundary conditions specified in equations 7 8 The boundary conditions are applied at the interfaces, where $z = (0,\ d_2,\ d_2+d_3,\ d_2+d_3+d_4,\ )$ When applying these boundary conditions, it is worthwhile to consider the x and z dependence of ϕ and ψ We recall the x dependence is simply $e^{i\xi x}$ for both potentials in any layer The z dependence is $e^{\pm i\alpha_j z}$ or $e^{\pm i\beta_j z}$, with the sign of the exponent depending on the vertical direction of the wave in the layer These relationships make the application of the x and z derivatives straight-forward in the boundary conditions 7 8

Even for a small number of layers, the above method for obtaining the reflection coefficient becomes tedious due to the large number of equations and boundary conditions In the following section, a method which takes advantage of the relationships between the amplitudes of waves in adjacent layers is investigated

IV. Brekhovskikh's method

We start by considering solid layer n The origin of the z axis is temporarily placed at the lower boundary of this layer The thickness of this layer is d The compressional and shear potentials in the layer are written

$$\phi_n = \phi'_n e^{i\alpha_n z} + \phi''_n e^{-i\alpha_n z}, \qquad \alpha_n = \left(k_n^{\,2} - \xi^2\right)^{1/2} \tag{7 10}$$

$$\psi_n = \psi'_n e^{i\beta_n z} + \psi''_n e^{-i\beta_n z}, \quad \beta_n = \left(\kappa_n^{\,2} - \xi^2\right)^{1/2}$$

The components of particle displacement, u_{xn} and u_{zn} are obtained from equations 1 4 The components of the stress tensor, T_{zn} and T_{xn} are obtained from equations 7 5 We

want specific expressions for these four quantities at the upper boundary of the layer ($z = d$) Substituting the expressions 7 10 for ϕ_n and ψ'_n into the equation for u_x in 7 4, and expanding the complex exponentials into their cosine and sine components we get

$$u_{x_n} = \iota\xi(\phi'_n + \phi''_n)\cos P - \xi(\phi'_n - \phi''_n)\sin P - \iota\beta(\psi'_n - \psi''_n)\cos Q + \beta(\psi'_n + \psi''_n)\sin Q, \quad (7\ 11)$$

where $P=\alpha d$ and $Q=\beta d$ The remainder of the expressions u_{z_n}, T_{z_n}, T_{x_n} have very similar forms to 7 11 The only differences are that the coefficients of $(\phi'_n+\phi''_n)$, $(\phi'_n-\phi''_n)$, $(\psi'_n-\psi''_n)$, and $(\psi'_n+\psi''_n)$ are different Equation 7 11 as well as the quantities u_{z_n}, T_{z_n}, T_{x_n} can thus be conveniently written in the matrix form shown in equation 7 12,

$$\begin{bmatrix} u_{x_n} \\ u_{z_n} \\ T_{z_n} \\ T_{x_n} \end{bmatrix} = \begin{bmatrix} \iota\xi\cos P & -\xi\sin P & -\iota\beta\cos Q & \beta\sin Q \\ -\alpha\sin P & \iota\alpha\cos P & -\xi\sin Q & \iota\xi\cos Q \\ -(\lambda k^2 + 2\mu\alpha^2)\cos P & -\iota(\lambda k^2 + 2\mu\alpha^2)\sin P & -2\mu\xi\beta\cos Q & -2\iota\mu\xi\beta\sin Q \\ -2\iota\mu\alpha\xi\sin P & -2\mu\alpha\xi\cos P & \iota\mu(\beta^2 - \xi^2)\sin Q & \mu(\beta^2 - \xi^2)\cos Q \end{bmatrix} \begin{bmatrix} \phi'_n + \phi''_n \\ \phi'_n - \phi''_n \\ \psi'_n - \psi''_n \\ \psi'_n + \psi'' \end{bmatrix} \quad (7\ 12)$$

We now regard the lower boundary of the layer (n) which we have been considering This is the interface where we have chosen $z = 0$, so $P = Q = 0$ Expression 7 12 can be used again to obtain the particle displacements and the stress components at this lower boundary Now we make use of the fact that the displacements and stresses are continuous across the lower boundary The quantities at the lower boundary of layer n are therefore equal to the respective quantities at the upper boundary of layer n-1 We then express 7 12 at the lower boundary in 7 13,

$$\begin{bmatrix} u_{x(n-1)} \\ u_{z(n-1)} \\ T_{z(n-1)} \\ T_{x(n-1)} \end{bmatrix} = \begin{bmatrix} \iota\xi & 0 & -\iota\beta & 0 \\ 0 & -\iota\alpha & 0 & \iota\xi \\ -(\lambda k^2 + 2\mu\alpha^2) & 0 & -2\mu\xi\beta & 0 \\ 0 & -2\mu\alpha\xi & 0 & \mu(\beta^2 - \xi^2) \end{bmatrix} \begin{bmatrix} \phi'_n + \phi''_n \\ \phi'_n - \phi''_n \\ \psi'_n - \psi''_n \\ \psi'_n + \psi'' \end{bmatrix} \quad (7\ 13)$$

The center matrix in equation 7 13 may be inverted and the result multiplied from the left through the equation to express the rightmost matrix, which is also present in equation 7 12, in terms of the displacements and stresses at the upper boundary of layer n-1 The resulting expression for the rightmost matrix in equation 7 13 is then entered into equation 7 12 to obtain matrix equation 7 14

$$\begin{bmatrix} u_{x_n} \\ u_{z_n} \\ T_{z_n} \\ T_{x_n} \end{bmatrix} = \begin{bmatrix} a_{11} & a_{12} & a_{13} & a_{14} \\ a_{21} & a_{22} & a_{23} & a_{24} \\ a_{31} & a_{32} & a_{33} & a_{34} \\ a_{41} & a_{42} & a_{43} & a_{44} \end{bmatrix} \begin{bmatrix} u_{x(n-1)} \\ u_{z(n-1)} \\ T_{z(n-1)} \\ T_{x(n-1)} \end{bmatrix} \tag{7 14}$$

where the elements a_{ij}, (i , j = 1 4) are listed in equations 7 15

(7 15)

$$\begin{aligned}
a_{11} &= 2\sin^2\gamma\cos P + \cos 2\gamma\cos Q, \\
a_{12} &= \iota(\tan\theta\cos 2\gamma\sin P - \sin 2\gamma\sin Q), \\
a_{13} &= \iota\sin\theta(\cos Q - \cos P)/\omega\rho c, \\
a_{14} &= (\tan\theta\sin\gamma\sin P + \cos\gamma\sin Q)/\omega\rho b, \\
a_{21} &= \iota b^2(c^{-2}\sin 2\theta\sin P - b^{-2}\cos 2\gamma\tan\gamma\sin Q), \\
a_{22} &= \cos 2\gamma\cos P + 2\sin^2\gamma\cos Q, \\
a_{23} &= (\cos\theta\sin P + \tan\gamma\sin\theta\sin Q)/\omega\rho c, \\
a_{24} &= a_{13}, \\
a_{31} &= -2\iota\omega\rho b\sin\gamma\cos 2\gamma(\cos Q - \cos P), \\
a_{32} &= -\omega\rho\left[(c\cos^2 2\gamma/\cos\theta)\sin P + 4b\cos\gamma\sin^2\gamma\sin Q\right], \\
a_{33} &= a_{22} \\
a_{34} &= a_{12}, \\
a_{41} &= -\omega\rho b^2\left[4c^{-1}\cos\theta\sin^2\gamma\sin P + b^{-1}\sin Q\cos^2 2\gamma/\cos\gamma\right], \\
a_{42} &= a_{31}, \\
a_{43} &= a_{21}, \\
a_{44} &= a_{11}
\end{aligned}$$

The components of the wave vectors ξ, α, and β which occur in equations 7 13 and 7 14 have been written in terms of their wave vector magnitudes, (ω/c or ω/b) and their wave vector angles, (θ or γ) in equations 7 15 The Lame constants λ and μ also present in 7 13 and 7 14 have been written in terms of the density ρ, and the wave speeds c or b, in equations 7 15 Note that all values in equations 7 15 are associated with the layer n for the case being considered so far We can now move our coordinate system down one layer so that $z = 0$ corresponds with the interface between layers n-1 and n-2 The identical reasoning which lead to equations 7 14 and 7 15 can be applied again to

obtain the same relationships of particle velocity and stress components between layers n-1 and n-2 In this case however, the constants a_{11} to a_{44} in equation 7 15 are obtained using values associated with layer n-1

This procedure is applied iteratively from layer n down to layer 2 so that the particle displacements and stress components in layer n are expressed in terms of the respective values in layer 1 This result is written in the form 7 16

$$\begin{bmatrix} u_{x_n} \\ u_{z_n} \\ T_{z_n} \\ T_{x_n} \end{bmatrix} = \begin{bmatrix} A_{11} & A_{12} & A_{13} & A_{14} \\ A_{21} & A_{22} & A_{23} & A_{24} \\ A_{31} & A_{32} & A_{33} & A_{34} \\ A_{41} & A_{42} & A_{43} & A_{44} \end{bmatrix} \begin{bmatrix} u_{x1} \\ u_{z1} \\ T_{z1} \\ T_{x1} \end{bmatrix} \tag{7 16}$$

where the matrix **A** is the product of n-1 matrices, each of the form of matrix ***a*** in equation 7 14 Thus $\mathbf{A} = \mathbf{a}^{(n)}\ \mathbf{a}^{(n-1)}\ \ \mathbf{a}^{(3)}\ \mathbf{a}^{(2)}$ Where $\mathbf{a}^{(n)}$ is the matrix relating layers n and n-1 The individual elements of **A** are written out in equation 7 16 only for reference because they will be used separately in following equations

We proceed by returning to the coordinate system shown in figure 7 11, in which the origin is placed on the interface between layers 1 and 2 The interface between the top solid layer n and the fluid layer n+1 is then at $z = H$ where $H = d_2 + d_3 + \ + d_n$ The downward traveling wave in the fluid (the incident wave) is given amplitude 1 and is assumed to have zero phase The upward traveling wave in the fluid is the reflected wave It has amplitude V which may be complex, indicating non-zero phase change The total potential field in the fluid layer can then be written

$$\phi_{n+1} = e^{-i\alpha_{n+1}(z-H)} + Ve^{i\alpha_{n+1}(z-H)}, \tag{7 17}$$

The z particle displacement and z stress component in the fluid on the boundary are obtained from 7 17 using equations 7 4 and 7 6,

$$z = 0 \qquad u_{z(n+1)} = i\alpha_{n+1}(V-1), \qquad T_{z(n+1)} = -\omega^2\rho_{n+1}(V-1), \tag{7 18}$$

Combining equations 7 18, we can write the reflection coefficient V in the form,

$$V = (Z_{1n} - Z_{n+1})/(Z_{1n} + Z_{n+1}) \tag{7 19}$$

where $$Z_{in} = \frac{\imath T_{z(n+1)}}{\omega u_{z(n+1)}}, \qquad Z_{n+1} = \frac{\rho_{n+1} c_{n+1}}{\cos\theta_{n+1}} \tag{7 20}$$

Note that equation 7 19 is of the form of the reflection coefficient commonly arising in transmission line theory Continuing this analogy, Z_{in} is called the input impedance to the set of layers, and Z_{n+1} is the characteristic impedance of the fluid to the wave We still do not have a closed form expression for the input impedance, for which we require the z particle displacement and the z component of stress at the fluid-solid interface In order to find these values, we have to consider the field in the bottom layer 1 In layer 1, which is a solid half-space, no upward traveling waves are expected The field in this layer is thus written,

$$\phi_1 = We^{-\imath\alpha_1 z}, \qquad \psi_1 = Xe^{-\imath\beta_1 z} \tag{7 21}$$

Notice, in this expression, that the coefficients W and X are the transmission coefficients for compressional and shear wave potentials The particle displacements and stress components at the top of layer 1 are obtained from 7 21, by again using equations 7 4 and 7 6,

$z = H$ $$u_{z_1} = \imath(-\alpha_1 W + \xi X), \quad u_{x_1} = \imath(\xi W + \kappa_1 X \cos\gamma_1), \tag{7 22 a,b,}$$

$$T_{z_1} = -\omega^2 \rho_1 \left[\cos 2\gamma_1 W - \sin 2\gamma_1 X\right], \tag{7 22 c}$$

$$T_{x_1} = \omega^2 \rho_1 \left[\cos 2\gamma_1 X + (b_1^2 / c_1^2)\sin 2\theta_1 W\right], \tag{7 22 d}$$

The boundary conditions at $z = H$ state that,

$$u_{z(n+1)} = u_{z_n}, \quad T_{z(n+1)} = T_{z_n}, \quad T_{x(n+1)} = T_{x_n} = 0, \tag{7 23}$$

We now make use of these relationships between particle displacements and stress components at the fluid-solid interface ($z = H$), and the same values at the interface above layer 1 ($z = 0$) This relationship was given in matrix equation 7 16 Multiplying out the terms of interest, we get

$$
\begin{aligned}
u_{z(n+1)} &= A_{21}u_{x_1} + A_{22}u_{z_1} + A_{23}T_{z_1} + A_{24}T_{x_1}, \\
T_{z(n+1)} &= A_{31}u_{x_1} + A_{32}u_{z_1} + A_{33}T_{z_1} + A_{34}T_{x_1}, \\
0 &= A_{41}u_{x_1} + A_{42}u_{z_1} + A_{43}T_{z_1} + A_{44}T_{x_1}
\end{aligned}
\tag{7 24}
$$

where the terms for layer n+1 are taken at $z = H$, and the terms for layer 1 are taken at $z = 0$ The third equation in 7 24 is solved for u_{x_1} and this value is put into the first and second equations These first two equations can then be written,

$$
\begin{aligned}
u_{z(n+1)} &= M_{22}u_{z_1} + M_{23}T_{z_1} + M_{24}T_{x_1}, \\
T_{z(n+1)} &= M_{32}u_{z_1} + M_{33}T_{z_1} + M_{34}T_{x_1}
\end{aligned}
\tag{7 25}
$$

where
$$M_{ij} = A_{ij} - A_{i1}A_{4j} / A_{41} \tag{7 26}$$

We now substitute the values of u_{z1}, T_{z1} and T_{x1} from equations 7 22 a,c,d into equations 7 25 and multiply the results by i/W to obtain the expressions $A = iT_{z(n+1)}/W$ and $B = iu_{z(n+1)}/W$

$$
\begin{aligned}
A = {} & \alpha_1 M_{32} - i\omega^2\rho_1\left[\cos 2\gamma_1 M_{33} - (b_1^2 / c_1^2)\sin 2\theta_1 M_{34}\right] \\
& -\left[\xi M_{32} - i\omega^2\rho_1(\sin 2\gamma_1 M_{33} + \cos 2\gamma_1 M_{34})\right]X / W
\end{aligned}
\tag{7 27}
$$

$$
\begin{aligned}
B = {} & \alpha_1 M_{22} - i\omega^2\rho_1\left[\cos 2\gamma_1 M_{23} - (b_1^2 / c_1^2)\sin 2\theta_1 M_{24}\right] \\
& -\left[\xi M_{22} - i\omega^2\rho_1(\sin 2\gamma_1 M_{23} + \cos 2\gamma_1 M_{24})\right]X / W
\end{aligned}
\tag{7 28}
$$

The ratio $T_{z(n+1)}/u_{z(n+1)}$ is required in equation 7 20 for the input impedance to the system of layers Note since $A/B = T_{z(n+1)}/u_{z(n+1)}$, that ratio can be substituted

We still are not quite finished The ratio X/W which occurs in equations 7 27 and 7 28 may be determined by substituting all four expressions from equations 7 22 into the third equation in 7 24 The resulting ratio is,

$$
\frac{X}{W} = -\frac{\xi A_{41} + \alpha_1 A_{42} + i\omega^2\rho_1 \cos 2\gamma_1 A_{43} - i\omega^2\rho_1 (b_1^2 / c_1^2)\sin 2\theta_1 A_{44}}{\kappa_1 \cos\gamma_1 A_{41} + \xi A_{42} - i\omega^2\rho_1 \sin 2\gamma_1 A_{43} - i\omega^2\rho_1 \cos 2\gamma_1 A_{44}}
\tag{7 29}
$$

The problem is thus solved In order to obtain the reflection coefficient, we first calculate the wave numbers and angles for both shear and compressional waves in all layers using Snell's law and the wave speeds We then construct the matrices **a** whose

components are given in equation 7 15 for each layer The matrix **A** is then calculated as the product of all matrices **a** as is shown in the second line following equation 7 16 The elements of **A** are used to obtain the elements M_{ij} using equation 7 26 The elements of **A** are also used to obtain the ratio *X/W* in equation 7 20 This ratio is used in equations 7 27 and 7 28 to get values for *A* and *B* The ratio *A/B* is equal to the ratio $T_{z(n+1)}/u_{z(n+1)}$ which is required in equation 7 20 to obtain the input impedance Z_{in} to the system of solid layers Finally the reflection coefficient is calculated from equation 7 19

V. Attenuation Coefficients

Although not explicitly shown, attenuation of both compressional and shear waves can be accounted for easily using the above method Attenuation in the layers arises when the Lamé constants are complex This leads to complex sound speeds (*c* and *b*) and wave numbers (*k* and κ) for compressional and shear waves respectively The imaginary components of the wave numbers introduce real spatial decay in the complex exponentials present in the potential expressions We therefore introduce attenuation by first calculating the real parts of the wave numbers for each layer as $k_r = \omega/c$ and $\kappa_r = \omega/b$, where *c* and *b* are the ordinary (real) sound speeds for the layer The imaginary parts of the wave numbers are calculated based on the value of the attenuation coefficient If the attenuation coefficients (α_p and α_s) are given in units of dB/λ, then $k_i = k_r * \alpha_p / [2\pi*20\log(e)]$, and $\kappa_i = \kappa_r * \alpha_s / [2\pi*20\log(e)]$ Finally, we recalculate complex sound speeds based on the complex wave numbers $c = \omega/k$ and $b = \omega/\kappa$

VI. Reflection Loss Subroutine

The following subroutine calculates the reflection loss in a specified frequency band for a plane acoustic wave signal incident from a fluid onto a two homogeneous layer solid substrate It assumes that the incident wave power specturm is constant over the frequency band The loss is calculated as the average square modulus of the complex reflection coefficient at a specified number of equi-spaced frequencies within the band This subroutine was used for modeling the reflection loss for acoustic energy incident from water onto the sediment / basalt ocean bottom Variables and equations are named as closely as possible to the scheme used by Brekhovskikh

```
C**********************************************************************
C**                  SUBROUTINE BY DAVID HANNAY                       **
C**                     VERSION 1  APRIL, 1993                        **
C**********************************************************************

C*****************************************************************
C This program calculates the plane wave reflection loss
C for waves incident from a fluid on to a layered solid substrate
c The method used is outlined in "Waves in Layered Media", 2nd
c Edition, by Brekhovskikh  This program first calculates the reflection
C coefficent for the specific case of a solid sediment layer
c overlying an infinite solid halfspace basement layer   For this
c case, the matrix A is equal to matrix a whose components are
c given in equation 8 29 in Brekhovskikh  The components for this
c matrix are calculated using the parameters from the sediment layer
c The numbering of the layers here is done as in Brekhovskikh
c The solid layers are numbered starting from the lower solid half-
c space  In the case being considered, the basement is layer 1, the
c sediment is layer 2, and the water is layer 3
C*****************************************************************

c Variable names are based mainly on those used by Brekhovskikh
C     A(ij)       4X4 Matrix in equation (8 31)  Note (== a) from
c                 equation (8 28) for the case being considered
c     ANG_FREQ    Angular frequency of incident wave
c     C(n)        Compressional wave speeds
c     B(n)        Shear wave speeds
c     Kp(n)       Compressional wavenumber for layer n
c     Ks(n)       Shear wavenumber for layer n
c     E           Horizontal component of all wave vectors
c     ALPHA(n)    Vertical components of compressional wave vectors
c     BETA(n)     Vertical components of shear wave vectors
c     U3z         Z component particle displcmt at wat-sed interface
c     T3z         Z component of stress at water - sediment interface
c     Zin         Input impedance to the solid layers
c     Z3          Characteristic impedance of the water
c     V           Reflection coefficient
c
c*****************************************************************

      SUBROUTINE REFL_COEF
     &   ( NUMANGLES, NUMFREQS, FREQMIN, FREQMAX, RSEDTHICK,
     &    CR, BR, ATTENP, ATTENS, RDENSITY, RUF,
     &    GRAZANGLE, RC )

      DOUBLE PRECISION
     &     PI,          ' Pi == 3 141592654
     &     FREQ,        ' Frequency of incident wave in Hertz
     &     FREQMIN,     ' Minimum frequency to use in average
     &     FREQMAX,     ' Maximum frequency to use in average
     &     FREQSTEP,    ' Frequency step size to use in average
     &     CR(3),       ! Real parts of layer compressional wave speeds
     &     BR(3),       ' Real parts of layer shear wave speeds
     &     ATTENP(3),   ' P wave attenuations in dB per wavelength
     &     ATTENS(3),   ' S wave attenuations in dB per wavelength
     &     RDENSITY(3),' Input densities of layers
     &     RSEDTHICK,   ' Input sediment thickness
     &     RUF(3),      ' Roughness above bsmt and sed interfaces
     &     kr,          ' Temporarily stores real part of wave numbers
     &     GRAZANGLE(90), ' Grazing Angles
     &     RC(90)       ! Reflection coefficients

      DOUBLE COMPLEX
     &     i, A(4,4), M(4,4), ANG_FREQ, C(3), B(3),
     &     Kp(3), Ks(3), ANG_IN, E,
     &     ALPHA(3), BETA(3), SEDTHICK, DENSITY(3),
     &     P, Q, X_W,
```

```
     &     SINP, COSP, SINQ, COSQ,
     &     SINTHETA1, COSTHETA1, SINGAMMA1, COSGAMMA1,
     &     SIN2THETA1, COS2THETA1, SIN2GAMMA1, COS2GAMMA1,
     &     U3z, T3z, Zin, Z3, V,
     &     E2mB2, E2pB2INV, RHOB2

      INTEGER
     &     J,          ! Iterative index
     &     L,          ' Index for layer number
     &     IGRAZANG,   ' Grazing angle index
     &     NUMFREQS,   ' Number of frequencies to average over
     &     NUMANGLES   ' Number of grazing angles

c-----------------------------------------------------------------

C  Constants

      i = ( 0 D0, 1 D0 )
      PI = 3 1415926535897932D0

C-----------------------------------------------------------------

c Initialize values in vector RC() to zero

       DO IGRAZANG = 1, NUMANGLES
         RC(IGRAZANG) = 0 D0
       END DO

C-----------------------------------------------------------------

C Assign values to the parameters in the water which do not change
C and put double precision densities in complex double variables

      L = 3
      B(L) = ( 0 0D0, 0 0D0 )     ! No shear wave speed in water
      Ks(L) = ( 0 0D0, 0 0D0 )    ! No shear wave number in water
      BETA(L) = ( 0 0D0, 0 0D0 ) ! No vert  shear wave component in water

      DO L = 1, 3                              ' Work with complex density
        DENSITY(L) = DCMPLX( RDENSITY(L) )  ! variables but densities
      END DO                                   ! here are always real
      SEDTHICK = DCMPLX( RSEDTHICK )

C-----------------------------------------------------------------

c Start frequency and grazing angle loops here

C   Determine the frequency step size
      IF ( NUMFREQS  GT  1 ) THEN
        FREQSTEP = ( FREQMAX-FREQMIN ) / DBLE( NUMFREQS - 1 )
      ELSE
        FREQSTEP = 0 1D0 ! Note FREQSTEP undefined for NUMFREQS = 1
      END IF

c   Start the Frequency loop
      DO FREQ = FREQMIN, FREQMAX, FREQSTEP

c     Convert frequency from units of Hz to rad/s and put in complex var
      ANG_FREQ = DCMPLX( 2 D0 * PI * FREQ )

c   Start the grazing angle loop
      DO IGRAZANG = 1, NUMANGLES

C     Convert grazing angle in degrees to incidence angle in radians
      ANG_IN = DCMPLX( (90 D0-GRAZANGLE(IGRAZANG) )*PI/180 D0, 0 D0 )

c-----------------------------------------------------------------

c Calculate the parameters associated with the water layer

      L = 3 ' Water layer is number 3 for sed-bsmt model
```

```
      C(L) = DCMPLX( CR(L) )  ! Compressional wave speed
      Kp(L) = ANG_FREQ / C(L) ' Wave number in water
      E = Kp(L) * SIN(ANG_IN) ' Horizontal component for all
      ALPHA(L) = SQRT( Kp(L)**2 - E**2 ) ' Vert  comp  of Kp in water

c-----------------------------------------------------------------

c Incorporate attenuations into complex sound speeds and wave components
C for the solid layers  Note entered sound speeds are just the phase speeds
c The real parts of the wave numbers are calculated from these  The
c imaginary parts of the wave numbers are calculated from the attenuations

      DO L = 1, 2  ' Calculate parameters for basement and sed  layers

c      First calculate complex wave numbers  Note sound speeds CR() and BR()
c      here are purely real  Complex sound speeds are calculated later  The
c      imaginary parts of the wave vectors are determined from the
c      entered attenuations
        kr = DBLE(ANG_FREQ) / CR(L)  ! Real part of compr  wave num
        Kp(L) = DCMPLX( kr, kr * ATTENP(L) / 54 57505415D0 )
        kr = DBLE(ANG_FREQ) / BR(L)  ' Real part of shear wave num
        Ks(L) = DCMPLX( kr, kr * ATTENS(L) / 54 57505415D0 )

c      Now calculate the vertical components of the wave vectors
        ALPHA(L) = SQRT( Kp(L)**2 - E**2 ) ' Vert  component of compr
        IF ( DIMAG( ALPHA(L) )  LT  0 D0 ) ALPHA(L) = -1  * ALPHA(L)
        BETA(L) = SQRT( Ks(L)**2 - E**2 )  ' Vert  component of shear
        IF ( DIMAG( BETA(L) )  LT  0 D0 ) BETA(L) = -1  * BETA(L)
c
c      Calculate complex sound speeds from the complex wavenumbers
        C(L) = ANG_FREQ / Kp(L)
        B(L) = ANG_FREQ / Ks(L)

      END DO

c-----------------------------------------------------------------------

c Calculate matrix A (equiv to matrix "a" for current case)
c This matrix is given in equation (8 29) in Brekhovskikh
c If more than one intermediate layer is present, then matrices
c of this form must be calculated for them and these matrices
c must be multiplied together starting with the top layer on the
c left

      L = 2 ! layer number  2 == sediment for present problem

      P = ALPHA(L) * SEDTHICK
      Q = BETA(L) * SEDTHICK
      SINP = SIN(P)
      COSP = COS(P)
      SINQ = SIN(Q)
      COSQ = COS(Q)

      E2mB2 = E**2 - BETA(L)**2
      E2pB2INV = 1  / Ks(L)**2
      RHOB2 = DENSITY(L) * B(L)**2

      A(1,1) = ( 2 * E**2 * COSP - E2mB2 * COSQ ) * E2pB2INV

      A(1,2) = -1 * i * E * ( E2mB2 / ALPHA(L) * SINP +
     &         2  * BETA(L) * SINQ ) * E2pB2INV
      A(1,3) = i * E / RHOB2 * ( COSQ - COSP ) * E2pB2INV

      A(1,4) = ( E**2 / ALPHA(L) * SINP + BETA(L) * SINQ ) *
     &         E2pB2INV / RHOB2
      A(2,1) = i * E *( E2mB2 / BETA(L) * SINQ +
     &         2  * ALPHA(L) * SINP ) * E2pB2INV
      A(2,2) = ( 2  * E**2 * COSQ - E2mB2 * COSP ) * E2pB2INV

      A(2,3) = ( ALPHA(L) * SINP + E**2 / BETA(L) * SINQ ) *
```

```
     &          E2pB2INV / RHOB2
      A(2,4) = A(1,3)

      A(3,1) = 2 * i * RHOB2 * E * E2mB2 * ( COSQ - COSP ) * E2pB2INV

      A(3,2) = -1 * RHOB2 * ( E2mB2**2 / ALPHA(L) * SINP +
     &          4 * BETA(L) * E**2 * SINQ ) * E2pB2INV
      A(3,3) = A(2,2)

      A(3,4) = A(1,2)

      A(4,1) = -1  * RHOB2 * ( E2mB2**2 / BETA(L) * SINQ +
     &          4 * ALPHA(L) * E**2 * SINP ) * E2pB2INV
      A(4,2) = A(3,1)

      A(4,3) = A(2,1)

      A(4,4) = A(1,1)

C-----------------------------------------------------------------

c Calculate components of matrix M shown in Brekhovskikh (8 38)
c Only require M22, M23, M24, M32, M33, and M34

        DO K = 2, 4
          M(2,K) = A(2,K) - A(2,1) * A(4,K) / A(4,1)
          M(3,K) = A(3,K) - A(3,1) * A(4,K) / A(4,1)
        END DO

C-----------------------------------------------------------------

C Calculate the ratio X/W in variable X_W as in Brekhovskikh (8 44)
c This is the ratio of the transimitted shear wave displacement
c potential amplitude to the transmitted compressional amplitude
c Note that the last term in the denominator  sin(2theta1) should
c be cos(2theta1)  Also the b^2/c^2 multiplying that term should be
c deleted from Brekhovskikh's expression

c     First need the following expressions
      SINTHETA1 = E / Kp(1)
      COSTHETA1 = ALPHA(1) / Kp(1)
      SINGAMMA1 = E / Ks(1)
      COSGAMMA1 = BETA(1) / Ks(1)
      SIN2THETA1 = 2 * SINTHETA1 * COSTHETA1
      SIN2GAMMA1 = 2 * SINGAMMA1 * COSGAMMA1
      COS2GAMMA1 = COSGAMMA1**2 - SINGAMMA1**2

      X_W = -1  * ( E * A(4,1) - ALPHA(1) * A(4,2) + i *
     &      ANG_FREQ**2 * DENSITY(1) * ( COS2GAMMA1 * A(4,3) -
     &      SIN2THETA1 * A(4,4) * B(1)**2 / C(1)**2 ) ) /
     &      ( Ks(1) * COSGAMMA1 * A(4,1) + E * A(4,2) -
     &      i * ANG_FREQ**2 * DENSITY(1) * ( SIN2GAMMA1 *
     &      A(4,3) + COS2GAMMA1 * A(4,4) ) )

c-----------------------------------------------------------------

c Calculate z components of particle displacement U3z, and stress at
c the water - sediment interface T3z  Note Brekhovskikh equ  (8 43)
c should have a multiply instead of a divide in the expression for
c Zin   Also, the last "+" sign in the expression for A should be a
c "-" sign   The expressions for U3z and T3z below are actually the
c A and B from equations 8 43  These however are related to the true
c displacement and stress by A = i*T3z/W and B = i*U3z/W  Since only
c the ratio of T/U is required we can use A/B because T/U = A/B

      T3z = ALPHA(1) * M(3,2) - i * ANG_FREQ**2 * DENSITY(1) *
     &      ( COS2GAMMA1 * M(3,3) - SIN2THETA1 *
     &      M(3,4) * B(1)**2 / C(1)**2 ) -
     &      ( E * M(3,2) - i * ANG_FREQ**2 * DENSITY(1) *
     &      ( SIN2GAMMA1 * M(3,3) + COS2GAMMA1 * M(3,4) ) ) * X_W
```

```
      U3z = ALPHA(1) * M(2,2) - ı * ANG_FREQ**2 * DENSITY(1) *
     &       ( COS2GAMMA1 * M(2,3) - SIN2THETA1 *
     &      M(2,4) * B(1)**2 / C(1)**2 ) -
     &       ( E * M(2,2) - ı * ANG_FREQ**2 * DENSITY(1) *
     &       ( SIN2GAMMA1 * M(2,3) + COS2GAMMA1 * M(2,4) ) ) * X_W

C-----------------------------------------------------------------

C Calculate the "Characterıstıc ımpedance" ın the water Z3, and
C the ınput ımpedance Zın, to the solıd layer system   Expressıons
c for these quantıtıes are gıven ın Brekhovskıkh (8 42)

      Z3 =  DENSITY(3) * C(3) / COS( ANG_IN )
      Zın = ı * T3z / ( ANG_FREQ * U3z )

c-----------------------------------------------------------------

C Calculate the reflectıon coeffıcıent from the characterıstıc
C ımpedance of the water and the ınput ımpedance of the solıd layers
C usıng Brekhovskıkh (8 41)

      V = ( Zın - Z3 ) / (Zın + Z3 )

C-----------------------------------------------------------------

C Add contrıbutıon from present frequency and grazıng angle
C ınto vector RC()

      RC(IGRAZANG) = RC(IGRAZANG) + ABS( V )**2 / DBLE( NUMFREQS )

C-----------------------------------------------------------------

C Termınate loops ın angle and frequency

      END DO ' For do loop ın angle
      END DO ' For do loop ın frequency

C-----------------------------------------------------------------

C Convert power reflectıon coeffıcent to the equıvalent amplıtude
C reflectıon coeffıcıent  Note thıs ıs not the ordınary coeffıent
C unless the bandwıdth ıs zero  It does, however represent
C reflectıon loss ın a band over whıch the ınput sıgnal power
C spectrum ıs constant

      DO IGRAZANG = 1, NUMANGLES
        RC(IGRAZANG) = SQRT( RC(IGRAZANG) )
      END DO

C-----------------------------------------------------------------
C Return to callıng program

      RETURN
      END
*****************************************************************
```

Vita

Surname Hannay — Given Names David Edward

Place of Birth — Victoria, British Columbia, Canada

Educational Institutions Attended

University of Victoria	1991 to 1995
University of Victoria	1983 to 1988

Degrees Awarded

B Sc	University of Victoria	1988

Publications

N R Chapman and D E Hannay, "Seismic velocities of upper oceanic crust," Geophysical Research Letters (American Geophysical Union) ," Vol 21, No 21, p 2315 - 2318, Oct 1994

P Gerstoft, D E Hannay, and D Gingras, Matched Field Inversion of Multifrequency Data," Journal of the Acoustical Society of America ," Vol 96, 3234(A), 1994

N G Henson, D E Hannay, P Scrimger, and S E Dosso, "Efficient Acoustic Field Computation for Estimating Geoacoustic Bottom Parameters using Matched Field Inversion," in Full Field Inversion Methods in Ocean and Seismic Acoustics, Ed P Gerstoft and O Diachok, NATO conference series, (Publication Pending, 1994)

D E Hannay "Bottom Loss Processing of the Pacific Echo IV Experiment Data", D R E P Contractor report number 94-52, May 1994

D E Hannay and N R Chapman, Inversion of geoacoustic profiles in thin-sediment environments from ocean bottom reflection loss data, in IEEE Oceans 93, Vol III, p 381-386, 1993

D E Hannay "Correction of Bottom Loss Measurements from Pacific Echo Data using Coherent Summation of Multipath Energy," D R E P Contractor report number 93-51, August 1993

D E Hannay, "Bottom Loss Processing of the Pacific Echo III Experiment Data", D R E P Contractor report number 93-32, May 1993

D E Hannay, "Bottom Loss Processing of the Pacific Echo II Experiment Data", D R E P Contractor report number 92-31, September 1992

D E Hannay, "Estimation of the Geoacoustic Properties of the Upper Oceanic Crust from Bottom Reflection Loss Measurements," Journal of the Acoustical Society of America ," Vol 92, 2303(A), October 1992

D E Hannay, "Depth Scaling of Source Levels from 0 82 kg SUS Charges", Canadian Acoustical Association Symposium, October 1992

D E Hannay, "Propagation Losses from Shallow Sources" D R E P Contractor report number 91-17, March 1991

D E Hannay, "Manual for program PLOT, and bottom loss database", D R E P Contractor report number 90-10, June 1990

D E Hannay, "Methodology for Processing Acoustic Time Series Data to Determine Propagation and Bottom Losses", D R E P Contractor report for W7708-9-1055, April 1990

PARTIAL COPYRIGHT LICENSE

I hereby grant the right to lend my thesis to users of the University of Victoria Library, and to make single copies only for such users or in response to a request from the Library of any other university, or similar institution, on its behalf or for one of its users I further agree that permission for extensive copying of this thesis for scholarly purposes may be granted by me or a member of the University designated by me It is understood that copying or publication of this thesis for financial gain shall not be allowed without my written permission

Title of Thesis

Estimation of Geoacoustic parameters of the
Ocean Bottom by Inversion of Reflection Loss data

Author [redacted]

David Edward Hannay
April 3, 1995